2024 - 2025

DIPLÔME UNIVERSITAIRE DE GEMMOLOGIE

Nantes University

U.F.R Sciences et Techniques

OVERVIEW OF THE TUGTUPITE

IDENTIFICATION, CHARACTERIZATION, PHOTOCHROMIC PROPERTIES, AND ASSOCIATED MINERALS

par

CHAPUIS Claire

Publicly defended

4th November 2025

At the Department of Earth and Universe Sciences

Before the following jury

PRESIDENT	CHAUVIRÉ B.	*Associate professor, Nantes University*
VICE-PRESIDENT	KARAMPELAS S.	*Assistant professor,* *University of Thessalonique and scientific consultant of LFG*
EXAMINERS	DELAUNAY A.	*Head of Laboratoire Français de Gemmologie*
	GAILLOU E.	*Head and curator of Musée de Minéralogie des Mines de Paris*
	LATOUCHE C.	*Professor, Nantes Université*
	NOTARI F.	*Founder of GGTL Laboratories Switzerland and Head of Scientific Research at AIGS (Bangkok)*
INVITED	FRITSCH E.	*Professor Emeritus, Nantes University*
	LASNIER B.	*Founder of DUG*

“Somewhere, something incredible is waiting to be known.”
Carl Sagan

Acknowledgements

First, I would like to sincerely thank the entire pedagogical team of the University Diploma in Gemology at Nantes University: Dr. Boris Chauviré, Pr. Emmanuel Fritsch and Dr. Stefanos Karampelas, as well as the external gemologists: Dr. Eloïse Gaillou and Mr. Vincent Pardieu, who generously shared their time, expertise, valuable knowledge, and in the use of laboratory instruments during the practical sessions. I would also like to thank all the kind people I had the pleasure to meet through this program, and express my gratitude to the members of the jury for the time they have dedicated to reading and evaluating my research memoir.

Many thanks to the Jean Rouxel Institute of Materials Nantes (IMN), to Mr. Aurélien Delaunay, Director of the French Gemological Laboratory (LFG) in Paris, and to all the team of the GGTL Laboratories Switzerland, who provided me with access to their laboratory equipment. I am also grateful to all those who lent or donated to me tugtupite samples for this study: Pr. E. Fritsch (IMN, Nantes University, France), Dr. I. Lykova (Canadian Museum of Nature, Canada), Mr. M. T. M. Haris (Enteem Gem Laboratory, Sri Lanka), Mr. S. Milliner, and Mr. R. Muller (Hypo-Créa & Minéraux, France). Their generosity made this project possible.

Special thanks go to my first gemology professors at the National Institute of Gemology in Lyon, Anne Laurent and Loïc Lescuyer, to whom I will always be grateful for transmitting their passion to me from day one, a passion that continues to grow every day.

Likewise, I extend my thanks to all the gemologists from the Lyon and Nice groups, for their kindness, their willingness to share their knowledge and always show us incredible gemstones during annual gemology tournaments.

I warmly thank all those who have offered a helping hand throughout my professional career, from the first person who gave me an internship to those who continue to contribute to my growth and my professional fulfillment.

And last but certainly not least, a special thanks to my closest friends, as well as to my parents, for their undeniable support through this challenging year.

All these people have played an essential role in helping me to complete this work. I am deeply grateful for their contribution and their invaluable support throughout this journey.

List of Cited Minerals

Minerals Name	***IMA-CNMNC Approved Mineral Symbols***	***Chemical Formula***
Aegirine	Aeg	$NaFe^{3+}Si_2O_6$
Albite	Ab	$Na(AlSi_3O_8)$
Analcime	Anl	$Na(AlSi_2O_6) \cdot H_2O$
Anorthite	An	$Ca(Al_2Si_2O_8)$
Arfvedsonite	Arf	$NaNa_2(Fe^{2+}_4Fe^{3+})Si_8O_{22}(OH)_2$
Barylite	By	$BaBe_2Si_2O_7$
Chesnokovite	Ck	$Na_2SiO_2(OH)_2 \cdot 8H_2O$
Chkalovite	Ckl	$Na_2BeSi_2O_6$
Eudialyte	Eud	$Na_{15}Ca_6Fe_3Zr_3Si(Si_{25}O_{73})(O,OH,H_2O)_3(Cl,OH)_2$
Manganoneptunite	Mnnpt	$KNa_2LiMn^{2+}_2Ti_2Si_8O_{24}$
Microcline	Mcc	$K(AlSi_3O_8)$
Natrolite	Ntr	$Na_2(Si_3Al_2)O_{10} \cdot 2H_2O$
Nepheline	Nph	$Na_3K(Al_4Si_4O_{16})$
Neptunite	Npt	$KNa_2LiFe^{2+}_2Ti_2Si_8O_{24}$
Pyrochlore Group	**Pcl**	**$A_2Nb_2(O,OH)_6Z$** **A** = Na, Ca, Sn^{2+}, Sr, Pb^{2+}, Sb^{3+}, Y, U^{4+}, H_2O or □ (vacancy) **Z** = OH, F, O, H_2O or □ (vacancy) (mindat.org/min-3316.html, 2025)
Sodalite	Sdl	$Na_4(Si_3Al_3)O_{12}Cl$
Sørensenite	Sør	$Na_4Be_2Sn(Si_3O_9)_2 \cdot 2H_2O$
Sphalerite	Sp	ZnS
Tugtupite	Ttp	$Na_4BeAlSi_4O_{12}Cl$
Ussingite	Usg	$Na_2AlSi_3O_8(OH)$

All the chemical compositions, except for that of pyrochlore, have been found in the "List of Minerals" through the RRUFF link (https://rruff.info/ima/?Tugtupite) provided by the International Mineralogical Association (IMA, 2025).

Acronyms and Abbreviations

Acronyms	***Meaning***
EDX-SEM	Energy-Dispersive X-ray Scanning Electron Microscope
ED-XRF	Energy-Dispersive X-ray Fluorescence
EDS	Energy-Dispersive Spectroscopy
BSE	Backscattered Electron
FTIR	Fourier-Transform InfraRed
SEM	Scanning Electron Microscope
UV-Vis-NIR	Ultraviolet-Visible-Near Infrared
LWUV	Long-Wave Ultraviolet
SWUV	Short-Wave Ultraviolet

Table of Contents

Acknowledgements *3*

List of Cited Minerals *4*

Acronyms and Abbreviations *4*

Introduction *6*

CHAPTER I: State of the art on tugtupite and its commonly associated minerals *7*

- **History of the discovery** **7**
- **Geology** **7**
  - Ilímaussaq intrusion, Greenland 9
  - Lovozero intrusion, Russia 11
  - Mont Saint-Hilaire complex, Canada 12
- **Chemical and mineralogical properties** **13**
  - Chemical formula and mineralogical group 13
  - Crystallographic structure and crystal shapes 13
  - Mineralogical characteristics 15
- **Optical characteristics** **15**
  - Luminescence 16
  - Phosphorescence 18
  - Inclusions 19
  - Color, origin of the color 19
- **Photochromic behavior** **19**
  - Definition of photochromism 19
  - Photochromism applied to tugtupite 19

CHAPTER II: Materials and Methods *23*

- **Materials** **23**
- **Methods** **25**
  - Classical Gemology instruments 25
  - Laboratory equipment 25

CHAPTER III: Results *29*

- **Tugtupite** **29**
  - Classical Gemology 29
  - Laboratory Gemology 37
- **Associated Minerals** **54**
  - Laboratory Gemology 54

CHAPTER IV: Discussion *68*

- **Classical Gemology** **68**
- **Laboratory Gemology** **68**
  - Tugtupite Identification and Characterization 68
  - Associated minerals identification 71

CONCLUSION AND OUTLOOK ON FUTURES ANALYSES *73*

REFERENCES *74*

ANNEXES *80*

- **ANNEX I: ADDITIONAL FT-RAMAN SPECTRA** **81**
- **ANNEX II: EDXRF ANALYSES RESULTS** **84**
- **ANNEX III: SEM ASSOCIATED MINERALS ANALYSES RESULTS** **86**
- **ANNEX IV: SUPPLEMENTARY SEM PHOTOMICROGRAPHS** **96**

Introduction

The present experimental study has been realized as part of the University Diploma in Gemology (DUG), delivered by Nantes University, France, under the supervision of Professors Emmanuel Fritsch, Boris Chauviré and Stefanos Karampelas. The research focuses on the mineral tugtupite from the three localities known to date: Greenland (type locality) Russia and Canada. The aim is to present its identification criteria as a gemstone, its characteristics in relation to associated minerals, and to determine similarities and differences between samples from these different geographic origins.

Tugtupite has several aspects of interests in gemology, such as luminescence and photochromism, the latter being the main reason I chose this subject. I have always had a strong interest in gemology, chemistry, and physics. Throughout my academic career, I was interested in looking to find a special property that connected them. Thanks to my gemology professor Loïc Lescuyer, I discovered the amazing property of a few gemstones to change colors in a reversible way, through exposition to an electromagnetic radiation: a phenomenon called photochromism. Since then, I have been pursuing a deeper understanding of this phenomenon by studying and reading various articles about photochromic gemstones. My first study on the topic was on hackmanite, the photochromic variety of sodalite, during my studies at the National Institute of Gemology (ING) in Lyon, France. For the literature report required in this diploma, I chose to focus on the photochromic and the thermochromic behaviors in chameleon diamonds. Therefore, studying tugtupite represents a logical continuation toward the understanding of this phenomenon.

Moreover, the fact that photochromism is still not fully understood and remains a subject open to discovery motivated me to explore it. I was especially motivated by the opportunity to study a gemstone that has received relatively little attention in gemology so far.

Thanks to the advanced laboratory equipment at the Jean Rouxel Institute of Materials (IMN) in Nantes, at the French Gemological Laboratory (LFG) in Paris, at the GGTL Laboratories Switzerland, to the knowledge provided by the University Diploma in Gemology in Nantes and to all the persons and institutions who provided me tugtupite, I was able to study this stone in greater depth and add a small contribution to the knowledge surrounding this fascinating mineral.

This study represents an important step in my journey as a gemologist. This work continues to feed my passion for gemology, especially for photochromism, which has fascinated me for several years.

CHAPTER I: State of the art on tugtupite and its commonly associated minerals

History of the discovery

Tugtupite was first discovered in 1957 along the coastal cliffs of Tugtup agtakôrfia, located on the north coast of the Tunugdliarfik Fjord in South Greenland, by danish geologist and professor, Henning Sørensen (*figure 1*). It was initially described as "beryllium sodalite" (*Sørensen, 1960*). Around the same time, Russian petrologist E. I. Semenov identified a mineral from the Lovozero intrusion of the Kola Peninsula in Russia, related to sodalite but exhibiting non-cubic crystal symmetry. It was named “beryllosodalite” (*Semenov & Bykova, 1960; Povarennykh et al., 1971*).

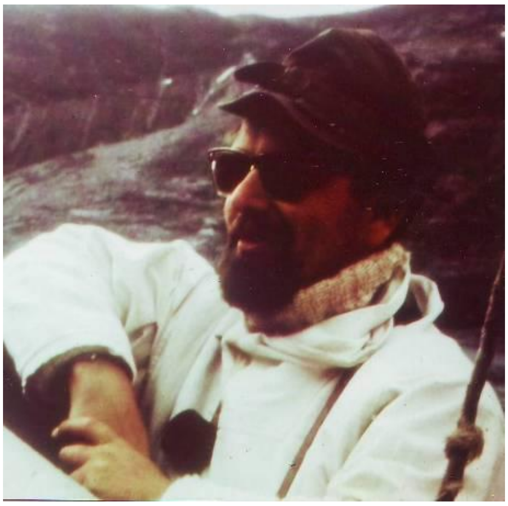

Figure 1: Henning Sørensen (1926-2013), mineralogist and petrographer, professor of geology, University of Copenhagen (Denmark). Photo from Roy Kristiansen by courtesy of Henning Sørensen. Photo scanned from paper color print (*mindat.org/photo-353565.html, 2025*).

Further investigations revealed that both minerals were identical, differing mainly in occurrence and grain size. While the Russian specimens were rarer and found in smaller grains (up to 3 mm), those from Greenland were more abundant and larger in size (*Sørensen et al., 1971)*.

Sørensen (1962) published additional data, demonstrating that “beryllium sodalite” and “beryllosodalite” were in fact a singular new mineral with distinct chemical and physical properties of sodalite. He proposed the name “tugtupite,” in reference to the discovery locality, and this was officially accepted by the Commission on New Minerals and Mineral Names of the International Mineralogical Association (IMA) in 1965 (*Sørensen et al., 1971*).

Geology

Tugtupite is a beryllium silicate mineral that forms during the final hydrothermal stage of peralkaline magmatic intrusions (*Sørensen et al., 1971; Milisenda et al., 2015*). This stage occurs after the main magma has crystallized. It is known from several localities, including the Ilímaussaq complex in Greenland, the Lovozero intrusion in Russia, and the Mont Saint-Hilaire in Canada (*figure 2*).

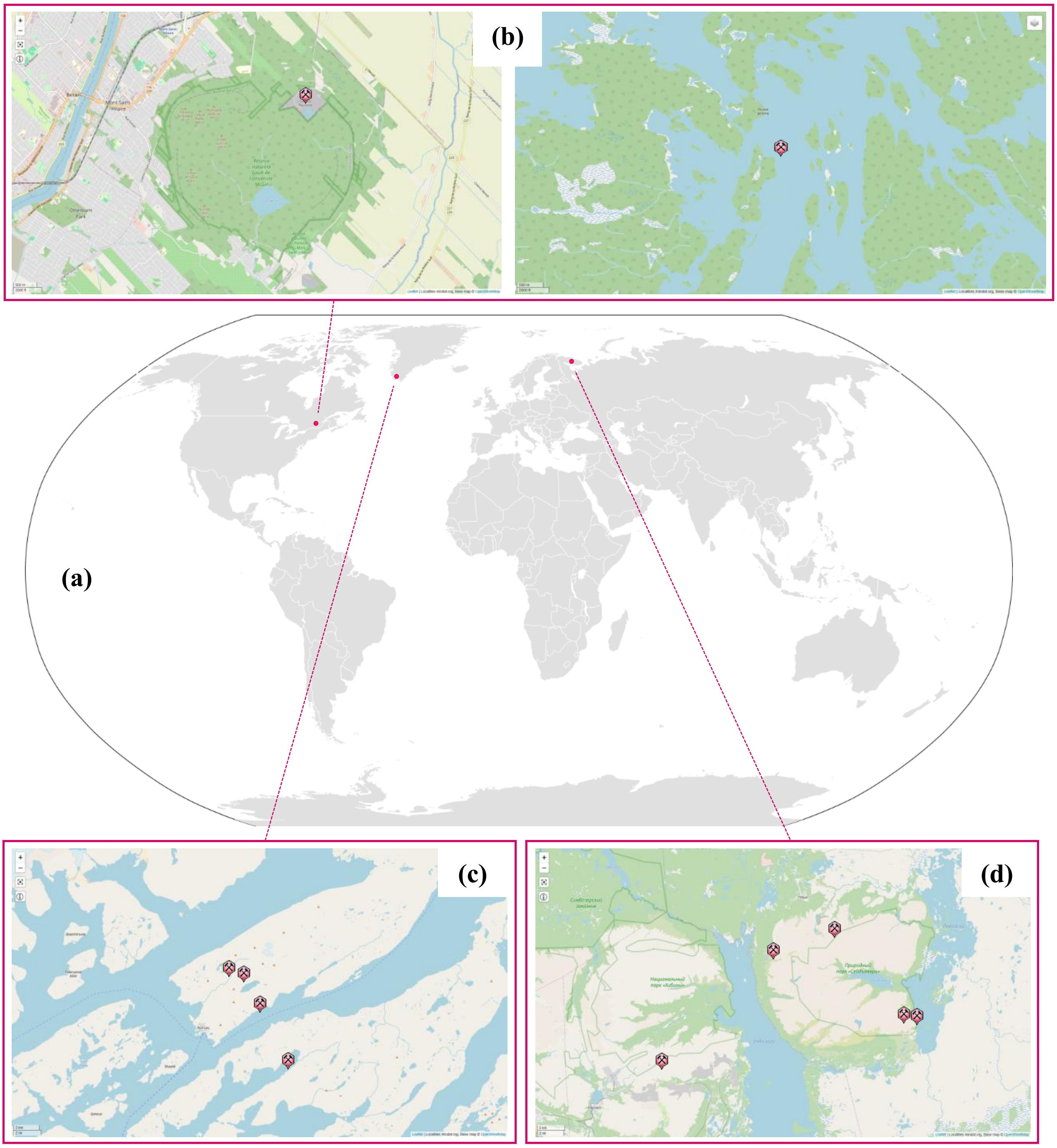

Figure 2: Geographic distribution of known tugtupite localities with close-up views of each mining area (represented by the mines and prospects red icon). (a) General map showing the three known occurrences: Canada, Greenland, and Russia. (b) Close-up on Canada: on the left, the Poudrette Quarry, Mont Saint-Hilaire, La Vallée-du-Richelieu RCM, Montérégie, Québec; and on the right, the Cabonga Reservoir area, Réservoir-Dozois, La Vallée-de-l'Or RCM, Abitibi-Témiscamingue, Québec. (c) Close-up on the Ilímaussaq complex, Kujalleq, Greenland. From top to bottom: Kuannersuit Plateau (Kvanefjeld), Taseq Slope, Tugtup agtakôrfia, and Qeqertaussaq Island (Kangerluarsuk fjord). (d) Close-up on the Lovozero intrusion, Lovozersky District, Murmansk Oblast, Russia. From left to right: Eveslogchorr Mt, Khibiny Massif, Shkatulka pegmatite, Umbozero mine, Alluaiv Mt, Karnasurt Mt, Punkaruaiv Mt, and Malyi Punkaruaiv Mt pegmatite. Map created by Claire Chapuis, based on information from *mindat.org/min-4044.html* (*Mindat, 2025, consulted 10/10/2025*).

Ilímaussaq intrusion, Greenland

In Greenland, tugtupite occurs within the 1.15-Ga-old Gardar failed rift province of South Greenland, the Ilímaussaq intrusive complex (*figure 3*), a layered intrusion composed mainly of naujaite, lujavrite, and sodalite syenite (*Markl & Baumgartner, 2002*). Naujaite is an igneous, peralkaline rock with high Na_2O and K_2O and low CaO and MgO contents and typically occurs in alkaline igneous complexes and rare-element pegmatites (*Mindat, 2025*). Lujavrite is a dark, coarse-grained variety of nepheline syenite rich in eudialyte, arfvedsonite, and aegirine, containing alkali feldspars or microcline and albite. It is characterized by a high concentration of incompatible elements such as rare-earth elements (REE), U, Th, Li etc. (*Mindat, 2025*).

Tugtupite forms in hydrothermal veins rich in albite and analcime, cutting through naujaite, and develops via replacement of chkalovite, a primary Be-silicate. These veins were formed after the consolidation of the main intrusion, from fluids released by the cooling lujavrite magma, a residual, volatile-rich phase enriched in rare elements and beryllium. Associated minerals include Li-mica, sodalite, microcline, aegirine, steenstrupine, and epistolite (*Sørensen et al., 1971*).

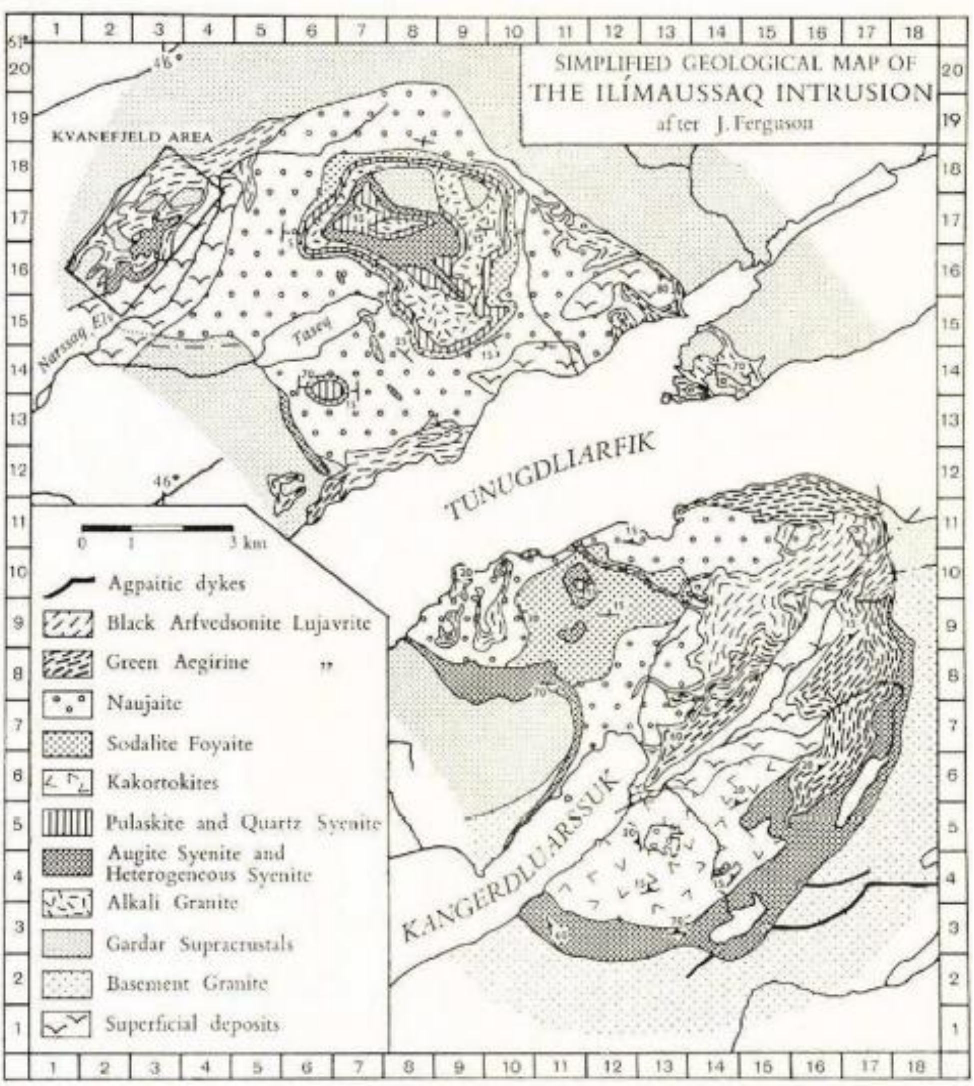

Figure 3: Geological map of the Ilímaussaq intrusion (*after Ferguson, 1964*). The coordinates of the main localities are: Tugtup agtakôrfia (8,12); Head of Kangerdluarssuk (12,7); Kvanefjeld (3,16); and the Taseq region (5,15).

The mineral typically appears as pink to red aggregates or veinlets, with local variations:

At Tugtup agtakôrfia, tugtupite occurs in almost vertical albitite-analcime veins cutting naujaite enclosed by black lujavrite (*figure 4*). It forms fine-grained pink to red aggregates and thin veinlets in analcime-albite rocks, often enclosing chkalovite (*figure 5*). Associated minerals include Li-mica, sodalite, microcline, aegirine, steenstrupine, schizolite, and epistolite (*Sørensen et al., 1971*).

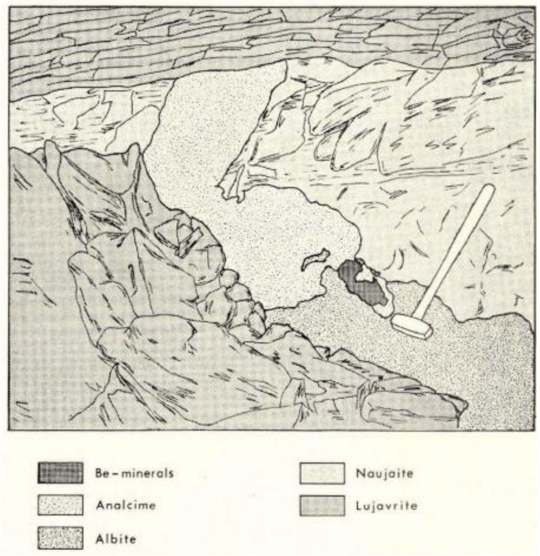

Figure 4: Explicative schema of tugtupite-bearing part of albitite vein at Tugtup agtakôrfia. Hammer handle about 40 cm long (*after Sørensen et al., 1971*).

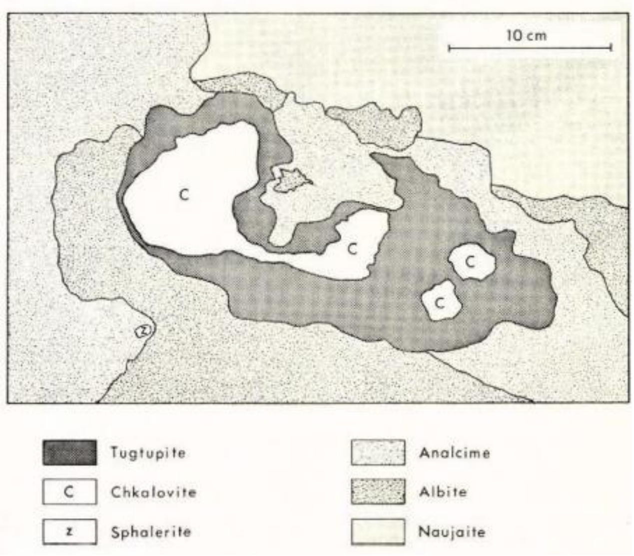

Figure 5: Close-up schema of the tugtupite-chkalovite intergrowth at Tugtup agtakôrfia (*after Sørensen et al., 1971*).

At the head of Kangerdluarssuk, tugtupite occurs in a fine-grained aegirine-albite vein with small amounts of analcime, sodalite, and natrolite. As at Tugtup agtakôrfia, chkalovite grains are rimmed and replaced by tugtupite, which contains inclusions of Li-mica, eucolite, sphalerite, and britholite (*Sørensen et al., 1971*).

In the Kvanefjeld area, tugtupite is found in analcime- and albite-rich veins cutting naujaite and augite syenite. It forms bright carmine-red patches, often in the central parts of zoned veins, together with chkalovite and aegirine (*figure 6*). The veins also contain pyrochlore, neptunite, and Li-mica. Tugtupite from these veins has an intense carmine red color and is the most strongly colored variety found in the Ilímaussaq (*Sørensen et al., 1971*).

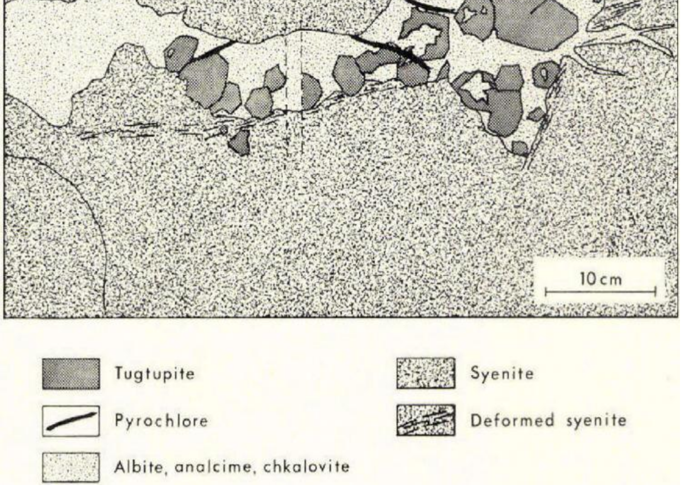

Figure 6: Typical structure of a tugtupite-bearing vein and associated minerals at Kvanefjeld (*after Sørensen et al., 1971*).

On the Taseq Plateau, tugtupite appears in several vein types: in ussingite-albite pegmatites, ussingite-rich veins, and analcime or albite veins. It forms narrow rims between chkalovite and ussingite, or fills cracks in these minerals. The associated phases include neptunite, schizolite, arfvedsonite, microcline, and Li-mica (*Sørensen et al., 1971*).

At Qeqertaussaq Island, tugtupite occurs in thin veins of aegirine and lujavrite, partially replaced by albite and analcime. Grains of chkalovite are surrounded by tugtupite, and associated minerals include arfvedsonite, astrophyllite, sphalerite, schizolite, and epistolite.

Across all Greenland sites, tugtupite forms in fractures filled by late hydrothermal fluids. These fluids are alkaline, rich in beryllium and chlorine. They first precipitate albite, analcime, and other zeolitic minerals, and then tugtupite crystallizes. Its position in the paragenetic sequence, after chkalovite and with analcime, indicates formation at low temperatures (approximately 400 °C) and under high volatile pressures (*Sørensen et al., 1971*).

Lovozero intrusion, Russia

In Russia, at the Lovozero intrusion (*figure 7, (a)*), tugtupite occurs in Be-bearing pegmatites and sodalite syenites. These pegmatites consist mainly of albite, microcline, analcime, natrolite, and ussingite, with chkalovite occurring near the margins of ussingite-rich bodies (*Semenov & Bykova, 1960*). Tugtupite is rare in Lovozero and forms small masses up to 3 mm across, typically secondary after chkalovite. It developed during intense hydrothermal reworking, when fluids replaced chkalovite within ussingite by tugtupite, while ussingite itself was altered to analcime, natrolite, and chabazite. Associated minerals include murmanite, aegirine, sphalerite, schizolite, neptunite, steenstrupine, and epistolite, showing a paragenetic sequence very similar to that in Ilímaussaq (*Yakovlevskaja & Semenov, 1963; Sørensen et al., 1971*).

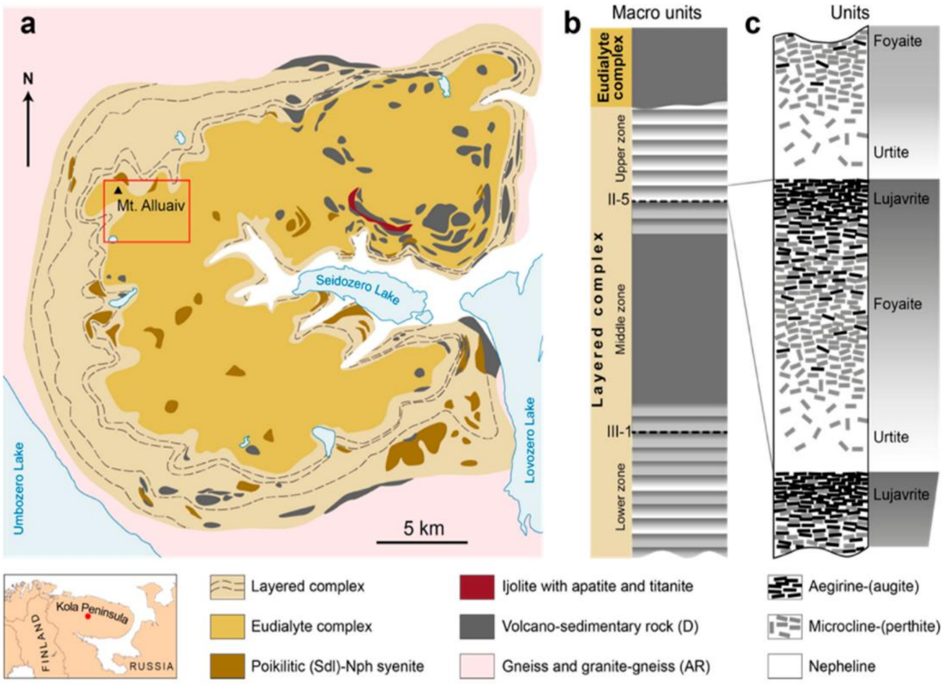

Figure 7: (a) Simplified geological map; (b) stratigraphic column; (c) schematic layering of the Lovozero Alkaline Massif, Russia. Tugtupite occurs in the Shkatulka pegmatite, located in the Umbozero mine, Alluaiv Mountain, Lovozersky District (Murmansk Oblast). This ultra-agpaitic pegmatite body is situated in the western part of Alluaiv Mountain. Shkatulkalite was identified in the marginal zone of the ussingite core of the pegmatite and in the adjacent aegirine zone (*After Mikhailova et al., 2019*).

Mont Saint-Hilaire complex, Canada

At Mont Saint-Hilaire, Canada, emplaced about 125 million years ago, the complex is mainly composed of gabbros, diorites, and various foid syenites (alkali-rich silica-undersaturated varieties of syenites essentially consisting of alkali feldspar, feldspathoids, mafic minerals like hornblende, pyroxene, sodic pyroxene/amphibole), like observed in *figure 8* (*Schilling et al., 2011*).

The formation of tugtupite is less documented but is believed to have occurred during the final hydrothermal stage of the peralkaline complex.

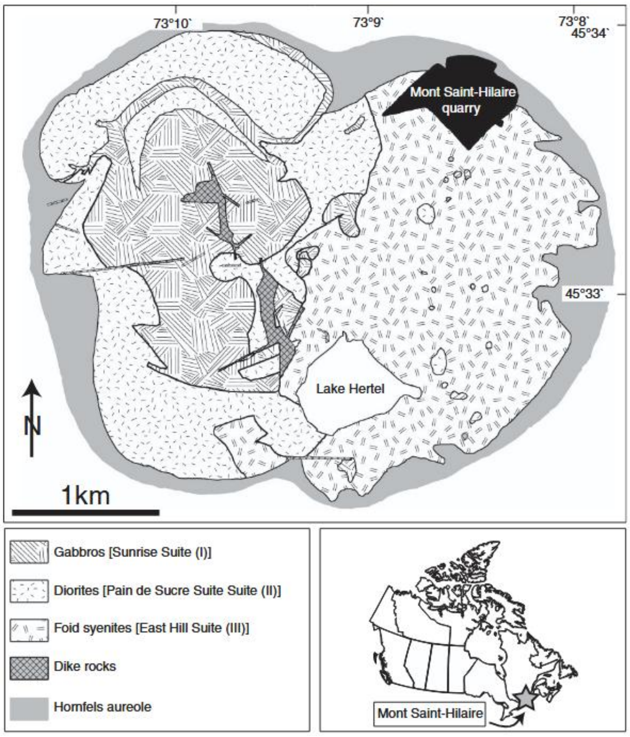

Figure 8: Simplified geological map of the Mont Saint-Hilaire complex (*after Currie, 1989; Schilling et al., 2011*).

The most evolved rocks, known as agpaitic syenites, are rich in high field strength elements (HFSE) such as Zr, Hf, Nb, Ta, Y, and REE, which are incorporated into complex silicates like the eudialyte group (*Schilling et al., 2011*).

During the transition from magmatic to hydrothermal conditions, the residual magma released hot, volatile-rich fluids containing sodium, chlorine, fluorine, and large-ion lithophile elements (LILE) such as Na, K, Rb, Cs, Li, Sr, Ba. These fluids migrated through fractures and cavities in the syenitic rocks, forming veins filled with albite, analcime, natrolite, and other zeolites (*Schilling et al., 2011*). Interaction with external CO_2-rich waters from surrounding limestones created a highly reactive and alkaline environment, favoring the formation of rare minerals such as tugtupite.

As temperatures dropped below 500 °C and silica activity decreased, Be- and Cl-bearing minerals crystallized from these alkaline fluids. Late-stage assemblages commonly include sodalite, albite, and analcime, often associated with eudialyte-group minerals. Primary feldspars were commonly albitized, and sodalite was sometimes replaced by natrolite or analcime. These replacement and veining processes are typical of late hydrothermal activity in peralkaline complexes and are similar to those observed at the Ilímaussaq complex (*Schilling et al., 2011*). The abundance of Na- and Cl-rich phases confirms that the fluids were highly alkaline and volatile-rich, providing the necessary conditions for tugtupite formation.

Therefore, tugtupite forms late in the magmatic-hydrothermal evolution of peralkaline intrusions through the replacement of chkalovite by Be- and Cl-rich fluids in albite- and analcime-bearing veins. Similar mineral assemblages and textures observed in Greenland, Russia, and Canada confirm a comparable genesis, involving volatile-rich alkaline fluids at temperatures around 400 °C, representing one of the last Be-silicates to crystallize in these complex systems. This relatively low formation temperature is important, as the photochromism is destroyed above 450 °C. Consequently, the late-stage, low-temperature hydrothermal conditions under which tugtupite crystallizes are essential for keeping its photochromic properties.

Chemical and mineralogical properties

Chemical formula and mineralogical group

Tugtupite belongs to the tectosilicate sub-class, within the feldspathoid group, specifically the cancrinite-sodalite structural group and part of the helvine subgroup (*Finch et al., 2016; Blumentritt & Fritsch, 2021; IMA, 2025*).

The first proposed formula described tugtupite as a beryllium-aluminum tectosilicate containing sodium, chlorine, with sulfur: $Na_8Al_2Be_2Si_8O_{24}(Cl,S)_2$ (*Sørensen et al., 1971*). Later, the International Mineralogical Association decided to remove the sulfur from the formula since it is not considered as a primary constituent, resulting from the accepted chemical formula: $Na_4BeAlSi_4O_{12}Cl$ (*IMA, 2025*).

Tugtupite commonly contains trace impurities. Chemical analyses have revealed the presence of H_2O (*Povarennykh et al., 1971*) and minor amounts of Fe, Ga, Mg, Ca, K, and S (*Mindat, 2025*). According to *Danø* (1966), K and Mg are substituted for Na, while S represents for approximately 5% of the Cl content.

Crystallographic structure and crystal shapes

The crystal structure of tugtupite is tetragonal (*Danø, 1966*) and closely related to that of sodalite. It consists of a three-dimensional framework of slightly distorted SiO_4, AlO_4, and BeO_4 tetrahedra, connected at their corners through shared oxygen atoms. These tetrahedra form eight-membered rings that define cages within the lattice. Each cage contains a central chlorine (Cl) atom, tetrahedrally surrounded by four sodium (Na) atoms (*Sørensen et al., 1971*). Compared to sodalite ($Na_8Al_6Si_6O_{24}Cl_2$), tugtupite ($Na_4BeAlSi_4O_{12}Cl$) exhibits lower symmetry due to the ordered distribution of Be, Al, and Si within the tetrahedral framework (*figure 9*). Structurally, the substitution of a Be-Si pair for an Al-Al pair maintains charge balance ($2Al^{3+} \rightarrow Si^{4+} + Be^{2+}$) but slightly distorts the tetrahedra (*figure 10*), lowering the cubic symmetry of sodalite to a tetragonal one (*Sørensen et al., 1971 ; Henderson & Taylor, 1977*). In particular, a Na atom forms an additional bond with the bridging oxygen between Si and Be tetrahedra (*Povarennyk et al., 1971; Finch et al., 2016*).

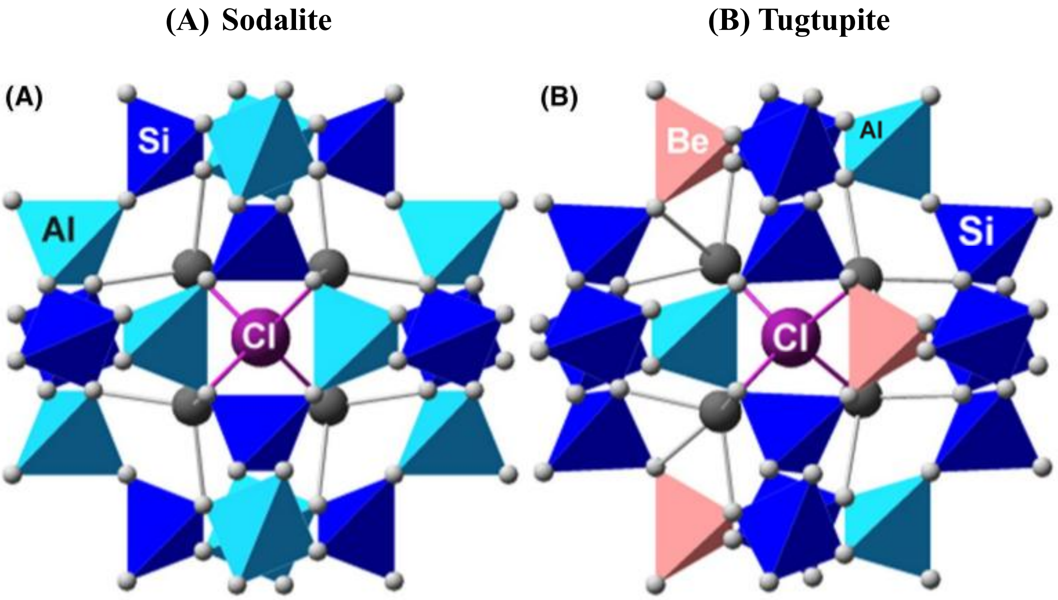

(A) Sodalite

(B) Tugtupite

Figure 9: Structural representation of sodalite (A) and tugtupite (B). In sodalite, the cages are composed of SiO_4 (dark blue) and AlO_4 (light blue) tetrahedra, whereas in tugtupite, BeO_4 tetrahedra (pink) are additionally present in the structure. The larger gray spheres represent sodium (Na) atoms, while the smaller lighter gray spheres correspond to oxygen (O) atoms. Each cage contains a central atom of chlorine (Cl) (violet), surrounded by four atoms of sodium (Na). In tugtupite, an additional bond between Na and the bridging oxygen between Si and Be tetrahedra leads to a five-fold coordination of Na (*Finch et al., 2016*).

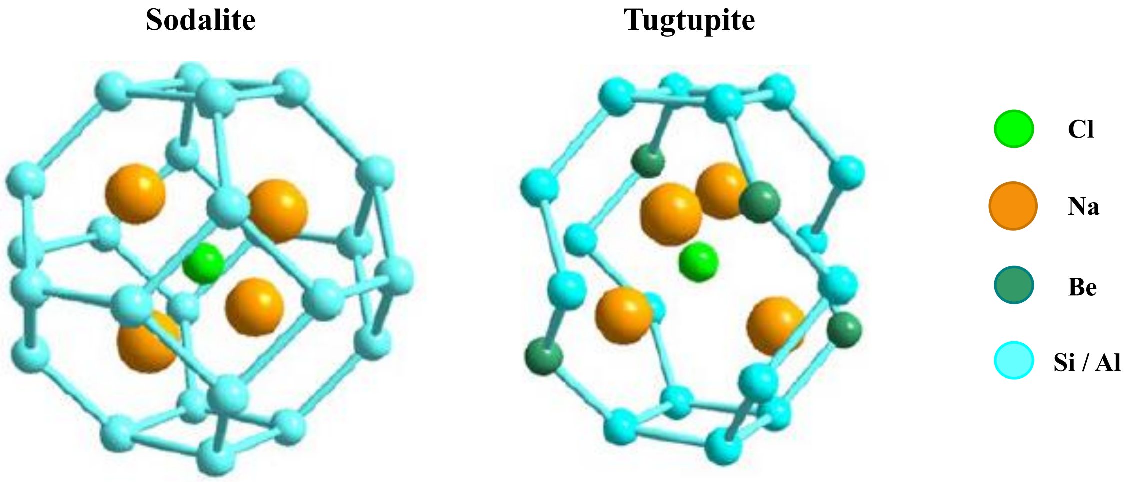

Sodalite

Tugtupite

Figure 10: Structural representation of sodalite and tugtupite without oxygen atoms. The distortion of SiO_4, AlO_4, and BeO_4 tetrahedra in tugtupite is clearly observed (*Blumentritt & Fritsch, 2021*).

Tugtupite can occur in transparent, translucid, or opaque crystals but it is mostly found as massive aggregates (*figure 11*). Well-formed crystals are relatively rare, only a few specimens have been discovered (*figure 12*). These crystals are typically short, prismatic and colorless to pale pink, measuring a few millimeters (*Mindat, 2025*). They are often found growing on the walls of cavities in massive tugtupite (*Sørensen et al., 1971; Jensen & Petersen, 1982*).

Figure 11: Pink tugtupite on matrix, 16 × 12 × 3.6 cm, from Kvanefjeld, Ilímaussaq, West Coast of Greenland. Sample No. 16865 (ENSMP 16865) – display O78, from the collection of the Mineralogy Museum, Mines Paris - PSL. The background has been removed for clarity. Photograph by Claire Chapuis.

Figure 12: Pale pink to colorless tugtupite crystals with brown crystals of helvine from Taseq Slope, Ilímaussaq complex, Kujalleq, Greenland. Field of view: 3.5 mm. Photograph by Tony Peterson (*mindat.org/photo-670845.html*, *2025*).

Mineralogical characteristics

When pure, tugtupite has a specific gravity of 2.34 +/- 0.01 g/cm^3. However, its specific gravity may vary between approximately 2.30 and 2.57 g/cm^3 due to its association with other minerals and its porosity (*Dragsted, 1970; Sørensen et al., 1971*).

Its hardness ranges from 4 to 7 on the Mohs scale, indicating some inconsistency in the literature. *Dragsted* (1970) and *Jensen & Petersen* (1982) gave values between 6 and 7, whereas *Povarennykh et al.* (1971) reported 5.5 and *Tunzi & Pearson* (2008) reported a hardness of 4. Typically, hardness is measured on single-crystal; however, the possible presence of associated minerals within the tugtupite samples may have influenced some of these measurements, leading to higher or lower reported values.

Tugtupite exhibits distinct cleavage parallel to {110} and {101} (*Danø, 1966*), also a fair cleavage parallel to {100}, corresponding to the {110} cleavage observed in sodalite (*Dragsted, 1970; Sørensen et al., 1971; Jensen & Petersen, 1982*).

Optical characteristics

Tugtupite is uniaxial and optically positive. Its refractive indexes range from 1.495 to 1.502, with a birefringence of 0.005 +/- 0.002. Due to its uniaxial optical character, tugtupite exhibits pleochroism. The dichroism is most visible in red tugtupite, showing a darker purplish red and a lighter orangey-red hue (*Dragsted, 1970*).

Luminescence

The luminescence of tugtupite was first described by *Dragsted* (1970), who reported an "apricot" color luminescence under long-wave ultraviolet (LWUV) radiation and a weaker "salmon-red" under short-wave ultraviolet (SWUV) radiation.

Povarennykh et al. (1971) also described a yellow-orange luminescence under LWUV radiation. Their spectral measurements revealed that this emission is composed of eleven narrow, regularly spaced bands (*figure 13*), separated by approximately 568 cm^{-1}, corresponding to the typical vibrational energy of S_2^- polyanion.

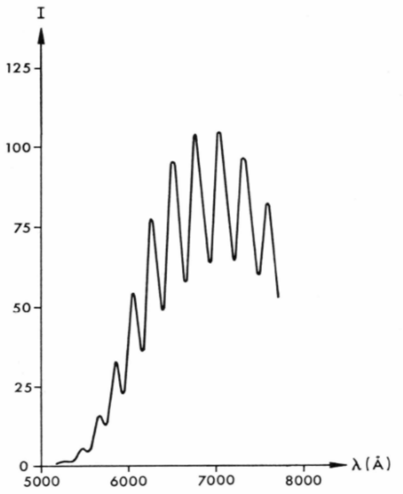

Figure 13: Luminescence spectrum of tugtupite showing eleven narrow bands characteristic of the vibrational energy levels of the S_2^- polyanion (*after Povarennykh et al., 1971*).

Later, *Jensen & Petersen* (1982) reported that red tugtupite specimens display a dark cyclamen-red luminescence under SWUV and a cinnabar-red to light cyclamen-red luminescence under LWUV excitation.

Gaft et al. (2009) identified five distinct luminescent emissions: yellow-orange, red, green, blue, and violet. The origin of the luminescence was initially suggested by *Sørensen et al.* (1971), who attributed the luminescence to sulfur polyanions (S_2^-) occupying chlorine vacancies in the crystal lattice. Subsequent studies into similar aluminosilicates minerals such as sodalite and scapolite, suggesting that polyanions could play a role in producing the yellow-orange luminescence (*Povarennykh et al., 1971; Gaft et al., 2009; Friis, 2011*). Recently, *Blumentritt et al.* (2020) confirmed that S_2^- is indeed the cause of orange luminescence in scapolite, strongly supporting the same hypothesis in tugtupite.

Under SWUV excitation, *Gaft et al.* (2009) observed that the red luminescence of tugtupite is characterized by a broad emission band centered at 670 nm (*figure 14*). This feature has been attributed to the substitution of tetrahedral Al^{3+} by Fe^{3+} — a process also observed in other aluminosilicates where Fe^{3+} substitutes for either Al^{3+} or Si^{4+} like in sodalite-hackmanite (*Gaft et al., 2009; Warner & Andersen, 2012; Blumentritt & Fritsch, 2021*). Additional colors could result from trace impurities within the crystal structure. Specifically, Mn^{2+} produces two types of green luminescence centers with narrow emission bands at 495 and 510 nm (*figure 15, respectively (a) & (b)*), while the combined presence of Ce^{3+} and Eu^{2+} gives rise to two violet bands; the first near 340 nm and the second peaking at 410 nm, corresponding to blue-violet emissions (*figure 17*).

UV-blue luminescence bands have also been detected in tugtupite, characterized by broad features peaking at 430 nm (*figure 16*) and between 380-390 nm with a secondary band at 490 nm (*figure 18*). These emissions are likely associated with a mercury-like luminescence center, commonly referred to as S^2. Based on chemical analyses, the potential S^2 luminescence centers in tugtupite could involve Pb^{2+}, Sn^{2+}, Tl^{+}, or Sb^{3+} (*Gaft et al., 2009*).

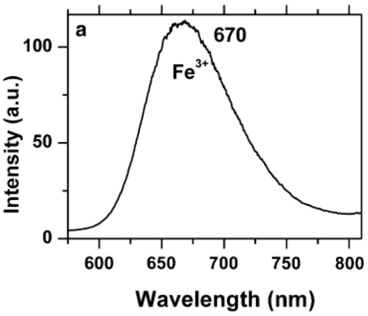

Figure 14: Luminescence spectrum of Fe^{3+} (a) under 266 nm excitation at 300 K, in a tugtupite from Ilímaussaq intrusion (*modified after Gaft et al., 2009*).

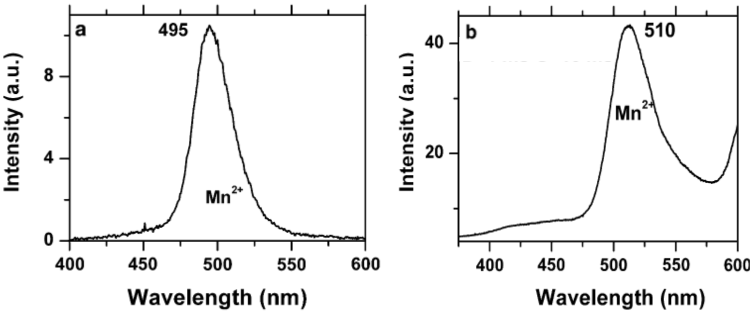

Figure 15: Two different Mn^{2+} luminescence spectra; (a) and (b) under 266 nm excitation at 300 K, in a tugtupite from Ilímaussaq intrusion (*modified after Gaft et al., 2009*).

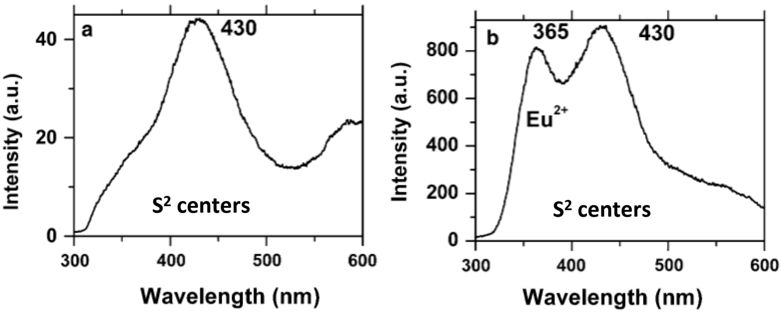

Figure 16: Luminescence spectra of mercury S^2 type centers (a) and combined mercury type S^2 centers and Eu^{2+} (b) under 266 nm excitation at 300 K, in a tugtupite from Ilímaussaq intrusion (*modified after Gaft et al., 2009*).

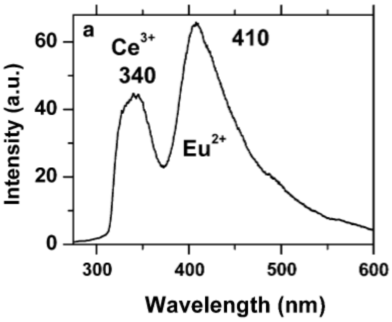

Figure 17: Luminescence spectra of second type of Ce^{3+} and Eu^{2+} under 266 nm excitation at 77 K in a tugtupite from Kola Peninsula (*modified after Gaft et al., 2009*).

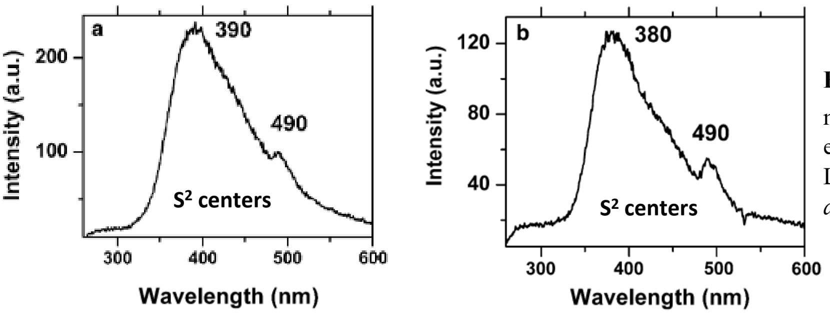

Figure 18: Luminescence spectra of mercury type S^2 centers under 266 nm excitation at 77 K in a tugtupite from Lovozero intrusion (*modified after Gaft et al., 2009*).

Under LWUV excitation, tugtupite typically exhibits a yellow-orange emission. The corresponding spectrum is characterized by a broad band extending from approximately 500 to 700 nm, with a maximum intensity around 600 nm (*figure 19, (a)*). The excitation spectrum peaks in the UV-violet region at about 382 nm (*figure 19, (b)*). The vibronic structure of (S_2^-) is clearly observable (*figure 19, (c)*) and tends to be responsible of the yellow-orange luminescence in tugtupite.

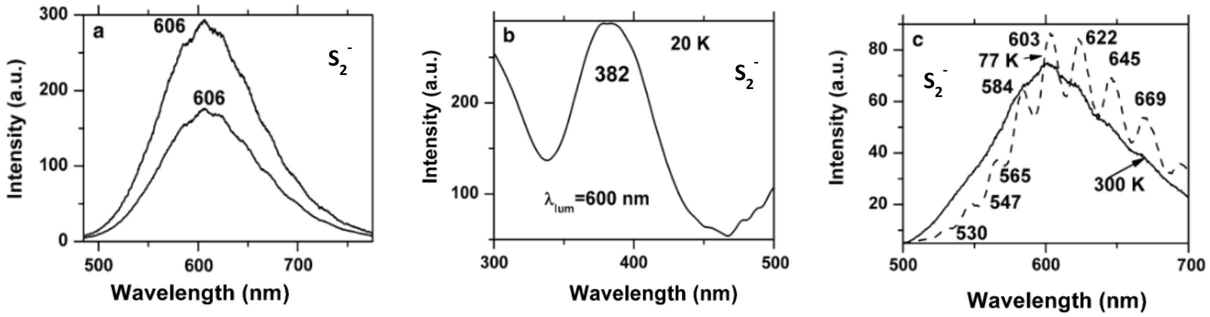

Figure 19: Luminescence and steady excitation of S_2^- spectra under 355 nm excitation: with different decay times and gates at 300 K (a), excitation at 300 K (b) and comparative spectra at 300 K and 77 K (c) in a tugtupite from Ilímaussaq intrusion (*modified after Gaft et al., 2009*).

Overall, the luminescence behavior of tugtupite reflects the interplay between intrinsic structural centers (notably S_2^- polyanions in Cl-vacancies) and extrinsic activators such as Fe^{3+}, Mn^{2+}, and rare-earth elements (REE). This complex combination of mechanisms explains the wide spectral diversity of luminescence, ranging from violet to red emissions under UV excitation.

Phosphorescence

Phosphorescence in tugtupite has been rarely documented in the literature. In most cases, it is not visible to the naked eye (*Tunzi & Pearson, 2008; Gao & Sun, 2023*). However, *Robbins* (1983) reported occasional eye-visible blue-white phosphorescence, similar to that observed in hackmanite. To further characterize the phosphorescence of tugtupite, *Gao & Sun* (2023) examined a 1.76-ct faceted pink tugtupite of an unknown locality, using a SYNTHdetect diamond-screening instrument capable of detecting very short-lived phosphorescence invisible to the eye. The sample displayed an intense yellow phosphorescence immediately after UV excitation, which gradually faded over time. A red hue appeared after about 4.7 ms, and by 17 ms, the yellow emission had almost disappeared. The overall phosphorescence became faint by 30 ms and was barely visible at 40 ms. To analyze the color evolution, the authors performed "RGB" (red, green, blue) color-channel analysis. It showed that red contributed the most to the emission, followed by green, with blue playing only a minor role. As a result, the overall phosphorescence of the tugtupite was described as orangey-red.

Inclusions

Colorless and irregular crystals, along with fluid inclusions, have been reported in tugtupite (*Sobolev et al., 1970; Gao & Sun, 2023*). These two-phase fluid inclusions, occurring in small irregular groups, are considered relics of tugtupite formation, trapped during crystallization at temperatures between 440 °C and 460 °C. Healed fractures are secondary inclusions formed during recrystallization. These high-temperature inclusions, often arranged in "chains" with "unlacing" features, homogenize at temperatures between 240 °C and 260 °C (*Sobolev et al., 1970*).

Color, origin of the color

Tugtupite is usually pink, pinkish red to deep red, and more rarely occurs as colorless or white (*Sørensen et al., 1971*). Very light to light blue specimens have been discovered on the Kvanefjeld Plateau, but they are quite rare, with fewer than ten cabochons reported (*Jensen & Petersen, 1982*). As for luminescence, *Sørensen et al.* (1971) suggested that sulfur anions might also play a role in the coloration of the mineral, while the involvement of radiation centers has likewise been proposed as an origin of color. *Povarennykh et al.* (1971), supposed that the "crimson" color of tugtupite is not only due to S_2^- centers, which are responsible for its luminescence, but also to other, less thermically stable radiation centers, such as $(SO_4)^{2-}$, similar to that identified in ussingite.

Photochromic behavior

Definition of photochromism

The term "photochromism", also known as "tenebrescence", refers to a reversible change of color of a chemical species between two forms, called the "stable" form and the "unstable" or "metastable" form. This change occurs through the absorption of electromagnetic radiation (typically in the ultraviolet range), which allows the transition to the "metastable" state. Then by irradiation with light (usually in the visible range) or through a thermal reaction (depending on the type of photochromism), the material reverts to its stable form. The stone acquires a color when exposed to light rich in ultraviolet rays, such as daylight, which gradually fades after exposure, taking from a few minutes to a few days (*Irie, 2000; Blumentritt, 2021; Piard, 2023*).

Regarding tugtupite, the term *"change of color"* is not appropriate, as it is not the hue that changes during the photochromic process, but rather the value (i.e., the lightness or darkness of a color) according to the Munsell color system (*Munsell Color, consulted 05/02/2026*). In fact, when the gemstone is exposed to UV radiation, its luminosity decreases, resulting in a more intense coloration.

Photochromism applied to tugtupite

All known colors of tugtupite exhibit reversible photochromic behavior; no specimen has ever been reported with a permanently stable color (*Blumentritt & Fritsch, 2021*). Typically, their body color changes from light to dark reddish purple, and in some cases from white when kept in the dark to dark red, reddish purple, or purplish red upon exposed to UV or X-ray radiation

(*Sørensen et al., 1971; Jensen & Petersen, 1982; Blumentritt & Fritsch, 2021*). When briefly exposed to artificial visible light or standard daylight such as D65, the stones return to their original color within a few minutes (*Blumentritt & Fritsch, 2021*). Annealing tugtupite about 600-700°C destroys photochromism resulting in a colorless tugtupite (*Warner & Andersen, 2012*).

In the case of blue tugtupite, only a few specimens have been reported. When these light blue stones are exposed under UV radiation, their body color changes from light blue to light red (*Jensen & Petersen, 1982*). However, the exposure must remain under 30 seconds; longer exposure causes the light blue tugtupite to develop a light red hue that stays after fading (*Jensen & Petersen, 1982*).

The first UV-Vis spectroscopic study of tugtupite was provided by *Povarennykh et al.* (1971). Their spectra (*figure 20*) showed that the pink coloration of tugtupite result from a broad absorption band in the visible region between 440 and 600 nm, with a maximum peaking at 510 nm (*figure 20, curve a*), that decreases significantly between 600 and 750 nm compared with shorter wavelengths. Heating the sample to 450 °C completely decolorizes the tugtupite, indicating the thermal destruction of the color center. After heating, the spectrum displays a continuum decreasing toward the red region (*figure 20, curve b*).

Subsequent two-hour X-ray irradiation of the decolorized sample partially restores the pink color and the associated absorption band, although the intensity remains lower than that of the natural sample (*figure 20, curve c*). *Povarennykh et al.* (1971) also noted that prolonged irradiation enhances both the color and the absorption band intensity. This behavior demonstrates that the color centers produced by irradiation are unstable.

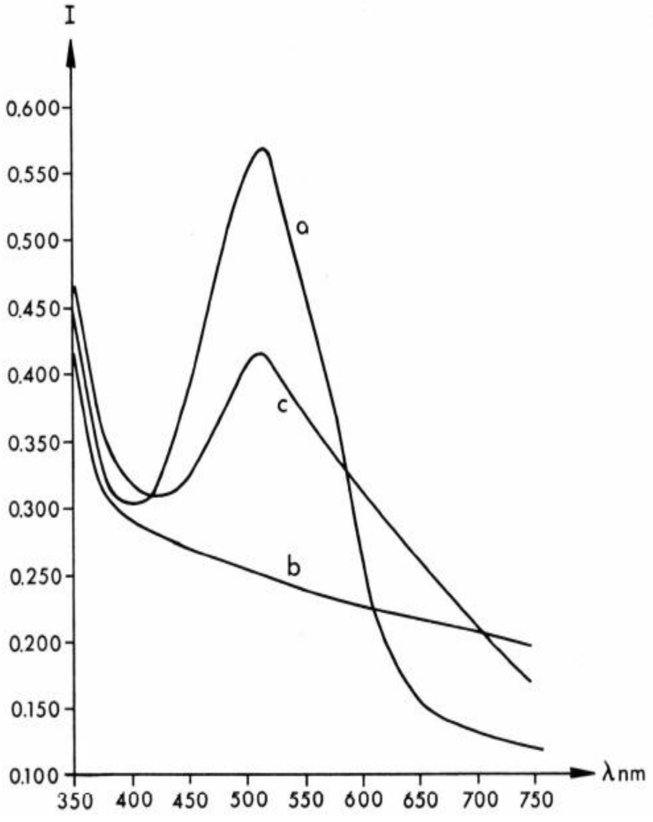

Figure 20: Spectral absorption curves of tugtupite sample from Ilímaussaq, South Greenland, between 350 and 750 nm. (a) Naturally colored sample; (b) Sample decolorized by heating to 450 °C; (c) Recolored sample after X-ray irradiation (*after Povarennykh et al., 1971*).

UV-Visible analysis of a tugtupite specimen from Greenland obtained by *Blumentritt & Fritsch* (2021) confirmed these findings. Indeed, spectra (*figure 21*) showing the broad band between 440 and 600 nm, with a maximum at 510 nm, consistent with the results of *Povarennykh et al.* (1971) and *Milisenda et al.* (2015). In addition, a smaller band peaking around 380 nm can be observed in both states, with higher intensity in the stable (pink) state. Spectral analysis of the difference spectrum reveals two Gaussian components corresponding to distinct color centers: one peaking near 545 nm, similar to that observed in hackmanite (the photochromic variety of sodalite), and another near 500 nm, responsible for the characteristic red photogenerated color in tugtupite (*Blumentritt & Fritsch, 2021*).

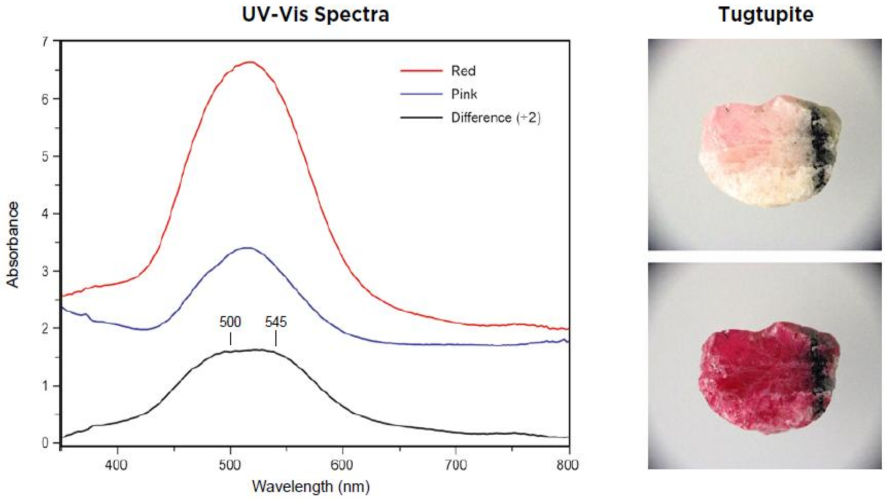

Figure 21: Photographs and absorption spectra of a tugtupite specimen from Greenland, showing the UV-induced change of color value from pink (before UV exposure, *blue curve*) to red (after UV exposure, *red curve*). The difference spectrum (divided by two, *black curve*) highlights two Gaussian bands at approximately 500 and 545 nm, corresponding to photogenerated color centers likely responsible for the red coloration (*after Blumentritt & Fritsch, 2021*).

Gao & Sun (2023) also recorded comparable UV-Visible spectra, with a broad absorption band between 440 and 600 nm peaking at 515 nm in the pink state and 520 nm in the red photogenerated state, as well as a 390 nm band more intense in the stable pink state (*figure 22*).

The main difference with *Blumentritt & Fritsch* (2021) is that *Gao & Sun* (2023) did not report the two Gaussian bands in the photogenerated red state, corresponding to the color centers near 500 nm and 545 nm previously described by *Blumentritt & Fritsch* (2021).

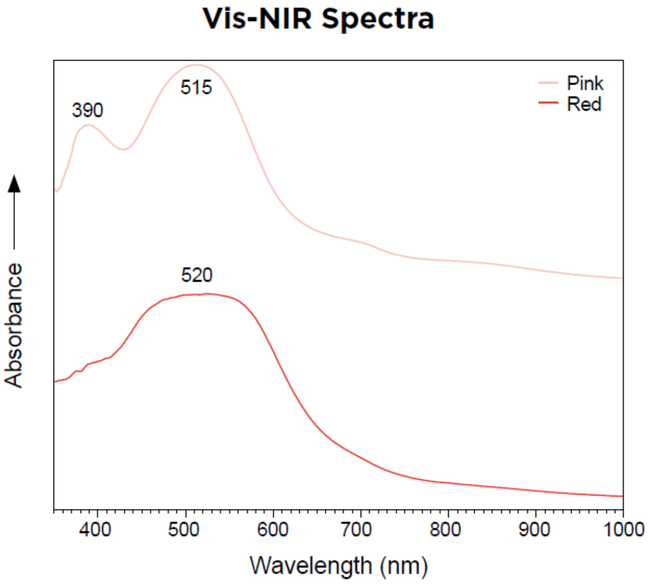

Figure 22: Vis-NIR spectra of a tugtupite sample in both its pink (before UV exposure) and red (after UV exposure) states, show differences in the major absorption features (*after Gao & Sun, 2023*).

Overall, the results of *Povarennykh et al.* (1971), *Blumentritt & Fritsch* (2021), and *Gao & Sun* (2023) consistently confirm that two distinct color centers are responsible for the red coloration observed in tugtupite. *Blumentritt & Fritsch* (2021) further proposed that the mechanism of photochromism in tugtupite may be similar to that of hackmanite and scapolite, due to significant similarities in their structure and chemical composition, particularly the presence of sulfur. It could result from an electron trapped in a Cl vacancy associated with sulfur polyanions (S_2^{2-} and/or S_2^{-}). The two Gaussian bands observed in the difference absorption spectrum (*figure 21, black curve*) may correspond to two distinct local environments of the trapped electron, possibly responsible for the two-color centers; typically observed in tugtupite.

CHAPTER II: Materials and Methods

Materials

Sixteen samples have been used in this study and come from the three known geographic origins; Greenland, Russia, and Canada. They have been either bought as “tugtupite” and gathered thanks to generous donations and loans from the collection of Mr. R. Muller, Pr. E. Fritsch, Dr. I. Lykova, Mr. M. T. M. Haris and Mr. S. Milliner. Few others are from my personal collection. All the samples are rough with their matrix and their colors ranging from light pink to purplish pink.

It is important to take into consideration that tugtupites from Canada and Russia are particularly rare and difficult to find. Moreover, their smaller crystals raise significant challenges for analysis.

Figure 23: Overview of all the samples from the three localities used in this study. Photograph by Claire Chapuis.

Samples TU01 to TU05 and TU11 to TU16 are classified as F-type stones according to GIA’s sample collecting protocols (*Vertriest et al., 2019*), as they were obtained from reliable secondary sources on the international market. Samples TU06 to TU10 are classified as Z-type stones due to the lack of information on their collection conditions.

Table I: Tugtupite samples collected for this study.

Identification Name	*Shape, Type*	*Mass (ct)*	*Dimensions (mm)*	*Origin and name of the owner*	Locality	*Photographs**
TU01	Shapeless, Thick section	10.06	43.00 x 15.51 x 1.59	Donation from R. Muller	Narsap Ilua, Kujalleq, **Greenland**	
TU02	Shapeless, Thick section	2.44	13.22 x 10.22 x 3.17	Donation from R. Muller	Narsap Ilua, Kujalleq, **Greenland**	
TU03	Shapeless, Thick section	3.06	18.59 x 9.07 x 2.27	Donation from R. Muller	Narsap Ilua, Kujalleq, **Greenland**	
TU04	Shapeless, Thick section	1.98	18.45 x 8.46 x 2.28	Donation from R. Muller	Narsap Ilua, Kujalleq, **Greenland**	
TU05	Shapeless, Thick section	2.00	14.46 x 7.72 x 2.24	Donation from R. Muller	Narsap Ilua, Kujalleq, **Greenland**	
TU06	Shapeless, Thick section	3.17	14.08 x 12.79 x 2.18	Author personal collection C. Chapuis	**Greenland**	
TU07	Shapeless, Rough	4.88	15.47 x 11.29 x 4.31	Loan from Pr. E. Fritsch	**Greenland**	
TU08	Shapeless, Thick section	1.49	16.32 x 5.70 x 2.17	Loan from Pr. E. Fritsch	**Greenland**	
TU09	Shapeless, Rough	67.28	48.00 x 27.00 x 5.61	Loan from Pr. E. Fritsch	**Greenland**	
TU10	Shapeless, Rough	6,82	18.02 x 10.73 x 7.21	Loan from M. T. M. Haris	Unknown locality	
TU11	Shapeless, Rough	10.06	17.99 x 13.77 x 8.43	Loan from I. Lykova	Mont Saint-Hilaire **Canada**	
TU12	Shapeless, Rough	6.37	14.87 x 13.24 x 7.02	Loan from I. Lykova	Mont Saint-Hilaire **Canada**	
TU13	Shapeless, Rough	44.49	24.67 x 21.61 x 18.79	Loan from I. Lykova	Mont Saint-Hilaire **Canada**	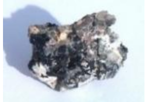

TU14	Shapeless, Rough	0.22	3.92 x 3.39 x 3.34	Author personal collection C. Chapuis	Karnasurt, Lovozero, Kola **Russia**	
TU15	Shapeless, Rough	0.54	6.13 x 6.00 x 4.00	Author personal collection C. Chapuis	Shkatulka pegmatite, Alluaiv, Lovozero, Kola **Russia**	
TU16	Shapeless, Rough	352.45	50.0 x 40.0 x 20.0	Loan from S. Milliner	Loparskij pereval Chibiny, Kola **Russia**	

*Photographs have been taken by the author.

Methods

Thick sections preparation

First, seven out of sixteen samples (TU01, TU02, TU03, TU04, TU05, TU06, and TU08) were prepared to allow light transmission and to isolate as much of the tugtupite-bearing areas as possible from the surrounding rock. This preparation was performed in the dedicated laboratory at Nantes University. The samples were first cut using a diamond-blade saw, then polished into thick sections using a lapidary wheel and a series of diamond discs with varying grain sizes, until obtained a final thickness between 1.59 and 3.17 mm.

Classical Gemology instruments

Standard gemological tools were used for the study

Refractive indexes were measured using a refractive liquid with an index of 1.789 and a Gemax ECO refractometer, equipped with a synthetic cubic zirconia optical prism, a 32 mm eyepiece, a removable polarizer and a monochromatic LED light source. The instrument is calibrated for a refractive index range of 1.350 to 1.810, with a precision of +/- 0.003. A gemological polariscope with an integrated light source was used to determine the optical properties of the samples. Observations were made between crossed polarizers. Specific gravity measurements were acquired using a Mettler Toledo hydrostatic balance with a precision of +/- 0.01 ct. Finally, luminescence was assessed using two Vilber Lourmat VL-215.LC ultraviolet lamps (15 W for each lamp): one emitting short-wave ultraviolet radiation (SWUV, 254 nm) and another long-wave ultraviolet radiation (LWUV, 365 nm). The samples were observed at a 10 cm distance from the tubes, in a dark environment and on a dark, inert, and non-reflective background.

Laboratory equipment

Infrared Spectroscopy

Fourier-Transform Infrared spectroscopy (FTIR) measurements were performed using a Bruker Vertex 70 FTIR spectrometer equipped with a CaF_2 beam splitter and a MIR light source. Spectra were recorded in the 7000-400 cm^{-1} range using 100 to 200 scans with a spectral resolution of 4 cm^{-1} in transmission or reflection mode, depending of the sample. The reflection was parameter in specular mode when the transmission mode was not possible.

Raman Spectroscopy

Raman spectra were measured using a Bruker MultiRAM Fourier-Transform Raman spectrometer, with an Nd:YAG laser at 1064 nm and a LN-Ge diode detector. The nominal laser power was 2 W, and the spectral resolution ranged between 4 and 5 cm^{-1}. Spectra were recorded from 50 to 4000 cm^{-1} over 200 scans.

Micro-Raman Spectroscopy

Three different micro-Raman instruments were used:

- Samples TU01, TU05, TU07, TU11, TU12, TU13, TU14, and TU15 were analyzed with a Renishaw InVia confocal Raman microscope equipped with a 514 nm laser excitation (operating at a power of 10%) and fitted with a 20x objective. The spectrometer used a diffraction grating of 1800 grooves/mm. Spectra were acquired in the 100-1300 cm^{-1} range with a spectral resolution of < 1 cm^{-1}, over an accumulation of 15 accumulations, and a 5-seconds acquisition time.
- Samples TU13, TU15, and TU16 were measured at the French Gemological Laboratory (LFG) using a Renishaw InVia Raman microscope with a 514 nm Ar^+ laser (DPSS Diode Pump Solid State, with a power of 100 mW, operated at 10%). The spectrometer used a diffraction grating of 1800 grooves/mm. Spectra were acquired in the 0-1000 cm^{-1} region with a resolution of < 1 cm^{-1}, over 5 to 10 accumulations, and acquisition times ranging from 1 to 10 seconds.
  Photoluminescence (PL) was measured in samples TU13 and TU15 between a range of 700-1200 cm^{-1} (approximately from 8333 to 14285 nm), using a laser power set at 10% for 100 mW, with 5 accumulations and an acquisition time of 10 seconds per accumulation.

- Samples TU08, TU12, and TU13 were analyzed using a T64000 Horiba Jobin-Yvon spectrometer in backscattering configuration, with a 514.5 nm argon excitation laser, fitted with a microscope and a 50x objective. Spectra were recorded between a range from 200 to 1400 cm^{-1}, with 5 to 10 scans, acquisition times ranging from 2 to 30 seconds, and 5 accumulations.

Chemical Analyses (SEM IT510)

- **EDXRF**

Energy-Dispersive X-Ray Fluorescence (EDXRF) chemical analyses were performed in GGTL Laboratories Switzerland, using a ThermoFisher Scientific ARL Quant'X system, equipped with a Rh X-ray tube for excitation and a 1000 µm-thick silicon drift detector cooled thermoelectrically via the Peltier effect (a three-stage module generating a λ of ≈ 120 °C), using total element normalization (Na → U), with 300 seconds of real-time acquisition per condition

(9 filters), under vacuum for light elements. Measurements were performed on the sample stage, with optimal geometry (± ≈ 1°) relative to the angle of incidence of the excitation beam with the stage (ϴ = 45°), as well as with the detector (same ϴ), samples on 4 µm Prolene® film, analyzed in rotation to reduce diffraction artifacts and analyze a defined circular area of ∅ 4 mm.

- **SEM IT510**

Sample preparation for SEM analysis

Before placing the samples in the scanning electron microscope (SEM), they were prepared for metallization. First, the sample holder (plot) was cleaned with ethanol and polished to remove any remaining material that could affect the results. A small amount of carbon paste was applied to both the sample holder and thick sections previously prepared, which had also been cleaned with ethanol. The sample was then pressed onto the sample holder to make sure it was positioned parallel to the surface. To establish electrical continuity between the sample and the plot, a layer of silver paint was applied, forming a conductive bridge. Finally, a thin layer of carbon was coated on the sample to provide a conductive surface, allowing electrons to escape during SEM imaging.

SEM analysis processus

Samples were placed in a JEOL JSM IT510 scanning electron microscope (SEM) working at 15 kV for a beam current in the 1nA range, providing sufficient statistics for the acquisition of spectra and maps by the integrated EDS spell out detector. Images were captured using either an Everhart-Thornley secondary electron detector or a dual PN junction backscattered electron detector.

UV-Vis-NIR Absorption

Ultraviolet-Visible-Near InfraRed (UV-Vis-NIR) absorption spectra were measured using a MagiLABS GemmoSphere spectrometer, equipped with an integrating sphere and operating in transmitted light mode. The spectral range covered a range from 365 to 1000 nm, with a spectral resolution of 1 nm, and an average of 100 scans. Integration times were recorded using the “AutoScan” mode and varied from 330 to 1340 seconds, depending on the sample.

Luminescence Spectroscopy

Luminescence spectra measurements were performed using a Horiba Scientific Fluorolog-3 spectrofluorometer equipped with a 450 W xenon lamp as the light source and a Hamamatsu R13456 photomultiplier tube as the detector. Corrected emission spectra were acquired in the 320-800 nm range, using a 1 nm increment, a 5 nm slit, and an integration time of 0.2 seconds.

Emission spectra were recorded under two excitation wavelengths:

- At 254 nm, with a 295 nm cut-off filter.

- At 365 nm, with a 400 nm cut-off filter.

Excitation spectra were acquired in the 250-500 nm range with a 385 nm filter, for different emission wavelengths depending on the sample. These spectra were acquired with a 0.1 second integration time, a 1 nm increment, and a slit of 2 nm, except for the following exceptions:

- TU05 (421 nm), TU07 (427 nm), and TU08 (425 nm): 5 nm slit.
- TU02 (647 nm) and TU09 (681 nm): 6 nm slit.

Phosphorescence Spectroscopy

Phosphorescence was tested on TU05, TU07 and TU08 and was recorded with a Horiba Scientific Fluorolog-3 spectrofluorometer. The excitation wavelength was set at 254 nm and the emission at 680 nm, with a slit of 10 nm. Measurements were performed using 10 to 20 flashes count, with an 80 to 150 ms time per flash, and a detection window of 1 ms.

Photography and photomicrography

Photographs were taken using an Olympus OM-D E-M10 Mark III camera fitted with a 14-42 mm f/3.5-5.6 II R lens.

Photomicrographs were taken at the French Gemological Laboratory (LFG) using a Nikon SMZ25 microscope, with magnifications ranging from 1.5x to 20x.

CHAPTER III: Results

Tugtupite

Classical Gemology

Classical gemology analyses were conducted on all samples from Greenland, as well as on one sample from Russia. Due to the fragility and very small crystal size of samples TU11 to TU15 — corresponding to tugtupites from Canada and Russia — analyses on these samples could not be performed.

Examination under crossed polarizing filters revealed variable optical behaviors related to the degree of crystallinity of each sample (*see Table II*). Translucent, partially microcrystalline samples (TU07 and TU08) displayed light reestablishment at every quarter turn, consistent with anisotropic behavior. In contrast, polycrystalline samples (TU01 and TU05) showed continuous light reestablishment due to the presence of intergrown microcrystals, while fully opaque specimens (TU02, TU03, TU04, TU06, TU09, TU10, and TU16) did not allow light transmission. These observations confirmed the anisotropic character of tugtupite, which is not visible in polycrystalline or opaque material.

Specific gravity values were measured and yielded a range of 2.26 to 2.60 g/cm^3, this broad range of values probably resulting from the association of tugtupite with other minerals. Refractive indexes, where determinable (either by direct or distant reading, depending on surface quality), indicated uniaxial positive optical character, ranging from 1.492 to 1.500, with the lowest value of 1.480 recorded for TU16.

Finally, consistent with the optical properties of tugtupite, a weak dichroism was observed in several samples (TU02, TU03, TU05, and TU08). It is characterized by two distinct color hues: from light pink to pink in lighter specimens (TU02 and TU03), from pink to purplish-pink in TU05, and from pink to intense pink in TU08.

Table II: Classical gemology description from TU01 to TU10.

Identification Name	*Crossed Polarizers*	*Specific Gravity*	*Refractive Index*	*Birefringence*	*Optical Character*	*Pleochroism Intensity Colors*
TU01	Light at all positions	2.60	1.495	Not determinable	Not determinable	Not visible
TU02	Opaque	2.26	1.492 1.498	0.006	U (+)	Dichroïsm Weak Light pink Pink
TU03	Opaque	2.46	1.492 1.498	0.006	U (+)	Dichroïsm Weak Light pink Pink
TU04	Opaque	2.46	1.497	Not determinable	Not determinable	Not visible
TU05	One part is light at all positions and the other is opaque	2.35	1.496 1.500	0.004	U (+)	Dichroïsm Weak Pink Purplish-pink
TU06	Opaque	2.27	1.495	Not determinable	Not determinable	Not visible
TU07	One part is four times dark and the other is opaque	2.34	1.496 1.500	0.004	U (+)	Not visible
TU08	One part is light at all positions; another is four times dark and the last part is opaque	2.28	1.492 1.498	0.006	U (+)	Dichroism Weak Pink Intense pink
TU09	Opaque	2.41	1.491-1.495	0.004	U (+)	Not visible
TU10	Opaque	2.43	1.500	Not determinable	Not determinable	Not visible
TU16	Opaque	Not determinable	1.480	Not determinable	Not determinable	Not visible

* Samples from TU11 to TU15 are not included in the table, as they were not measurable.

Ultraviolet Luminescence

Luminescence was tested on all samples, except for TU14 and TU15, because of analytical limits. *Table III* shows the results of the luminescence observed in the tugtupite parts of each sample, under short-wave UV (254 nm) and long-wave UV (365 nm).

Table III: Ultraviolet luminescence observation.

Luminescence Parameters	*SWUV 254 nm*	*LWUV 365 nm*	*Identification Name*
Intensity Color Distribution	Very Weak Orangey-red Uneven	None	TU01
Intensity Color Distribution	Very Weak Orangey-red Uneven	None	TU02
Intensity Color Distribution	Faint Orangey-red Uneven	Very Weak Orange Uneven	TU03
Intensity Color Distribution	Faint Orangey-red Uneven	Very Weak Orange Uneven	TU04
Intensity Color Distribution	Very Weak Orangey-red Uneven	None to Very Weak Orange Uneven	TU05
Intensity Color Distribution	Very Weak Orangey-red Uneven	Medium Orange Uneven	TU06
Intensity Color Distribution	Medium Orangey-red Even	Strong Orange Even	TU07
Intensity Color Distribution	Faint Orangey-red Even	Medium Orange Even	TU08
Intensity Color Distribution	Medium Orangey-red Even	Faint Orange Uneven	TU09
Intensity Color Distribution	Faint Orangey-red Uneven	None to Very Weak Orange Uneven	TU10
Intensity Color Distribution	Faint Orangey-red Even	Medium Orange Even	TU11
Intensity Color Distribution	Faint Orangey-red Even	Medium Orange Even	TU12
Intensity Color Distribution	None	None	TU13
Intensity Color Distribution	Not visible, too small	Not visible, too small	TU14
Intensity Color Distribution	Not visible, too small	Not visible, too small	TU15
Intensity Color Distribution	Strong Orangey-red Even	Medium Orange Even	TU16

All analyzed samples exhibited an orangey-red luminescence under short-wave UV (254 nm), with varying intensities from very weak to strong depending on the specimen. Under long-wave UV (365 nm), luminescence ranged from very weak to medium orange (*table III, figure 24*).

Generally, luminescence was stronger under short-wave UV, except for TU06, TU07, TU08, TU11, and TU12, which displayed stronger long-wave emissions. Luminescence distribution was often uneven in samples containing accessory minerals, such as TU01 to TU06. No visible-eye phosphorescence was observed.

These results are consistent with observations of tugtupite luminescence by *Dragsted* (1970) and *Povarennykh et al.* (1971).

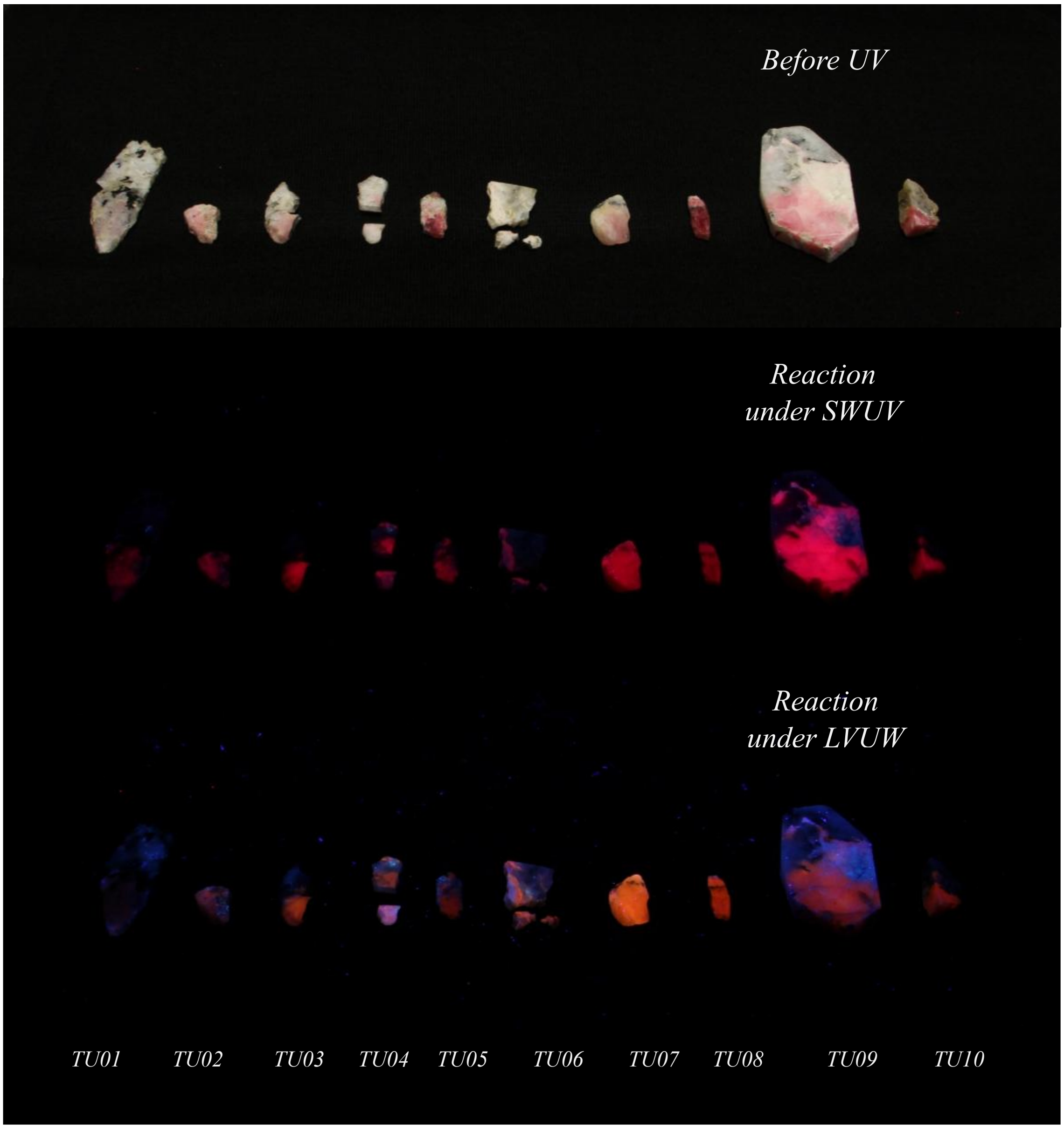

Figure 24: Short-wave and long-wave ultraviolet reactions of TU01 to TU10. The blue part is due to the reflection of the UV lamps on samples. Photographs by Claire Chapuis.

Photochromism behavior

Tugtupite is well known for its photochromic behavior. *Table IV* summarizes the results obtained before and after exposure to short-wave ultraviolet radiation (254 nm). Within a few minutes after ultraviolet excitation, tugtupite samples exhibited a distinct change of the color value from light pink, pink, or intense pink in their stable state to pink, reddish-pink, or intense purplish-pink (*figure 25*).

Table IV: Samples Photochromism Properties Observation.

Identification Name	*Stable color*	*Distribution*	*Time under UV exposition (minutes)*	*Metastable color*	*Distribution*	*Approximately fading time in a dark environment (week)*	*Fading time under exposure to D65 light*
TU01	Light Pink	Uneven	Few seconds to a minute	Pink	Uneven	> 6	Few minutes
TU02	Pink	Uneven	Few seconds to a minute	Darker Pink	Uneven	> 6	Few minutes
TU03	Light Pink	Uneven	Few seconds to a minute	Pink	Uneven	> 6	Few minutes
TU04	Light Pink	Uneven	Few seconds to a minute	Pink	Uneven	> 6	Few minutes
TU05	Intense Pink	Even	Few seconds to a minute	Pinkish Red	Even	6	Few minutes
TU06	Light Pink	Uneven	Few seconds to a minute	Pink	Uneven	5	Few minutes
TU07	Pink	Even	Few seconds to a minute	Dark Pink	Even	5	Few minutes
TU08	Intense Pink	Even	Few seconds to a minute	Intense Purplish Pink	Even	6	Few minutes
TU09	Intense Pink	Even	Few seconds to a minute	Intense Purplish Pink	Even	5	Few minutes
TU10	Pink	Uneven	Few seconds to a minute	Purplish Pink	Uneven	3	Few minutes
TU11	Pink	Even	Few seconds to a minute	Darker Pink	Even	5	Few minutes
TU12	Pink	Even	Few seconds to a minute	Pinkish Red	Even	5	Few minutes
TU16	Pinkish Violet	Even	Few seconds to a minute	Dark Violet	Even	< 1	Few minutes

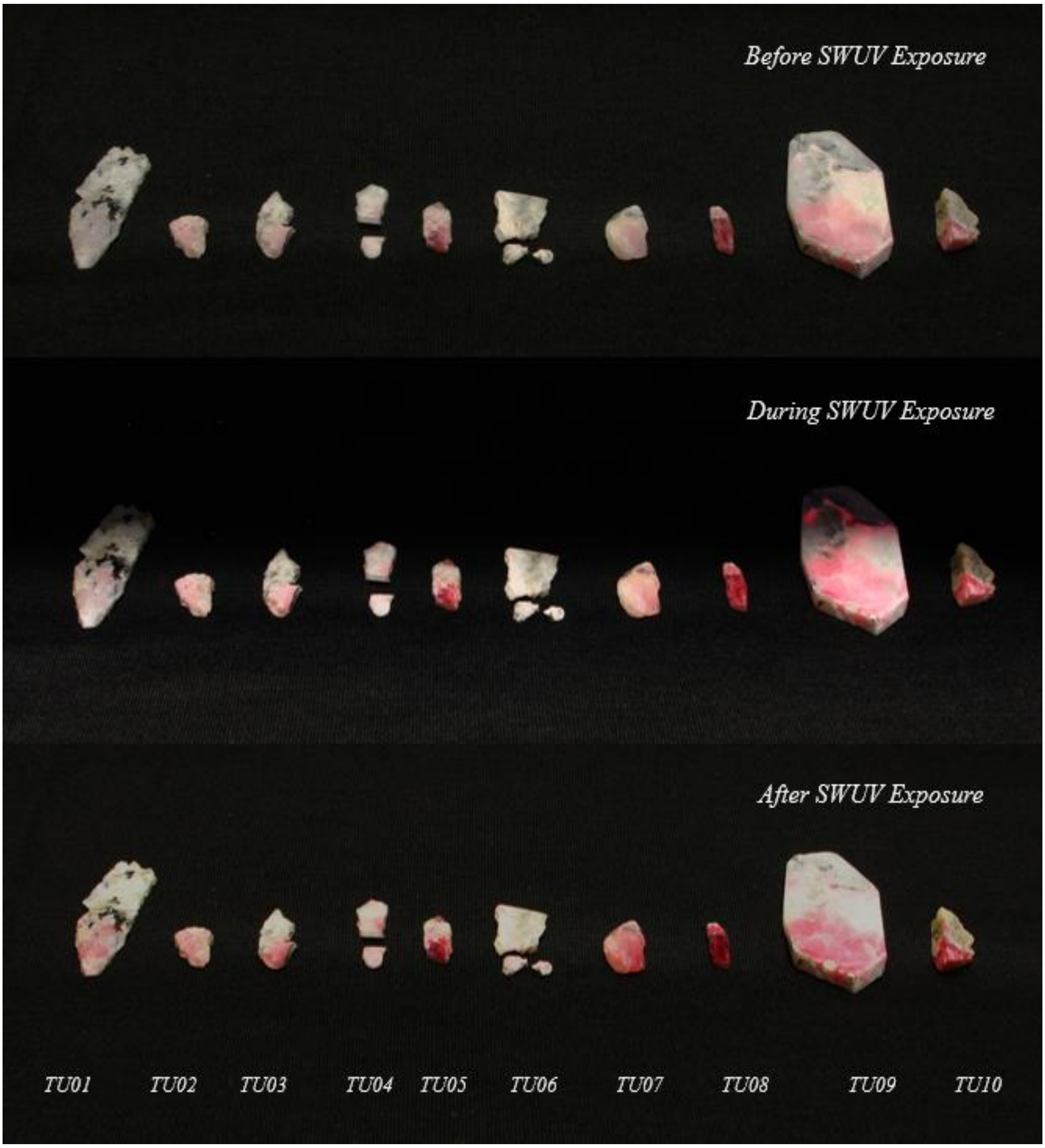

Figure 25: Photochromic process of TU01 to TU10 before, during, and after exposure to short-wave ultraviolet radiation. The exposure time was approximately 2 minutes. Photographs by Claire Chapuis.

After approximately five minutes of UV exposure, the samples reached their maximum color intensity, corresponding to the excited, metastable state (*figure 26, figure 29*).

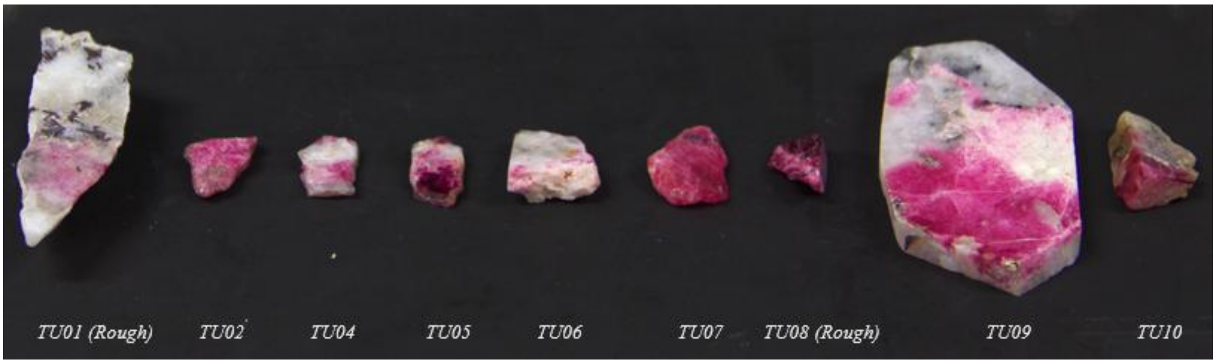

Figure 26: Close-up of a few tugtupite samples after approximately 5 minutes of exposure under short-wave ultraviolet radiation. Past this timepoint, no further darkening was observed. Photograph by Claire Chapuis.

Figure 27: TU12 before exposure to long-wave ultraviolet radiation. Photomicrograph by Claire Chapuis using a Nikon SMZ25 microscope. Field of view: 7.33 mm.

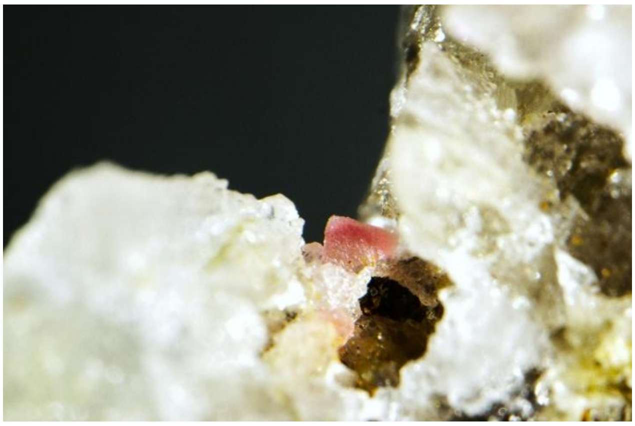

Figure 28: TU12 after approximately 2 minutes of exposure under long-wave ultraviolet radiation. Photomicrograph by Claire Chapuis using a Nikon SMZ25 microscope. Field of view: 7.33 mm.

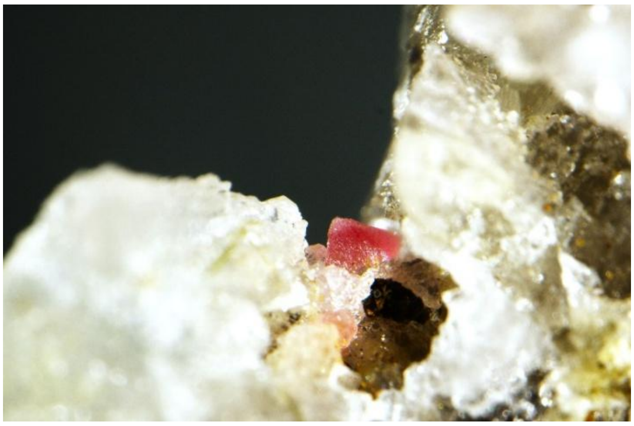

Figure 29: TU12 after approximately 5 minutes of exposure under long-wave ultraviolet radiation. After this time, no further darkening was observed. Photomicrograph by Claire Chapuis using a Nikon SMZ25 microscope. Field of view: 7.33 mm.

Regarding TU11, the color value variation was less pronounced than in other samples, such as the other Canadian specimen, TU12. Nevertheless, photochromic behavior remained clearly observable following UV irradiation exposure. For both TU11 and TU12, luminescence was examined under both short- and long-wave UV radiation. However, for the experimental observation of color evolution, short-wave UV exposure could not be performed, as only a long-wave UV lamp was available at the time of analysis. The specimens were observed under a microscope during the experimental procedure due to their small crystal size (*figure 30*).

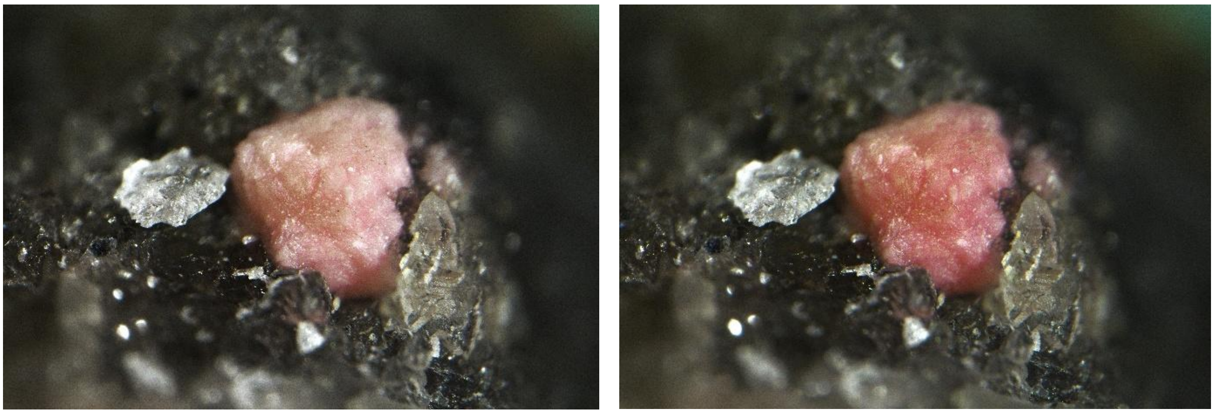

Figure 30: Photochromic process of TU11 before and after exposure to long-wave ultraviolet radiation. Photomicrographs by Claire Chapuis using a Nikon SMZ25 microscope. Field of view: 7.33 mm.

As observed for luminescence, color distribution was influenced by the association of the tugtupite matrix with other minerals. The darkened specimens gradually reverted to their original color when stored in darkness for three to more than six weeks, or within a few minutes when exposed to standard natural daylight (D65) (*see table IV*).

The photochromic behavior observed in this study is consistent with previously reported descriptions in the literature (*Milisenda et al., 2015; Blumentritt & Fritsch, 2021; Gao & Sun, 2023*). All the samples studied here displayed a reversible change of the color value from light-to-medium-to-intense pink to dark-pink, intense purplish-pink or pinkish-red color.

Regarding the color fading in darkness, earlier studies have reported recovery times ranging from a few minutes (*Blumentritt & Fritsch, 2021; Gao & Sun, 2023*) to several months or even years (*Milisenda et al., 2015*). In the present work, the samples returned to their stable color within several weeks, closer to the observations of *Milisenda et al.* (2015).

Inclusions

Microscopic observation of few samples revealed characteristic inclusions previously documented in the literature (*Sobolev et al., 1970; Gao & Sun, 2023*). TU05 contained a non-identified, partially eroded colorless crystal (*figure 31*). Fluid inclusions and typical healed fractures were observed in samples TU01 (*figure 32*) and TU08 (*figure 33*).

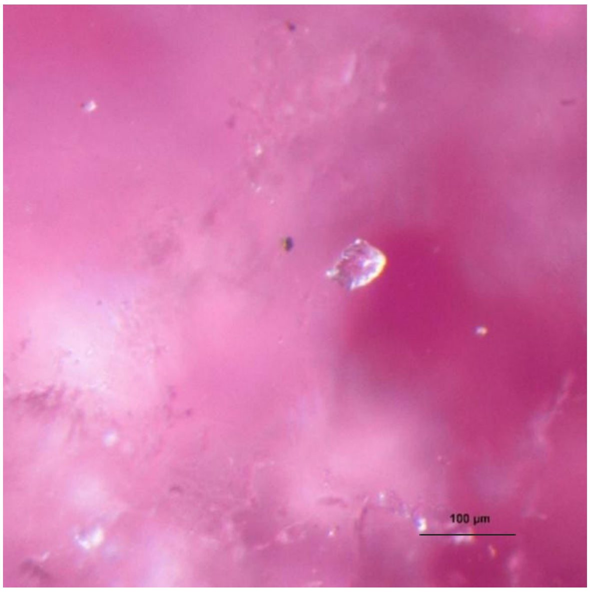

Figure 31: Photomicrograph of TU05 crystal inclusion by Claire Chapuis using a Nikon SMZ25 microscope. Crystal has an irregular shape and seems to be partially eroded.

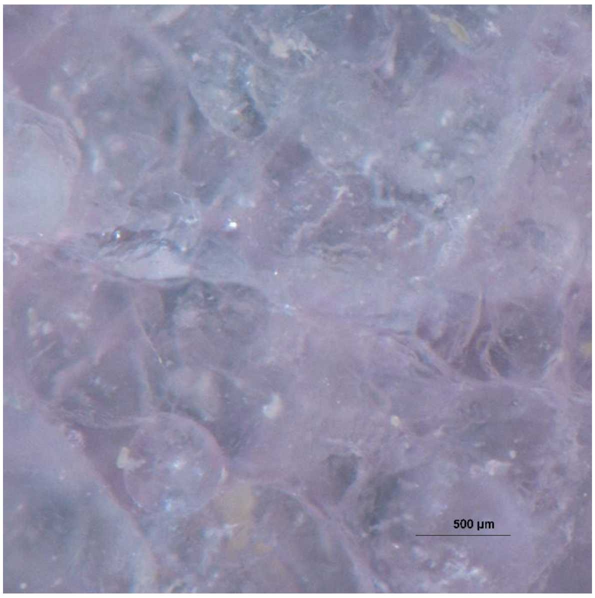

Figure 33: Photomicrograph of TU01 healed fracture inclusions by Claire Chapuis using a Nikon SMZ25 microscope.

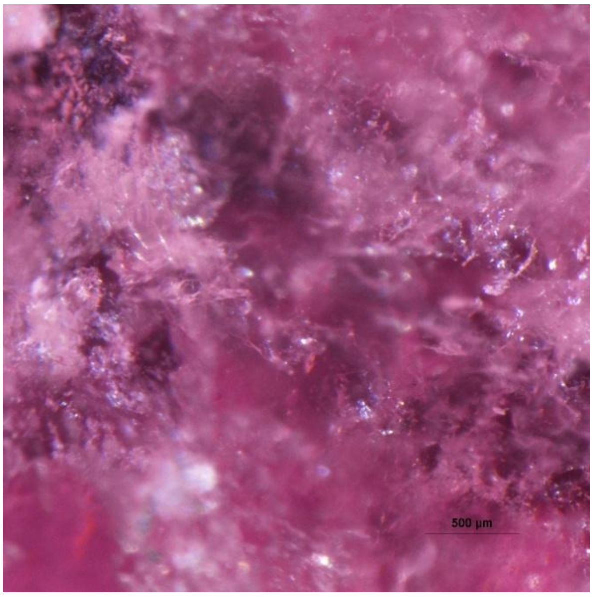

Figure 32: Photomicrograph of TU08 healed fracture inclusions by Claire Chapuis using a Nikon SMZ25 microscope.

Laboratory Gemology

To obtain a detailed characterization of the samples and to identify the tugtupite-bearing areas, several analytical techniques were used. However, some specimens — particularly those from Canada and Russia — could not be analyzed with all instruments, primarily due to their size and fragility. For these samples, only micro-Raman spectroscopy was performed to characterize pink crystals, which was presumed to be tugtupite.

Fourier-transform InfraRed Spectrometry

Fourier-transform infrared (FTIR) spectra were acquired for all Greenland tugtupite specimens. Transmission spectra (*figure 34*) were recorded for samples TU01, TU03, TU05, TU07, and

TU08, which were sufficiently crystalline to allow light transmission through the material. To the best of the author's knowledge, the FTIR spectra presented in this study represent some of the first published infrared characterizations ever reported for tugtupite.

In these spectra, a set of broad absorption bands were observed between 1850 and 2200 cm^{-1}. More specifically, weak peaks were detected at approximately 1872, 2012, 2060, 2114, and 2130 cm^{-1}, with three better-defined bands centered at 1990, 2091, and 2175 cm cm^{-1}. Additionally, the H_2O broad band (water band) was visible between 3100 and 3700 cm cm^{-1} in all samples, with variable intensity reflecting differences in structural water content incorporated during crystallization.

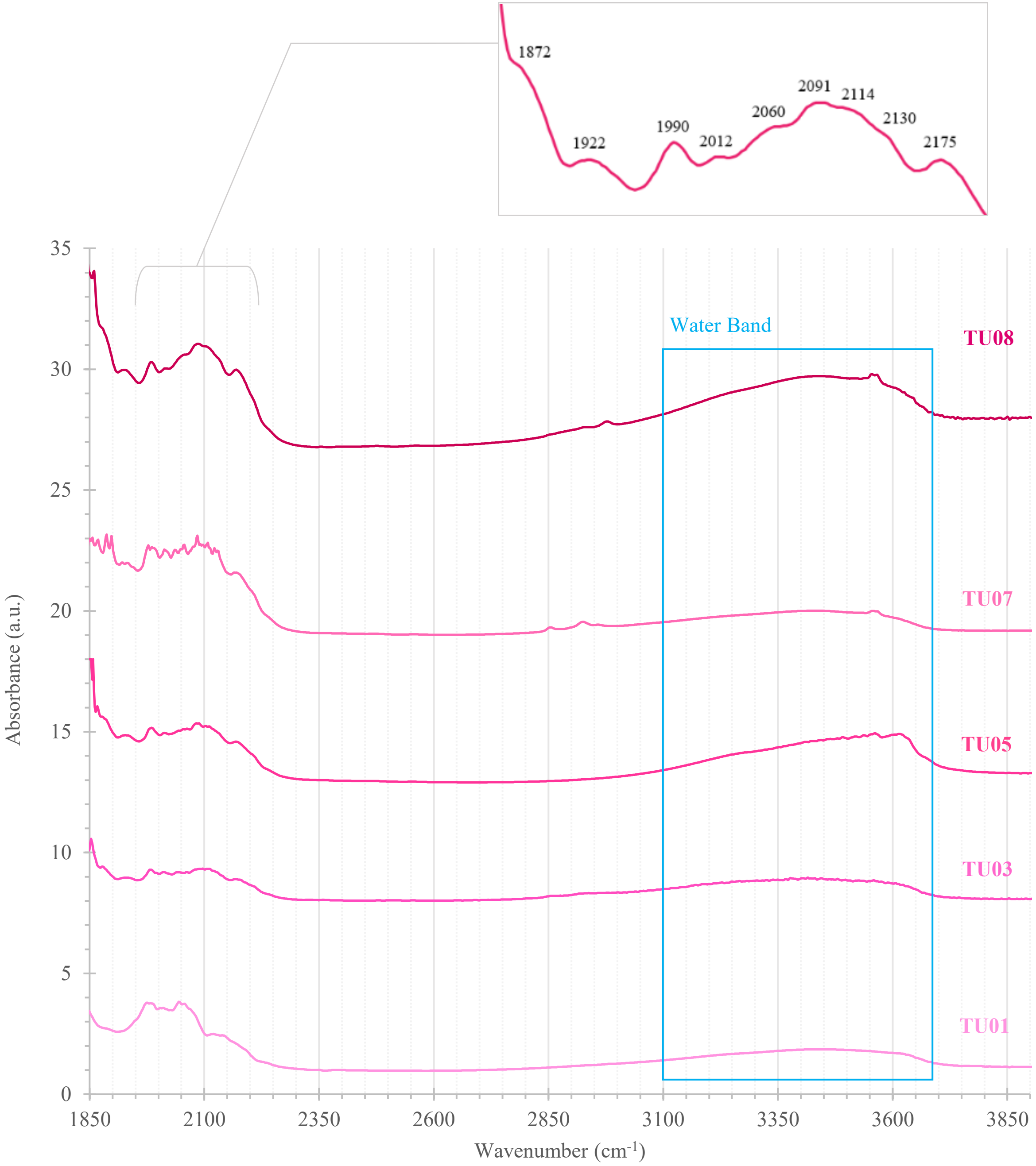

Figure 34: Infrared absorption spectra of few tugtupite samples. Spectra have been shifted for clarity.

For TU02, TU06, TU09, and TU10 in which FTIR transmission was not possible, reflectance spectra were recorded (*figure 35*). These spectra display several characteristic features. They were common to all of the samples; two first peaks at 474 and 534 cm^{-1}, followed by two weak bands at 619 and 659 cm^{-1} were observed, then, others well-defined peaks at 746, 797 and 1028 cm^{-1}, followed by weaker features at 1062 and 1110 cm^{-1}. Finally, a small band around 1200 cm^{-1} was detected.

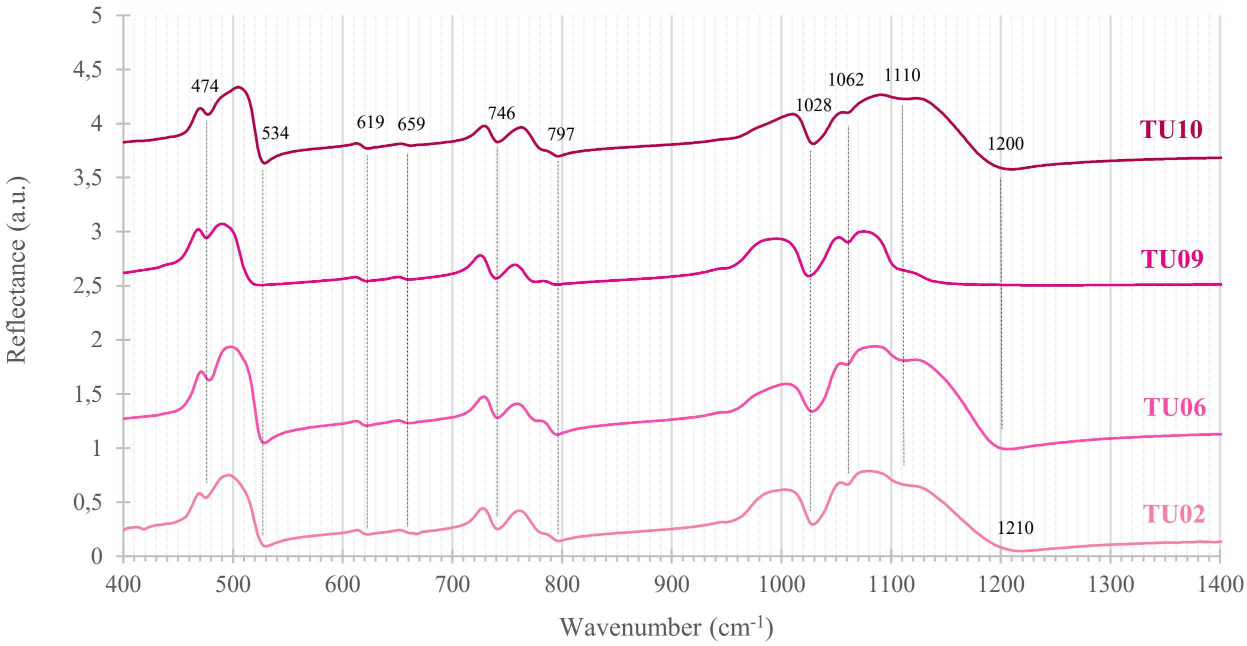

Figure 35: Infrared reflectance spectra of few tugtupite samples. Spectra have been shifted for clarity.

UV-Visible Spectroscopy

Representative UV-Visible spectra of the TU01 and TU03 specimens are shown in *figure 38*.

The spectrum of TU03 in its stable state — corresponding to the light pink color — displayed a broad absorption band between 440 and 600 nm, with a maximum at 507 nm. In the photogenerated intense pink state, the same absorption band was slightly shifted and enhanced, peaking at 509 nm. An additional minor band was observed in both states at approximately 370 nm. For TU01, a similar absorption band was visible between 440 and 600 nm. In the stable state, this broad band was almost negligible, while in the excited state it became more pronounced, peaking at 511 nm. An additional band peaking at 375 nm appeared. In both samples, the intensity of the small absorption band was higher in the excited state than in the stable state.

Analysis of the difference spectra shown in *figure 38* (*gray curve*) suggested the presence of two Gaussian components for both TU01 and TU03, corresponding to the distinct color centers reported in the literature (*Blumentritt & Fritsch, 2021*).

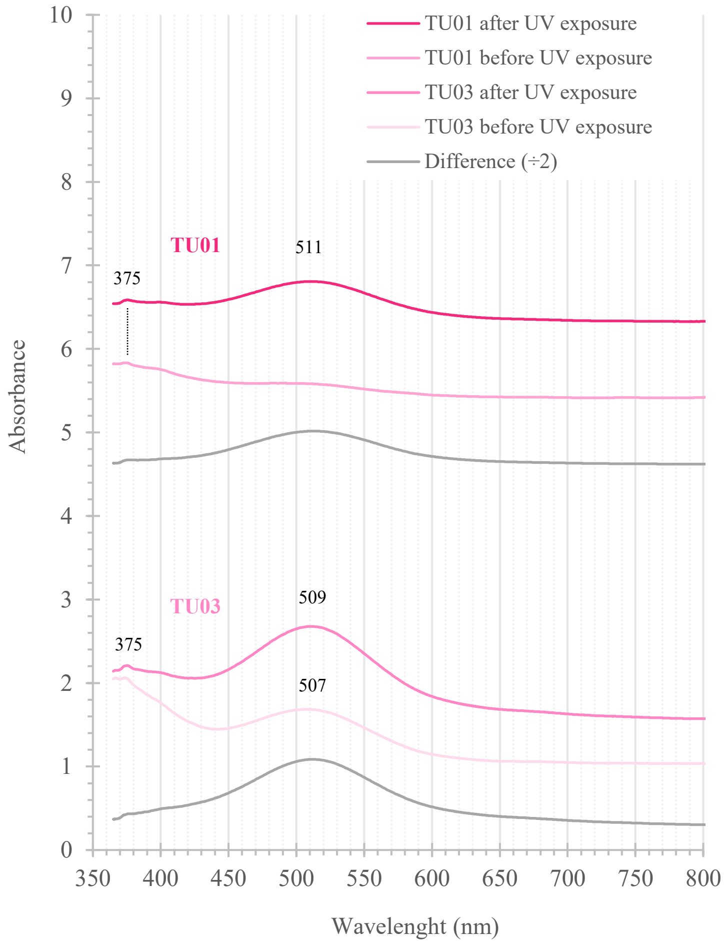

Figure 38: Example of UV-Visible spectra of TU01 and TU03 before UV exposure (light pink curve), after UV exposure (darker pink curve) and the difference divided by 2 (gray curve). Spectra have been shifted for clarity. Photographs of TU01 and TU03 have been taken by Claire Chapuis.

Figure 36: TU01 before and after exposure to short-wave UV. Photographs by Claire Chapuis.

Figure 37: TU03 before and after exposure to short-wave UV. Photographs by Claire Chapuis.

Photographs of TU01 and TU03 (*figures 36 and 37*) illustrate the change of color value before (pink) and after (pinkish-red) UV exposure, which was clearly observable. These results are consistent with the UV-Visible spectral observations reported by *Povarennykh et al.* (1971) and *Blumentritt & Fritsch* (2021).

Fourier-Transform Raman

Fourier-transform Raman spectra were acquired for all Greenland samples, from TU01 to TU10. The spectra of TU01, TU04, TU05, TU06, TU08, and TU09 are presented in the annexes (*see Annex I*). For the remaining samples, FT-Raman spectra are shown in *figure 39*, in comparison with the reference Raman spectrum of tugtupite from the RRUFF database (*figure 39, gray spectrum*).

Several bands were observed between 150 and 650 cm^{-1}, with particularly intense peaks at 462, 554, and 630 cm^{-1}. Two additional strong peaks were present at 1052 and 1129 cm^{-1}.

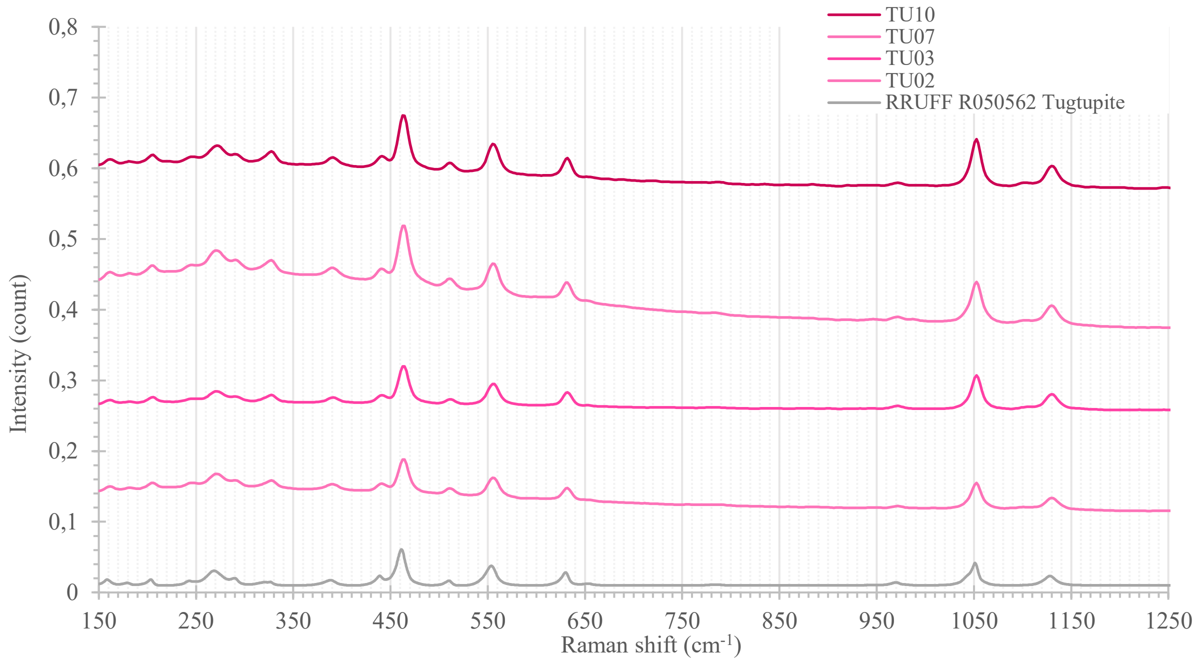

Figure 39: Fourier-Transform Raman spectra of TU02, TU03, TU07 and TU10 compared to tugtupite R050562 (gray) Raman spectrum from RRUFF database. Spectra have been shifted for clarity.

Figure 40 illustrates the FT-Raman spectrum of TU10, which exhibited all the characteristic features of a typical tugtupite Raman pattern. The spectrum showed multiple well-defined peaks between 50 and 1200 cm^{-1}. These included triplets at 113, 124, and 136 cm^{-1}, followed by another peak at 159, 186, and 204 cm^{-1}, and a third at 254, 269, and 286 cm^{-1}. Additional bands were observed at 327 and 393 cm^{-1}, along with a doublet at 439 cm^{-1}, with a 462 cm^{-1} prominent peak. Three distinct peaks appeared at 508, 554, and 630 cm^{-1}, followed by a weak peak at 967 cm^{-1}, a strong peak at 1052 cm^{-1}, and a final doublet at 1110 and 1129 cm^{-1}.

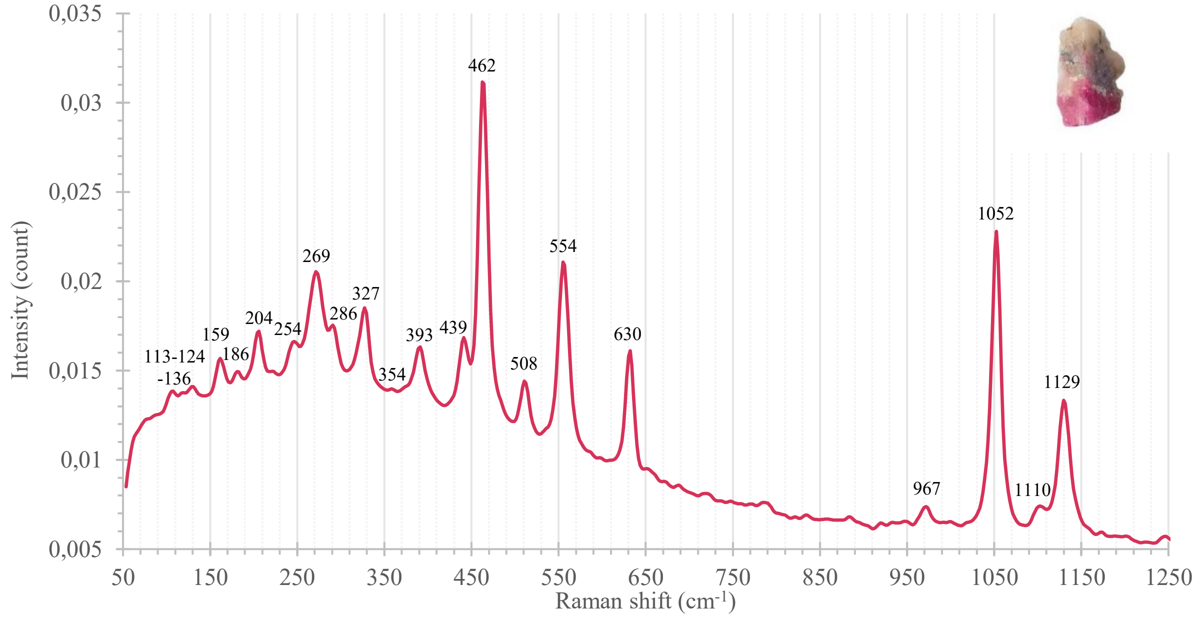

Figure 40: Close-up on TU10 Fourier-Transform Raman spectrum. Photograph of TU10 by Claire Chapuis.

Overall, the observed Raman features closely match the reference spectrum of tugtupite from the RRUFF database, confirming the identification of the samples.

Micro-Raman

As mentioned before, Micro-Raman spectra were acquired for all samples that could not be analyzed by FT-Raman due to their small crystal size, specifically for samples TU11 to TU16. The spectra of TU11, TU12, and TU14, shown in *figure 41*, are consistent with tugtupite, as confirmed by comparison with the reference Raman spectrum from the RRUFF database (*figure 41, gray spectrum*).

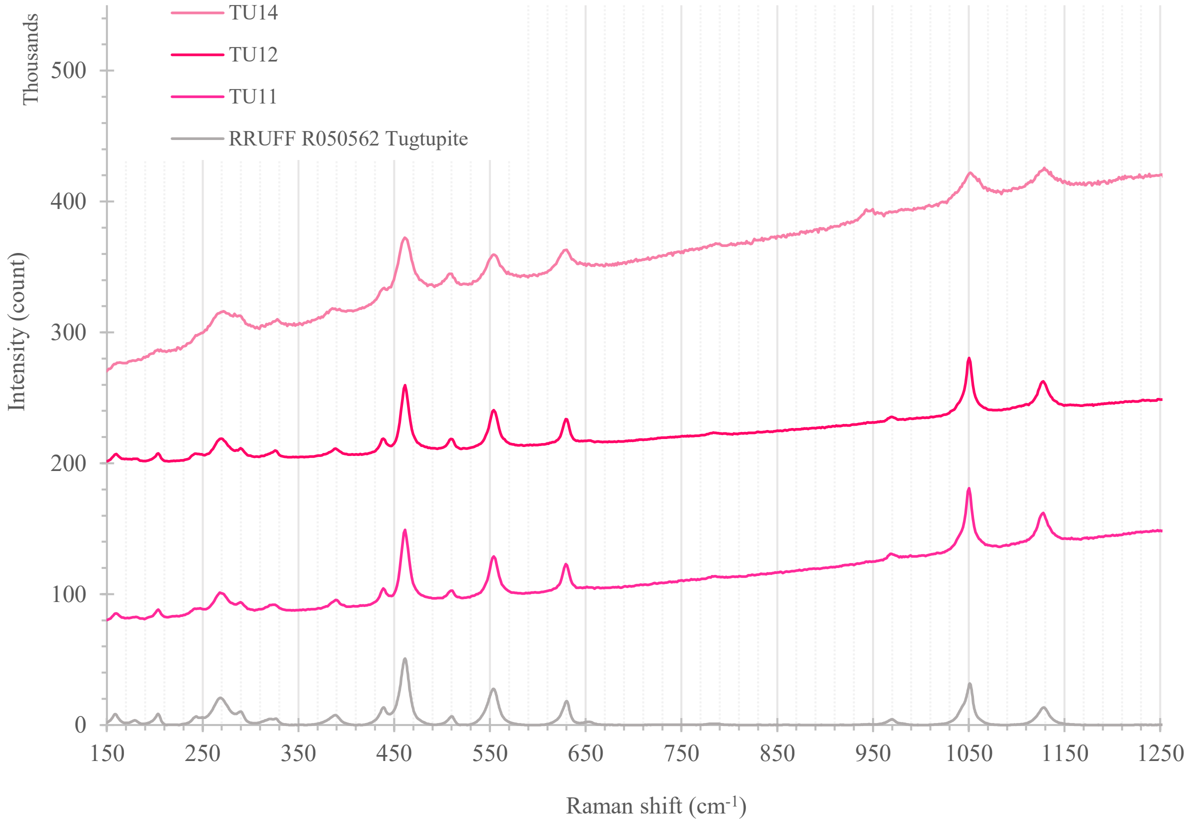

Figure 41: Micro-Raman spectra of TU11, TU12 and TU14 compared to tugtupite R050562 (gray) Raman spectrum from RRUFF database. Spectra have been shifted for clarity.

In contrast, Micro-Raman analyses of TU13, TU15, and TU16 indicate that these samples are not tugtupite, but rather associated minerals.

The pink crystal of TU13 was identified as a member of the eudialyte group. Comparison with RRUFF reference spectra of eudialyte (*figure 42, gray spectrum*) and manganoeudialyte (*figure 42, blue spectrum*) suggests a closer affinity with manganoeudialyte. However, the two peaks observed at 1124 and 1137 cm^{-1} were not consistent with any reference spectrum.

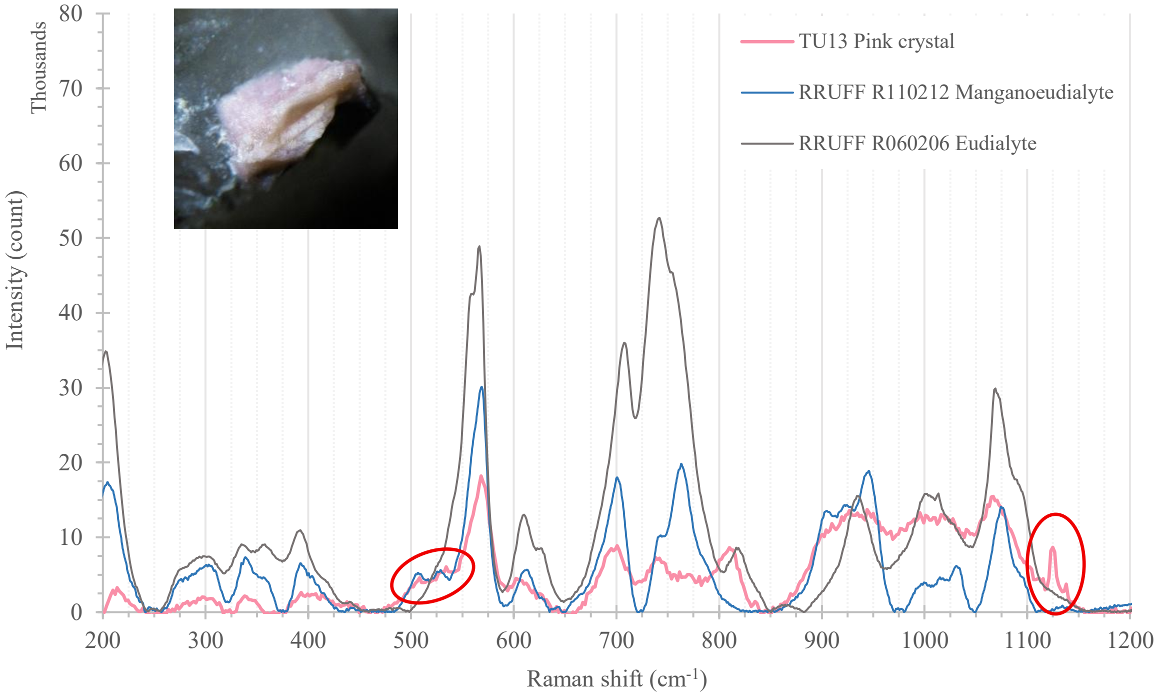

Figure 42: Micro-Raman spectrum of TU13 pink crystal (pink) compared to eudialyte R060206 (gray) and manganoeudialyte R110212 (blue) Raman spectra from RRUFF database. Photomicrograph of TU13 pink crystal by Claire Chapuis using a Nikon SMZ25 microscope, with a field of view of 14.67 mm.

Close-up micro-Raman spectrum of TU13 pink crystal (*figure 43*) shows the characteristic Raman peaks of eudialyte, along with the two unidentified peaks at 1124 and 1137 cm^{-1}.

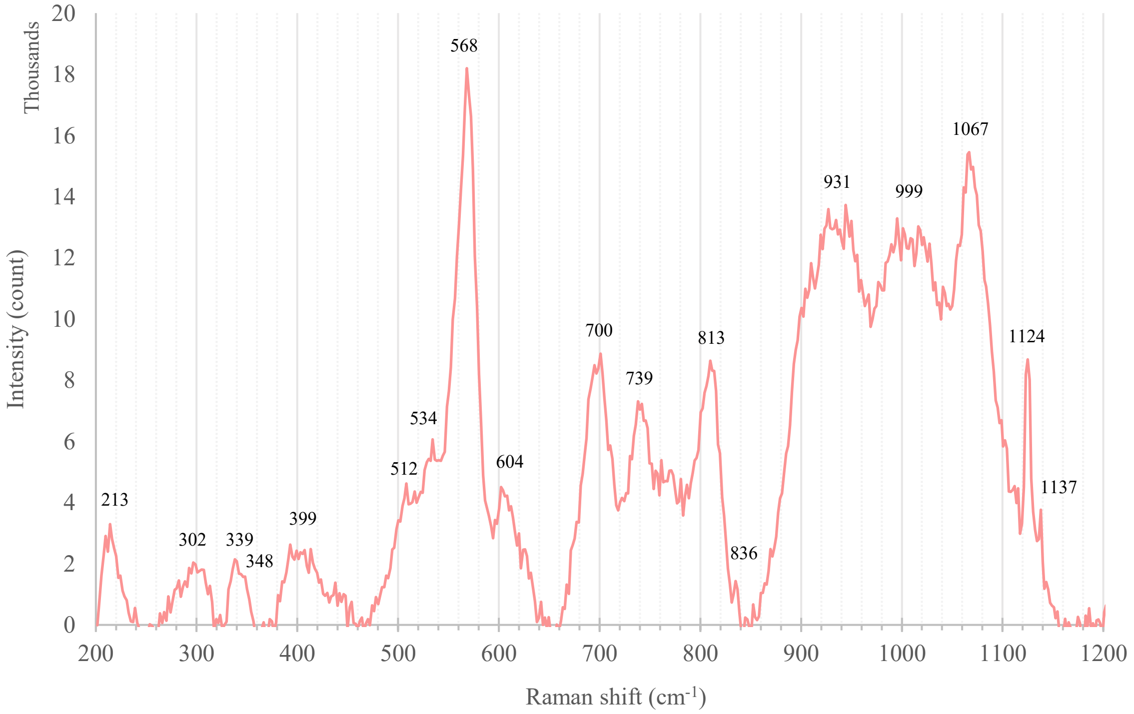

Figure 43: Close-up on TU13 pink crystal Micro-Raman spectrum. Background has been removed for clarity.

The red crystal of TU15 (*figure 44, red spectrum*) is consistent with the neptunite group, especially with manganoneptunite, as indicated by comparison with the RRUFF reference spectrum (*figure 44, gray spectrum*). An additional peak at 1058 cm^{-1} was present, which was not found in the neptunite reference (*figure 44, black spectrum*). Moreover, several bands present between 300 and 440 cm^{-1} in both reference spectra were not observed in the sample.

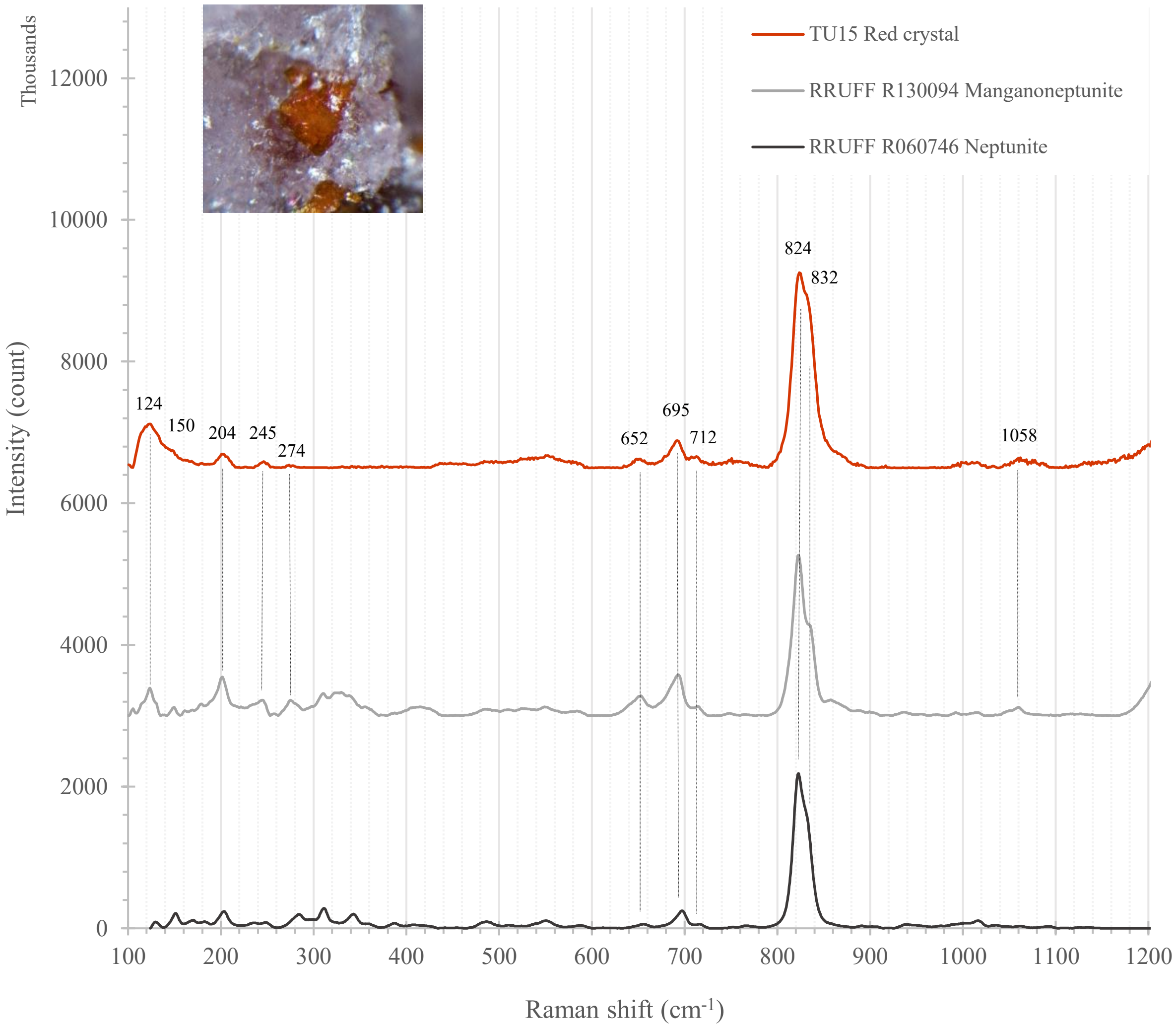

Figure 44: Micro-Raman spectrum of TU15 orangy red crystal (red) compared to manganoneptunite R130094 (blue) and neptunite R060746 (gray) from RRUFF database. Spectra have been shifted, modified and background of TU15 has been removed for clarity. Photomicrograph of TU15 red crystal by Claire Chapuis using a Nikon SMZ25 microscope, with a field of view of 2.62 mm.

TU15 close-up spectrum (*figure 45*) highlights the characteristic Raman peaks of the neptunite group. A nearly negligible broad band is observed between 360 and 460 cm^{-1}, which may correspond to features present in both the neptunite and manganoneptunite reference spectra seen in *figure 44*, that had not been observed previously.

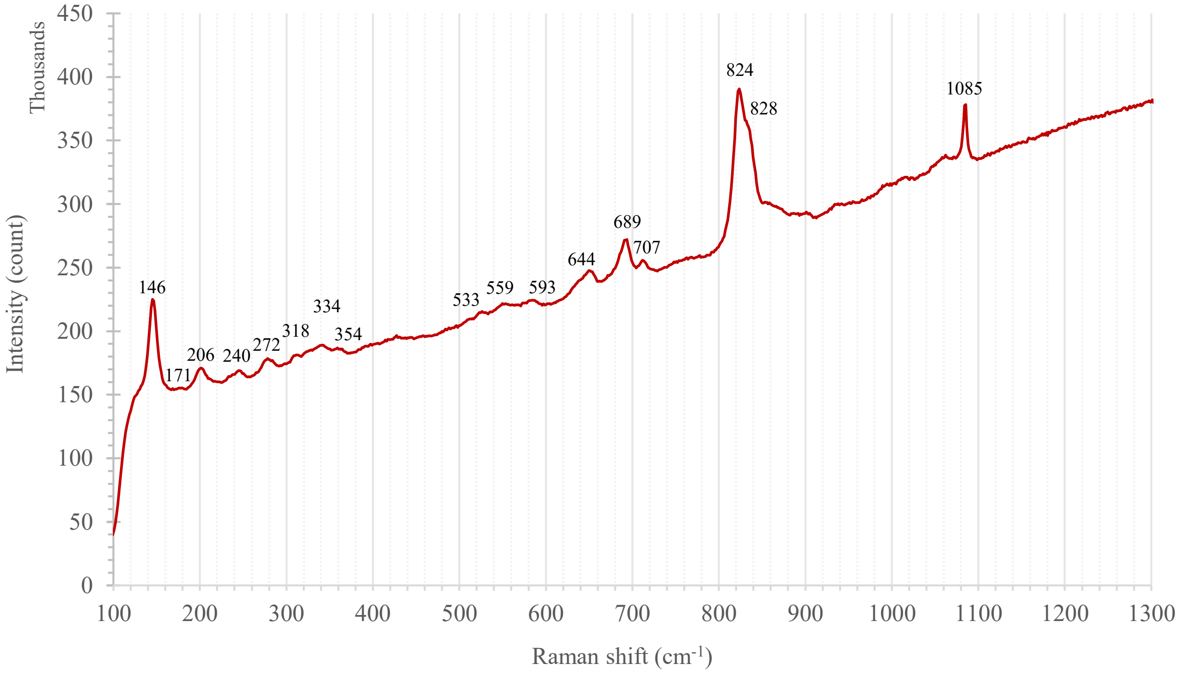

Figure 45: Close-up on TU15 pinkish red crystal Micro-Raman spectrum.

The violet crystal of TU16 (*figure 46, violet spectrum*) was identified as sodalite by micro-Raman spectroscopy (*figure 46, gray spectrum*). Based on its color, and photochromic behavior seen in *table IV*, this mineral was further attributed to the photochromic variety of sodalite, called "hackmanite."

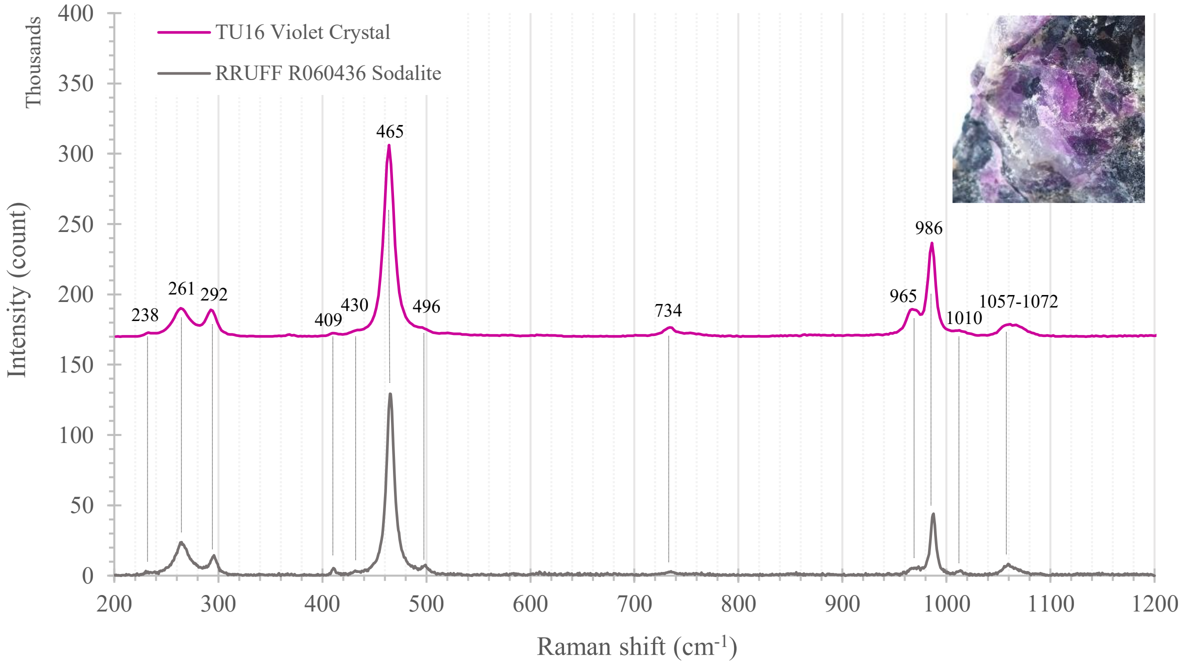

Figure 46: Micro-Raman spectrum of TU16 violet crystal (violet) compared to sodalite R060436 (gray) Raman spectrum from RRUFF database. Photograph of TU16 violet crystal by Claire Chapuis using an Olympus OM-D E-M10 Mark III camera fitted with a 42 mm f/5.6 II R lens.

EDX-SEM

Semi-quantitative Energy Dispersive Spectroscopy (EDS) analyses using the Backscattered Electron (BSE) detector on a Scanning Electron Microscope (SEM) were performed on selected Greenland samples (TU01 to TU06 and TU08) to determine their chemical composition. Metal and oxides types results are presented in *table V and table VI*, respectively.

Due to the limitations of quantitative EDS analysis, light elements such as beryllium, an important component of tugtupite, cannot be reliably detected, as its atomic number (Z = 4) is below the detection limit (Z = 11) (*myscope.training/EDS_Limitations_of_quantitative_analysis, consulted 16/10/2025*). Therefore, the analyses were normalized to obtain totals of 100%. This explains the differences observed between the reference values and the obtained results in both tables.

The results of metal type summarized in *table V*, are compared with reference data from *Mindat* (2025).

Table V: Chemical analyses of tugtupite samples, metal type.

% element mass	*Reference: mindat.org/min-4044.html*	*TU01*	*TU02*	*TU03*	*TU04*	*TU05*	*TU06*	*TU08*
O	**41.047**	36.52	43.2	38.23	42.7	42	44,4	34.91
Uncertainty		0.12	0.1	0.12	0.2	0.2	0.2	0.12
Difference (%)		*11.02%*	*5.24%*	*6.86%*	*4.02%*	*2.32%*	*8.16%*	*14.95%*
Na	**19.66**	21.22	18.57	20.72	18.9	19.9	19.6	20.55
Uncertainty		0.07	0.04	0.07	0.1	0.1	0.1	0.08
Difference (%)		*7.93%*	*5.54%*	*5.39%*	*3.86%*	*1.22%*	*0.3%*	*4.52%*
Al	**5.769**	6.54	5.98	6.34	5.9	5.9	5.8	6.8
Uncertainty		0.04	0.02	0.04	0.1	0.1	0.1	0.05
Difference (%)		*13.36%*	*3.65%*	*9.89%*	*2.27%*	*2.27%*	*0.53%*	*17.87%*
Si	**24.018**	27.07	24.35	26.3	24.3	24.3	23.1	28.35
Uncertainty		0.09	0.05	0.09	0.1	0.1	0.1	0.09
Difference (%)		*12.70%*	*1.38%*	*9.50%*	*1.17%*	*1.17%*	*3.82%*	*18.03%*
Cl	**7.58**	8.65	7.86	8.4	8	8	7.2	9.39
Uncertainty		0.05	0.03	0.05	0.1	0.1	0.1	0.06
Difference (%)		*14.11%*	*3.69%*	*10.81%*	*5.54%*	*5.54%*	*5.01%*	*23.87%*
Be	**1.927**	non-detectable	non-detectable	non-detectable	non-detectable	non-detectable	non-detectable	non-detectable
Total	100	100	100	100	100	100	100	100

Table VI reports the chemical analyses of the samples as oxides, compared with the data reported by *Danø* (1966).

Table VI: Chemical analyses of tugtupite samples, oxide type.

% element mass	*Reference: (Danø, 1966)**	*TU01*	*TU02*	*TU03*	*TU04*	*TU05*	*TU06*	*TU08*
Na_2O	**25.52**	27.22	25.85	27.09	26.16	27.25	27.68	25.88
Uncertainty		0.1	0.06	0.1	0.07	0.07	0.08	0.1
Difference (%)		*6.66%*	*1.29%*	*6.15%*	*2.50%*	*6.77%*	*8.46%*	*1.41%*
Al_2O_3	**11.15**	11.47	11.73	11.45	11.54	11.32	11.7	11.61
Uncertainty		0.08	0.05	0.08	0.06	0.05	0.06	0.08
Difference (%)		*2.87%*	*5.20%*	*2.69%*	*3.49%*	*1.52%*	*4.93%*	*4.12%*
SiO_2	**51.58**	53.4	54.23	53.52	53.83	53.12	52.84	54.22
Uncertainty		0.17	0.11	0.17	0.13	0.13	0.14	0.18
Difference (%)		*3.52%*	*5.13%*	*3.76%*	*4.36%*	*2.98%*	*2.44%*	*5.11%*
Cl	**7.28**	7.91	8.19	7.95	8.34	8.24	7.74	8.3
Uncertainty		0.05	0.03	0.05	0.04	0.04	0.04	0.05
Difference (%)		*8.65%*	*12.5%*	*9.20%*	*14.56%*	*13.18%*	*6.31%*	*14.01%*
BeO	**5.40**	non-detectable	non-detectable	non-detectable	non-detectable	non-detectable	non-detectable	non-detectable
Total	100.93	100	100	100	100	100	100	100

*Without S, K_2O and MgO for a total of 0,65.

In both types of analyses, only minor differences in the elemental mass percentages were observed between the reference and the measured values. No sulfur was detected in any of the studied samples.

Overall, the chemical results obtained in this study are consistent with literature data on tugtupite and confirm the nature of the samples.

Semi-quantitative Energy-Dispersive X-ray Fluorescence

In contrast to EDX-SEM, Energy-Dispersive X-ray Fluorescence (EDXRF) analyses (*see Annex II*) reveal the presence of sulfur as well as other common and previously unreported impurities. Chemical analyses were conducted exclusively on Greenland samples due to crystal size limitations in Canadian and Russian tugtupite specimens. Beryllium and oxygen could not be reliably detected due to instrumental limitations. The data in the table *Annex II* are given as normalized concentrations (ppm) to show only the proportions of the analyzed elements.

The concentrations of the primary constituents are generally consistent across all samples, with minor variations attributed to associated minerals present in their matrix. Sample TU01 shows greater variability, particularly in aluminum content (24,900 ppm compared to a range of 67,370-80,030 ppm for TU02 to TU10), silicon content (459,690 ppm compared to 283,680-304,860 ppm), and chlorine content (138,810 ppm compared to 255,660-374,080 ppm).

All analyzed samples except TU09 contained sulfur. Sulfur concentrations corresponded to approximately 1.50-2.60% of the chlorine content, except for TU01, where sulfur represented about 6.89% of the chlorine content.

Compared to the observations reported by Danø (1966) which indicated that "S is about 5% of the Cl content", the values obtained here are roughly half as high, except for TU01. This difference may be explained by the detection of additional impurities in the present study, beyond the commonly reported elements in the literature: potassium (K), calcium (Ca), iron (F), gallium (Ga), and magnesium (Mg) (*Semenov & Bykova, 1960; Danø, 1966; Mindat, 2025)*. Indeed, additional impurities were detected, including manganese (Mn), strontium (Sr), barium (Ba), bromine (Br), iodine (I), cesium (Cs), chromium (Cr), nickel (Ni), vanadium (V), titanium (Ti), scandium (Sc), rubidium (Rb), copper (Cu), and zinc (Zn).

Finch et al. (2016) also reported the presence of scandium and titanium at concentrations of 10 ppm and 6 ppm, respectively. In the present study, scandium was detected only in sample TU08 at 3.7 ppm. Titanium, however, was present in all samples except TU08 (with 10.1 ppm, considered as below the detection limit), with concentrations ranging from 26 to 368.2 ppm.

Some elements occurred in relatively high concentrations. Zinc (Zn), for instance, reaches 848 ppm in TU01 and 2051 ppm in TU02, while remaining much lower in other samples such as TU05 (20.1 ppm), TU08 (20.31 ppm), and even less significant concentration in TU09 (5.33 ppm). Similarly, barium concentrations ranged between 338 and 530 ppm in TU02, TU08 Rough, TU09, and TU10, but reached 1910 ppm in TU01. Bromine was also present in significant amounts, with concentrations of 215.5 ppm in TU08 Rough, 187.9 ppm in TU10, 172.4 ppm in TU05, 149.9 ppm in TU08, 93.7 ppm in TU07, 71.54 ppm in TU01, and 73.1 ppm in TU09, while TU02 contained only 5.44 ppm Br.

Finally, an unusual presence of chromium was detected exclusively in TU07, at a concentration of 12.6 ppm. *Finch et al.* (2016) reported the presence of chromium in other aluminosilicates, particularly in sodalite, with concentrations ranging from 12 ppm (*turquoise sodalite, sample "F-12-21*) to 129 ppm (*pink sodalite, sample AF-07-35*), but it was not detected in their "*AF-99-173*" tugtupite sample.

Luminescence

Tugtupite luminescence is a well-documented mineral phenomenon in the literature. As previously observed in the classical gemological analyses, the tugtupite reacts distinctly under both short-wave (SWUV) and long-wave (LWUV) ultraviolet radiation, displaying an orangey-red luminescence under SWUV and an orange luminescence under LWUV. Observations also reveal that, for most samples, the intensity of luminescence is stronger under SWUV excitation.

Based on these visual observations, luminescence spectra were recorded using a spectrofluorimeter. Emission spectra were acquired in the 320-800 nm range under two excitation wavelengths: 254 nm (SWUV) and 365 nm (LWUV).

Luminescence spectra were recorded for samples TU01 to TU10. Under both excitation conditions, spectra displayed several emission peaks and broad bands, which were subsequently used to determine excitation spectra. Selected emissions obtained at 254 nm and 365 nm were then analyzed to identify their associated excitation bands (*table VIII*).

Table VII: Excitation wavelengths studied from TU01 to TU10.

Sample	*Excitation Wavelengths Studied (nm)*
TU01	440, 625, 676
TU02	647, 679, 689
TU03	428, 444, 677
TU04	649, 684
TU05	421, 673, 686, 693, 720
TU06	648, 676
TU07	427, 680
TU08	425, 648, 674, 685, 695
TU09	647, 681
TU10	673, 687

Figure 47 presents several representative emission spectra recorded at 254 nm. In these spectra, samples TU04, TU06 and TU08 all exhibited a broad emission band between 600 and 800 nm, peaking at 676 nm for TU06 and slightly shifted to 685 nm for TU04 and TU08. A weaker, broad band was also observed between 400 and 460 nm.

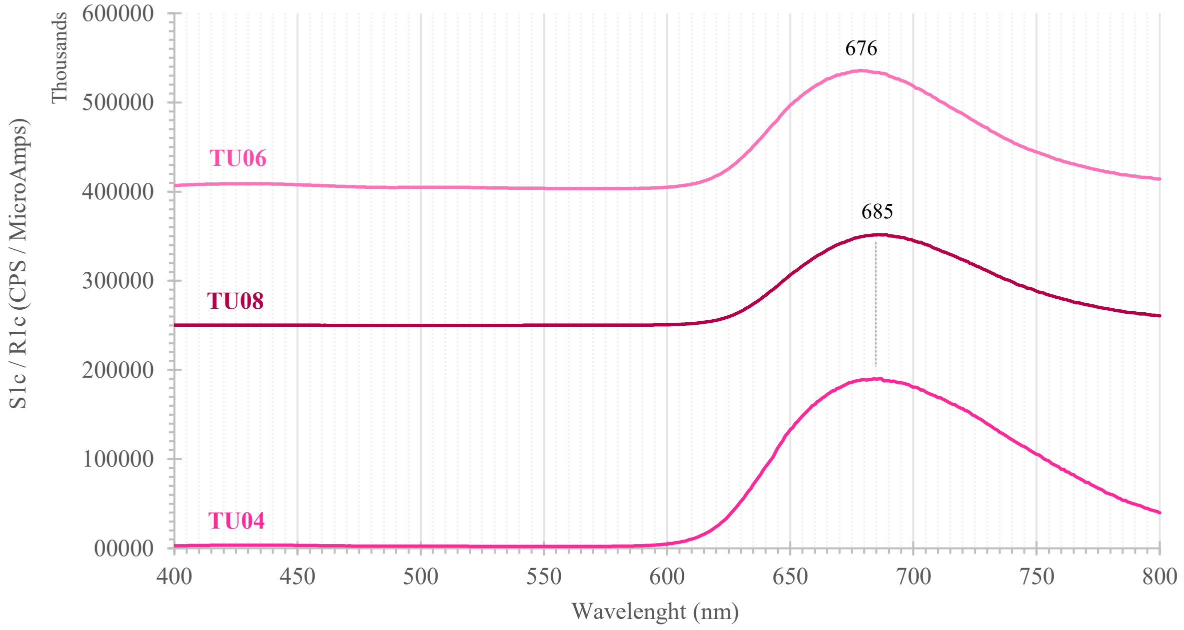

Figure 47: Emission spectra at 254 nm with a 5 nm slit of TU04, TU08 and TU06. Spectra have been shifted for clarity.

The excitation spectrum corresponding to the 685 nm emission of sample TU08 (*figure 48*), as shown in the 254 nm emission spectrum (*figure 47*), reveals two main excitation bands: a sharp band centered at 258 nm, attributed to the mineral's response to short-wave UV, and a broader band peaking around 388 nm. A weak peak was also observed at 375 nm.

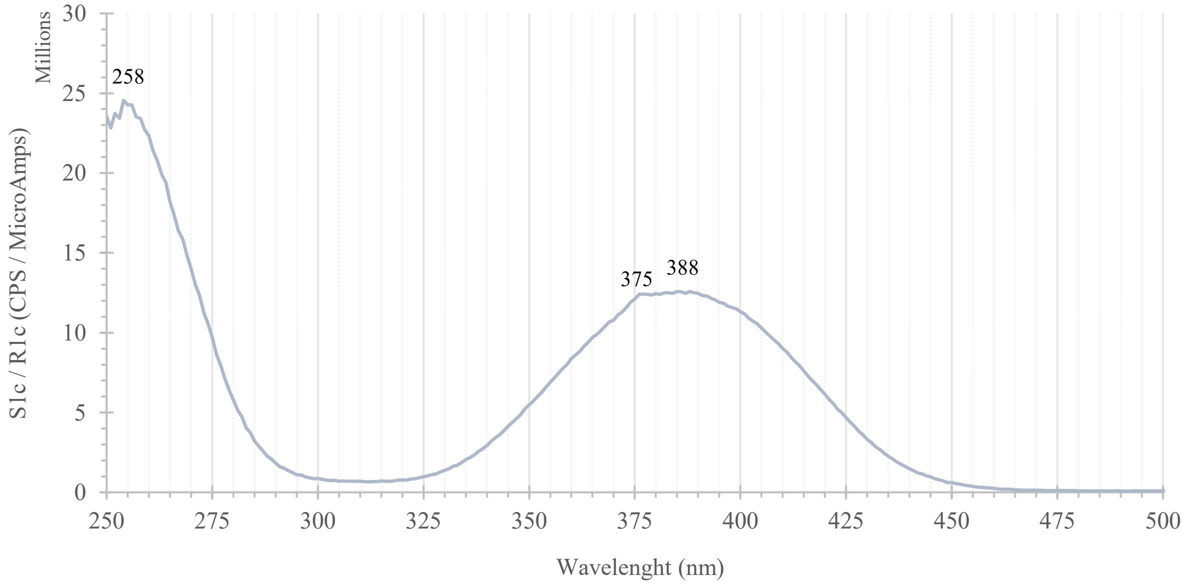

Figure 48: Example of TU08 excitation spectrum for an emission at 685 nm.

Under 365 nm excitation, the emission spectra of TU04, TU06 and TU08 (*figure 49*) displayed several bands between 550 and 800 nm, notably at 648, 674, and 695 nm. These quite regularly spaced peaks correspond to the vibrational structure of the S_2^- polyanion (*Povarennykh et al., 1971; Gaft et al., 2009*). Additionally, a broad band between 400 and 460 nm was observed, peaking around 425 nm in TU08 and 432 nm in TU04 and TU06.

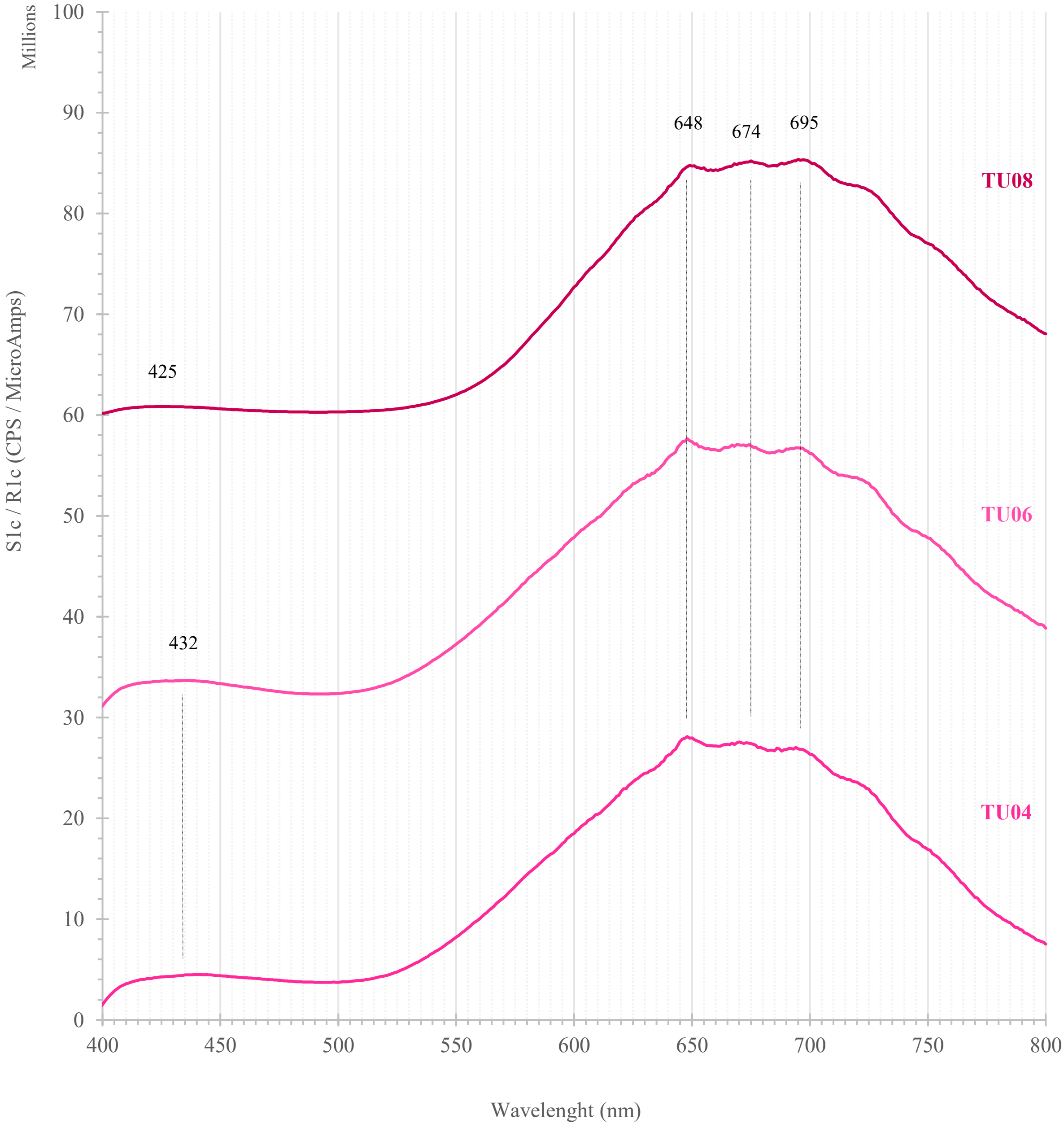

Figure 49: Emission spectra at 365 nm with a 5 nm slit of TU04, TU06 and TU08. Spectra have been shifted for clarity.

Focusing on sample TU08, the excitation spectrum corresponding to the 425 nm emission (*figure 50*), previously observed in the 365 nm emission spectrum (*figure 49*), showed a broad band between 250 and 350 nm, peaking at 306 nm.

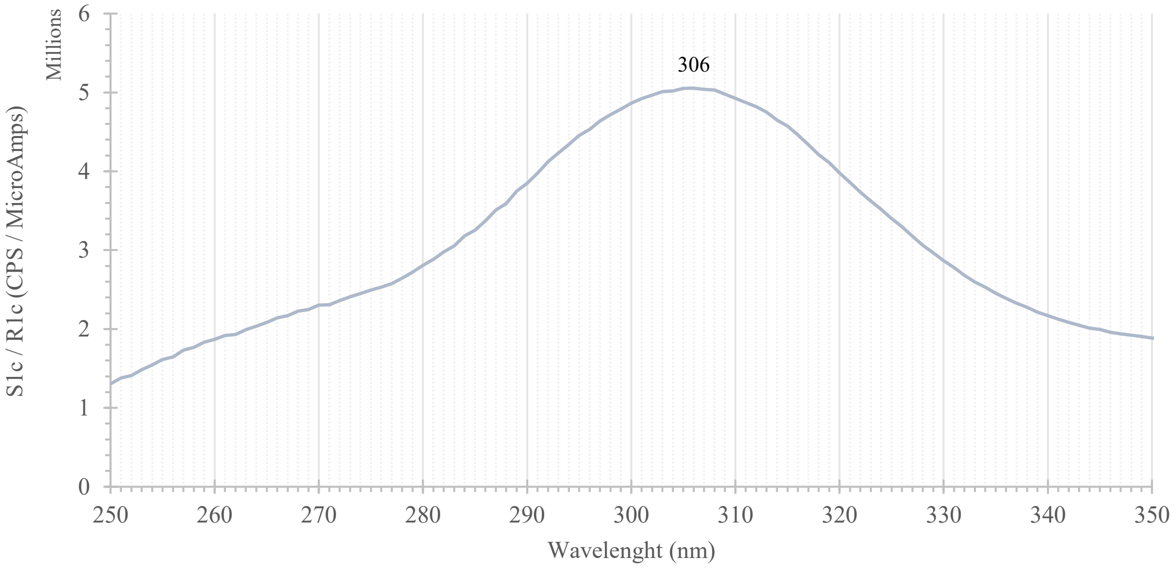

Figure 50: Example of TU08 excitation spectrum for an emission at 425 nm and a slit of 5 nm.

Furthermore, for the emission peaks observed in TU08 under 365 nm excitation (*figure 49*) at 648, 674, and 695 nm, the corresponding excitation spectra (*figure 51*) displayed two main bands: one centered around 258 nm, attributed to the response of tugtupite to short-wave UV, and a broader band peaking at 388 nm. A weak peak was also observed at 378 nm, mainly for the 674 nm emission. The similarity of these excitation spectra indicates that the three emissions (648, 674, and 695 nm) originate from the same luminescence center.

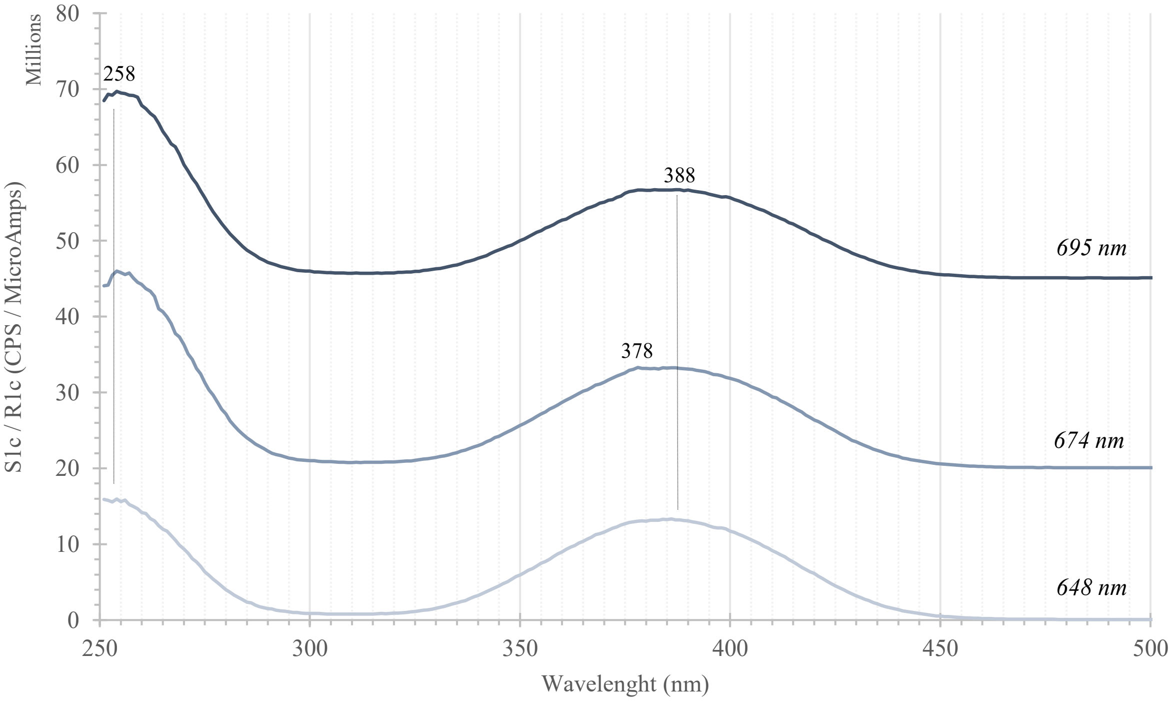

Figure 51: Example of TU08 excitation spectra for emissions at 648, 674 and 695 nm and a slit of 2 nm. Spectra have been shifted for clarity.

Table IX presents all emission wavelengths studied for samples TU01 to TU10, along with their corresponding maximum excitation bands. Overall, the results indicate that all samples exhibit similar excitation features under both short-wave (254 nm) and long-wave (365 nm) ultraviolet excitation.

Table VIII: Results of the excitation wavelengths studied from TU01 to TU10.

Sample	*Emission Wavelengths (nm)*		*Maximum Excitation Bands (nm)*
	At 254 nm (SWUV)	*At 365 nm (LWUV)*	
TU01	440		306
		625	388
	676*	**676***	388
TU02		647	388
	679		388
	689*	**689***	388
TU03	428		306
	444		306
	677*	**677***	388
TU04		649	388
	684		388
TU05	**421***	**421***	306
		673	388
	686		388
		693	388
		720	388
TU06		648	398
	676*	**676***	398
TU07		427	300
	680		388
TU08		425	306
		648	388
		674	388
	685		388
		695	388
TU09		647	398
	681		398
TU10		673	388
	687		388

*Bold numbers are common to both emissions.

From the results summarized in *table IX*, three main excitation bands can be identified at approximately 300-306 nm, 388 nm, and 398 nm. Under LWUV excitation (365 nm), the characteristic vibrational structure of S_2^- is clearly visible, producing multiple bands between 550 and 800 nm (*Povarennykh et al., 1971; Gaft et al., 2009*).

Phosphorescence

Under 254 nm UV excitation, samples TU05, TU07, and TU08 exhibited phosphorescence spectra (*figure 52*).

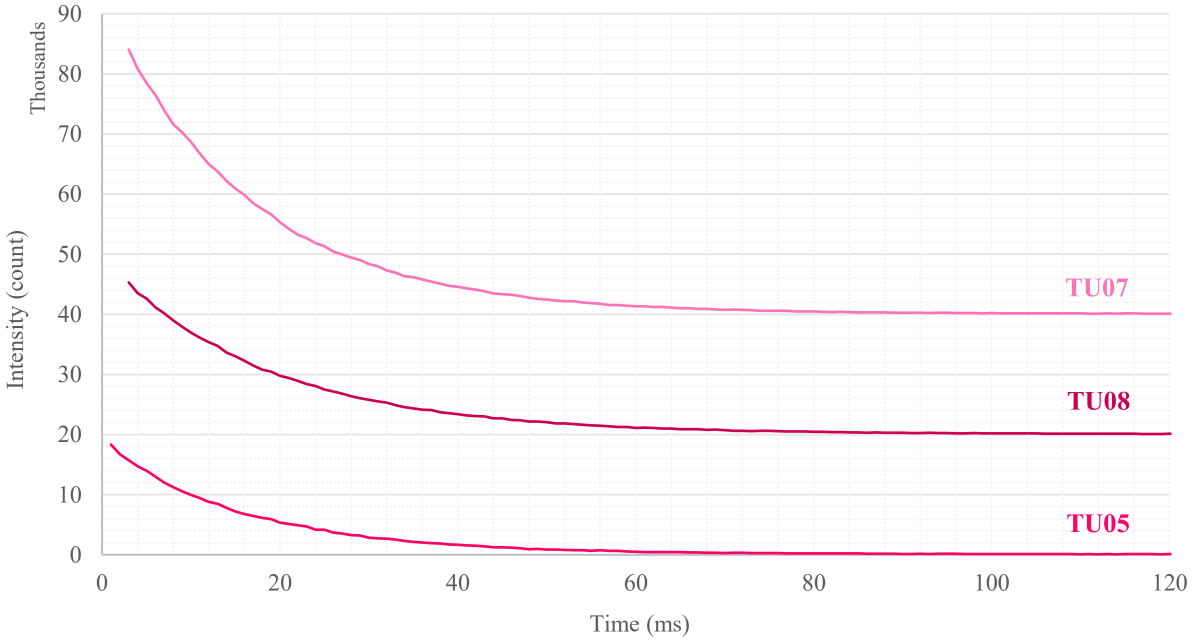

Figure 52: Phosphorescence spectra of TU05, TU07 and TU08 with 254 nm emission. Spectra have been shifted for clarity.

The emission intensity decreased sharply within the first few milliseconds after excitation, becoming faint at approximately 30 ms and barely detectable at 40 ms. Among the three samples, TU07 displayed the highest initial intensity, whereas TU05 showed the weakest.

This behavior indicates that the phosphorescence of tugtupite is extremely short-lived and generally not observable to the unaided eye, consistent with the observations reported by *Gao & Sun* (2023).

Associated Minerals

This second part of this study focuses on the minerals found alongside the tugtupite matrix. These minerals are evidence of the geological environment in which tugtupite formed and can help understand its formation. The aim of these analyses was to determine the differences between samples from different geographic origins.

Laboratory Gemology

Micro-Raman

All analyses of the associated minerals were performed using a micro-Raman spectrometer to identify each inclusion/phase observed in the samples. Samples from three geographic localities were tested: four Greenland tugtupites (TU01, TU05, TU07, and TU08), the three Canadian samples (TU11, TU12, and TU13), and two Russian samples (TU14 and TU15).

- **Greenland samples**

For sample TU01, *figure 54* presented the Raman spectra of three mineral inclusions associated with tugtupite, compared with reference spectra from the RRUFF database. The identified minerals are chkalovite (gray massive inclusion), neptunite (elongated black crystal), and albite (translucent to grayish-white crystal aggregate). The corresponding microphotographs of the analyzed area are shown in *figure 53*.

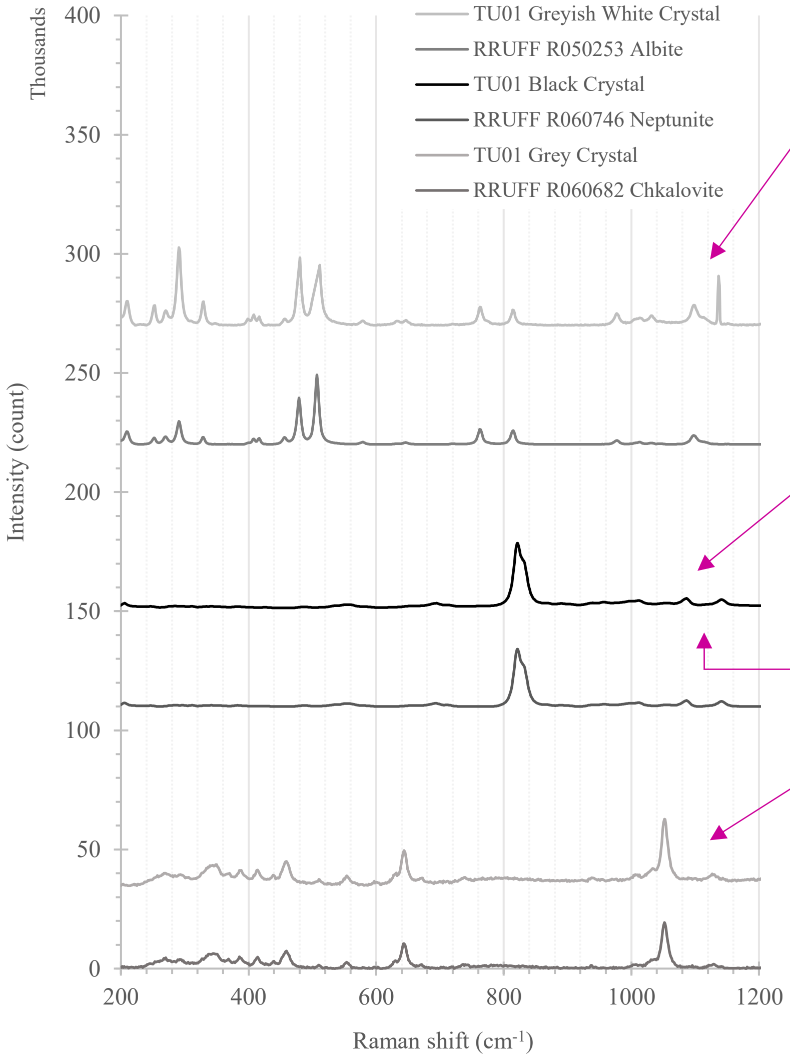

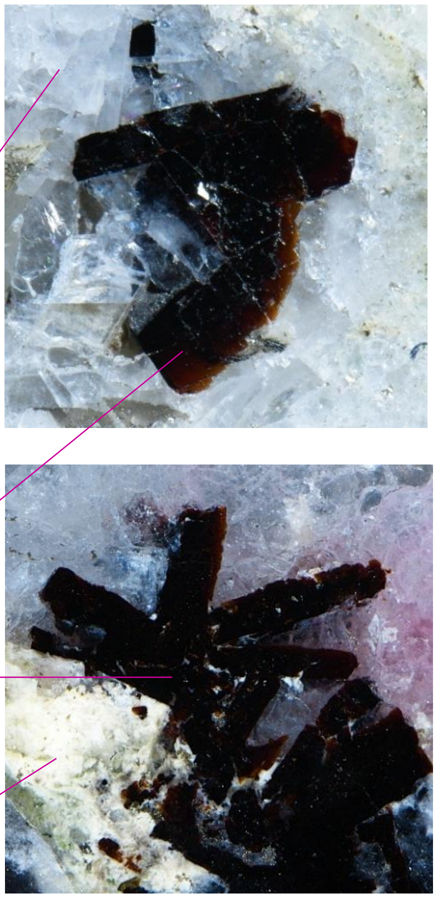

Figure 53: Photomicrographs of TU01 inclusions acquired by Claire Chapuis using a Nikon SMZ25 microscope. The field of view is 14.7 mm (top) and 11 mm (bottom).

Figure 54: Micro-Raman spectra of TU01 associated minerals compared to Raman spectra of reference minerals from the RRUFF database. Spectra have been modified and shifted for clarity.

In sample TU05, *figure 56* displayed the Raman spectra of two additional minerals found in association with tugtupite: arfvedsonite (black crystal) and albite (grayish-white crystal), again matched with RRUFF mineral reference spectra. The corresponding photomicrographs are presented in *figure 55*.

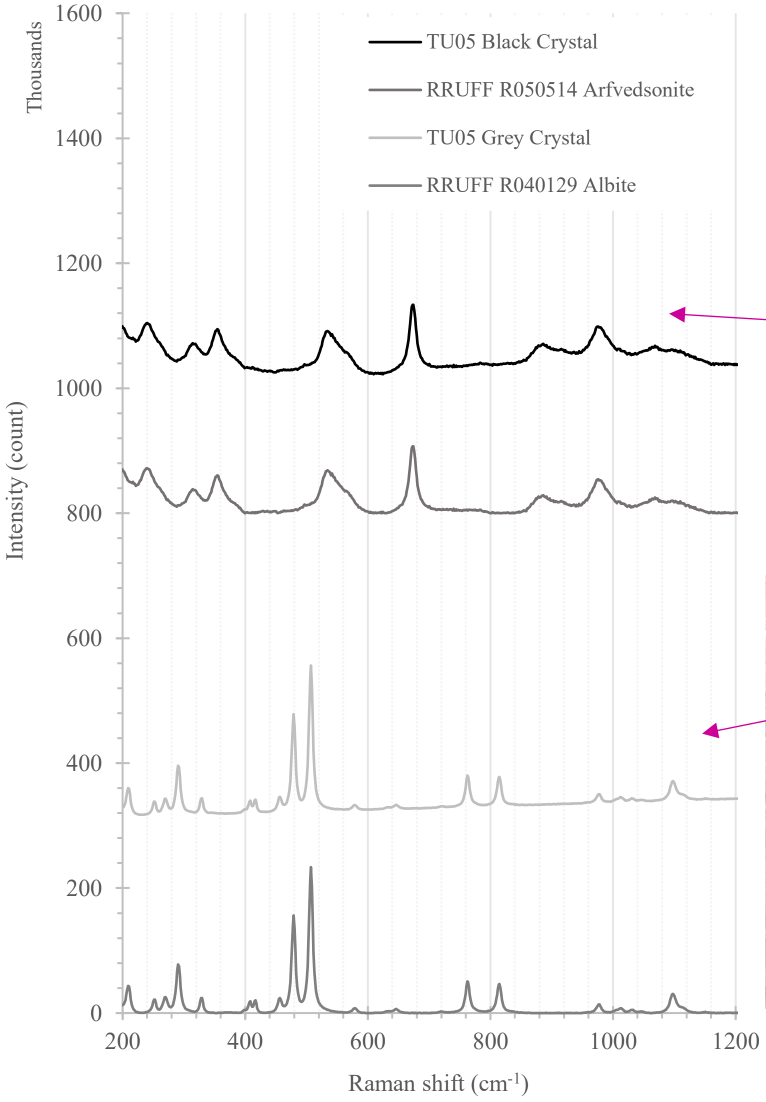

Figure 56: Micro-Raman spectra of TU05 associated minerals compared to Raman spectra of reference minerals from the RRUFF database. Spectra have been modified and shifted for clarity.

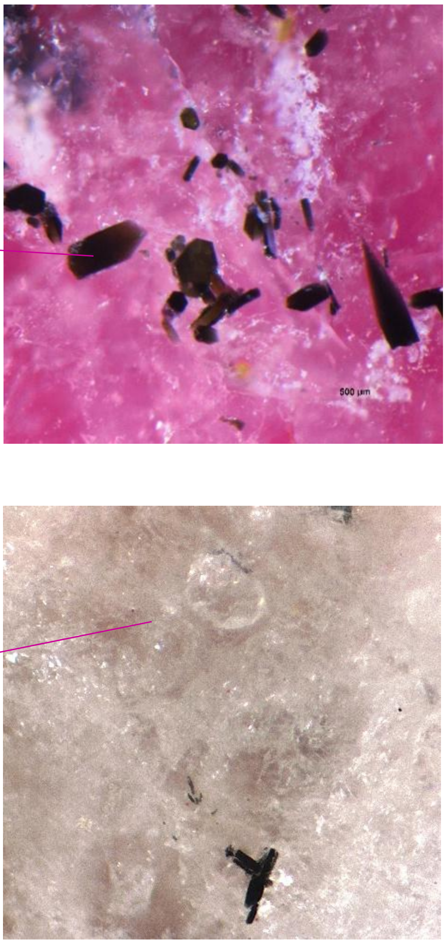

Figure 55: Photomicrographs of TU05 inclusions by Claire Chapuis using a Nikon SMZ25 microscope. Field of view: 4.40 mm.

As for sample TU07, *figure 58* shows the spectra of two additional minerals associated with tugtupite — chkalovite (gray inclusion) and neptunite (black crystal) — both consistent with the minerals previously identified in TU01. The related microphotograph is displayed in *figure 57*.

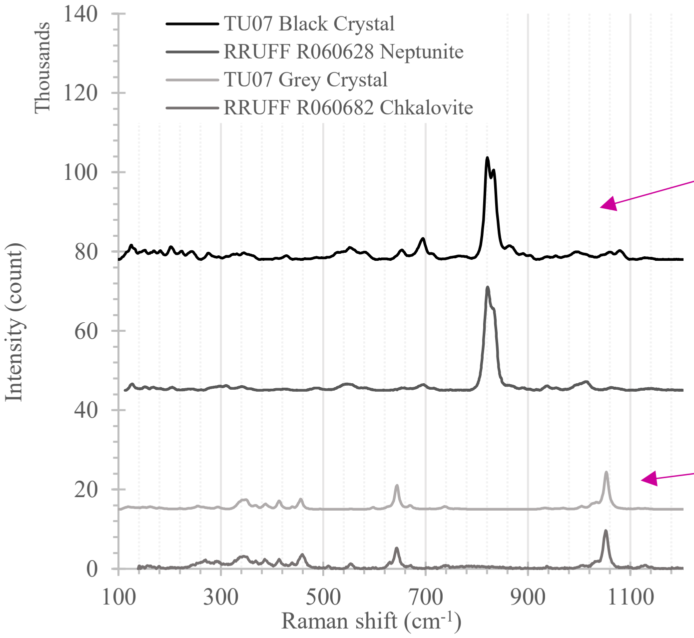

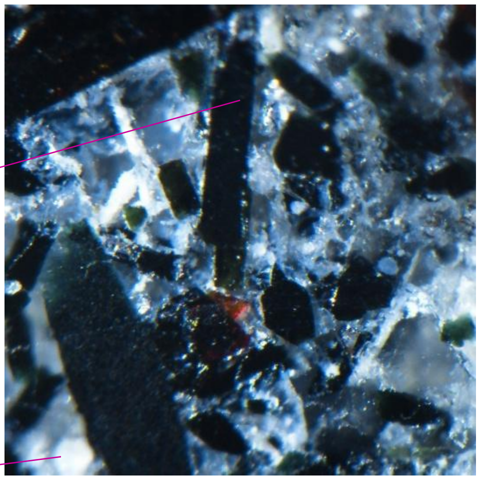

Figure 57: Photomicrograph of TU07 inclusions by Claire Chapuis using a Nikon SMZ25 microscope. Field of view: 2.44 mm.

Figure 58: Micro-Raman spectra of TU07 associated minerals compared to Raman spectra of reference minerals from the RRUFF database. Spectra have been modified and shifted for clarity.

In sample TU08, the associated mineral detected by micro-Raman spectroscopy (*figure 59*, *light gray spectrum*) showed a strong correspondence with pyrochlore, based on the comparison with the RRUFF pyrochlore reference spectrum (*figure 59*, *gray spectrum*). This identification suggests the presence of a pyrochlore-group mineral, occasionally observed in late-stage pegmatitic assemblages within the Ilímaussaq complex.

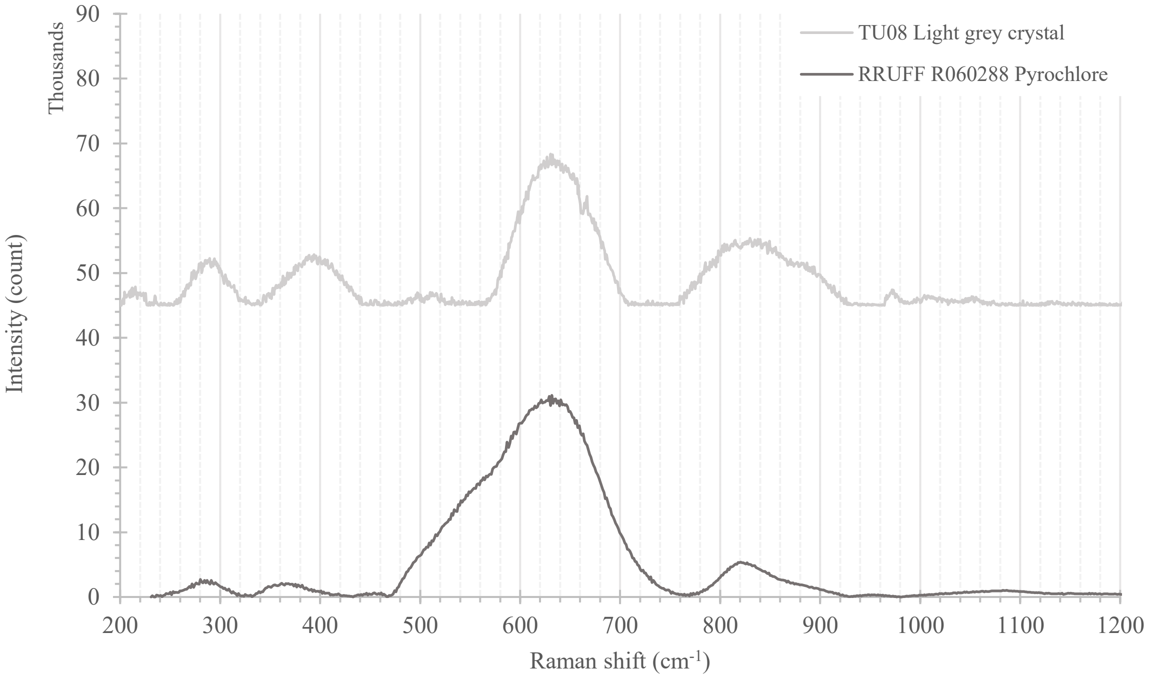

Figure 59: Micro-Raman spectrum of TU08 associated mineral compared to pyrochlore Raman spectrum from the RRUFF database. Spectra have been modified and shifted for clarity.

- **Canadian samples**

For sample TU11, several minerals were identified through comparison with RRUFF reference spectra. The white crystalline phase observed (*figure 60, (a)*) showed spectral features compatible with both ussingite and chesnokovite. Another phase was identified as sodalite (*figure 60, (b)*).

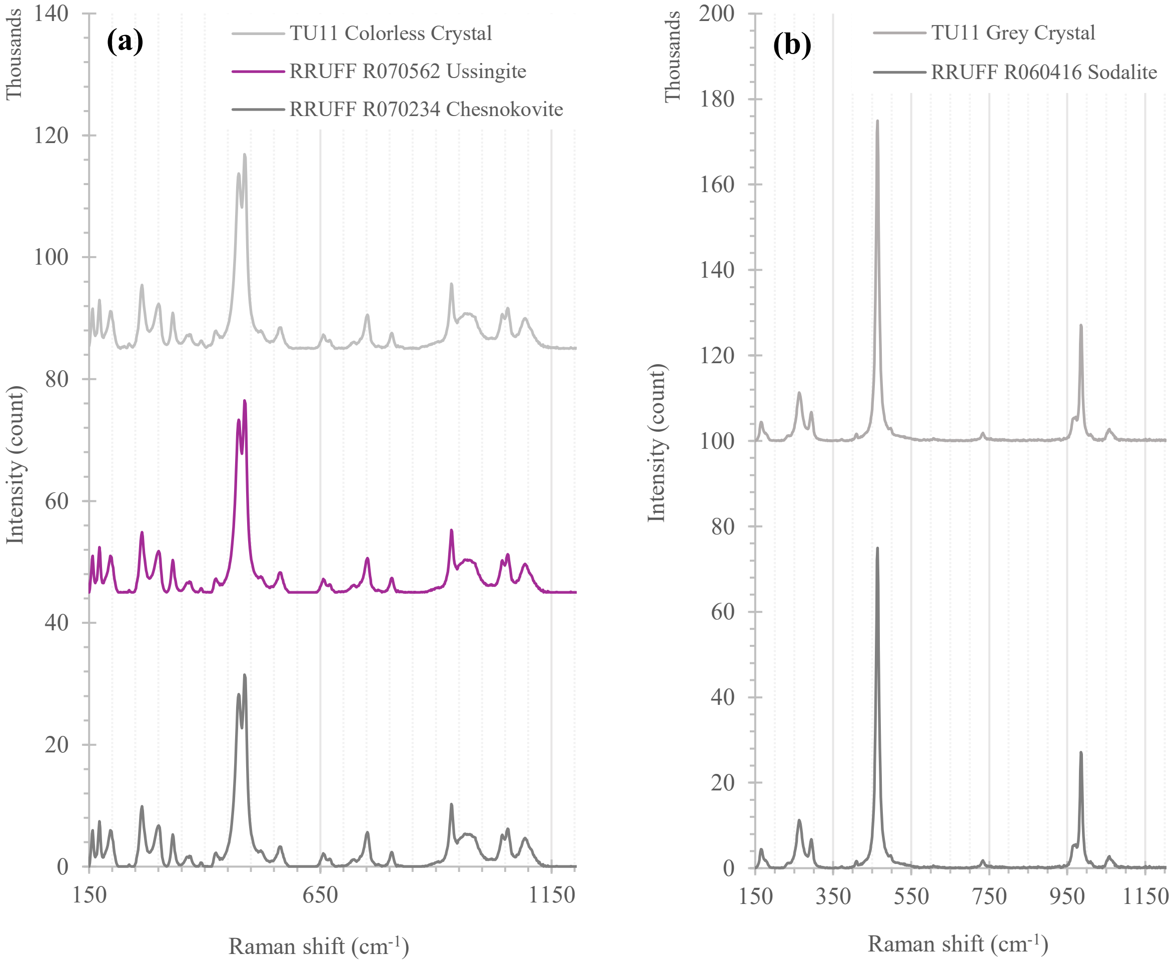

Figure 60: Micro-Raman spectra of TU11 associated minerals compared to Raman spectra of reference minerals from the RRUFF database. Spectra have been modified and shifted for clarity.

When comparing the TU11 pink crystal photomicrograph (*figure 61*) with that of aegirine crystals enclosed in colorless ussingite from Mont Saint-Hilaire (*figure 62*), a similar textural relationship was observed. In TU11, an aegirine crystal was observed within a colorless mineral aggregate near the tugtupite grain (*red circle in figure 61)*. Considering the geological context, the known association between ussingite and tugtupite (*Yakovlevskaya & Semenov, 1963; Sørensen et al., 1971*), and the lack of evidence for chesnokovite outside Russia (*Mindat, 2025*), it is reasonable to attribute the colorless phase in TU11 to ussingite rather than chesnokovite.

Figure 61: TU11 tugtupite crystal associated with presumed ussingite, sodalite and aegirine from Mont Saint-Hilaire, Canada. Field of view: 8.15 mm. Photomicrograph by Claire Chapuis taken with a Nikon SMZ25 microscope.

Figure 62: Group of colorless ussingite crystals with aegirine from Poudrette quarry, Mont Saint-Hilaire, La Vallée-du-Richelieu RCM, Montérégie, Québec, Canada. Field of view: 1.2 mm. Photomicrograph by Douglas Merson, obtained from László Horváth. (*https://www.mindat.org/photo-31960.html,2025*).

In sample TU12, Raman analyses revealed the presence of aegirine (greenish-black crystal) and sodalite (gray crystal), as confirmed by RRUFF spectra (*figure 63, (a)*). The same uncertain white mineral, showing spectral similarity to both ussingite and chesnokovite, was again detected (*figure 63, (b)*).

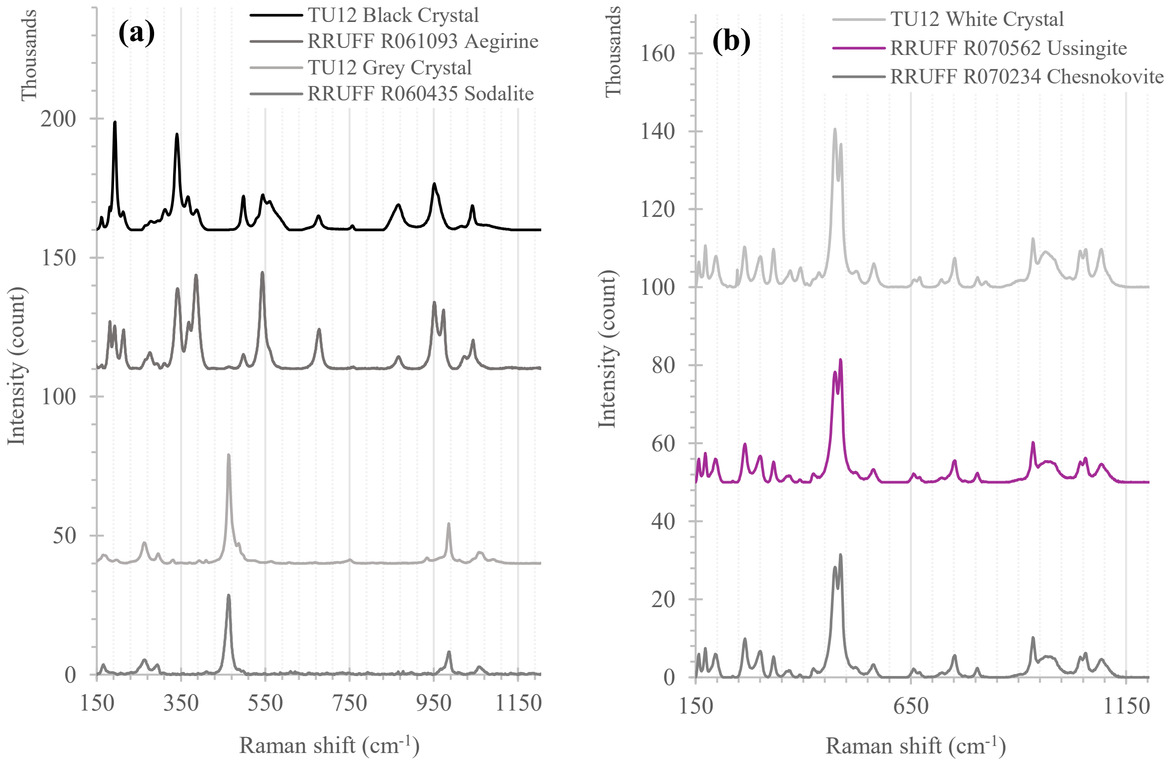

Figure 63: Micro-Raman spectra of TU12 associated minerals compared to Raman spectra of reference minerals from the RRUFF database. Spectra have been modified and shifted for clarity.

As for TU11, the morphological comparison between *figures 64 and 65* of TU12 with *figure 62* supports its identification as ussingite.

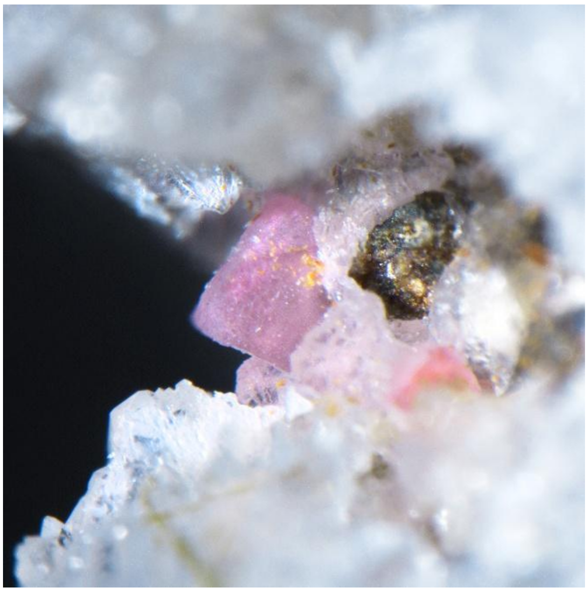

Figure 65: TU12 tugtupite crystal associated with presumed ussingite and sodalite from Mont Saint-Hilaire, Canada. Photomicrograph by Claire Chapuis, taken with a Nikon SMZ25 microscope. Field of view: 6.29 mm.

Figure 64: TU12 aegirine crystal associated with presumed ussingite and sodalite from Mont Saint-Hilaire, Canada. Photomicrograph by Claire Chapuis, taken with a Nikon SMZ25 microscope. Field of view: 6.29 mm.

Regarding sample TU13, the previous Raman spectrum of the pink crystal was identified as eudialyte (*figure 42*), with no tugtupite detected. However, the study of its associated minerals remains relevant since eudialyte and tugtupite often occur within the same geological environment (*Schilling et al., 2011*). The same non-identified white mineral (matching both chesnokovite (*figure 66, gray spectrum*) and ussingite (*figure 66, violet spectrum*) in the RRUFF database) was observed once again (*figure 66*, *light gray spectrum*).

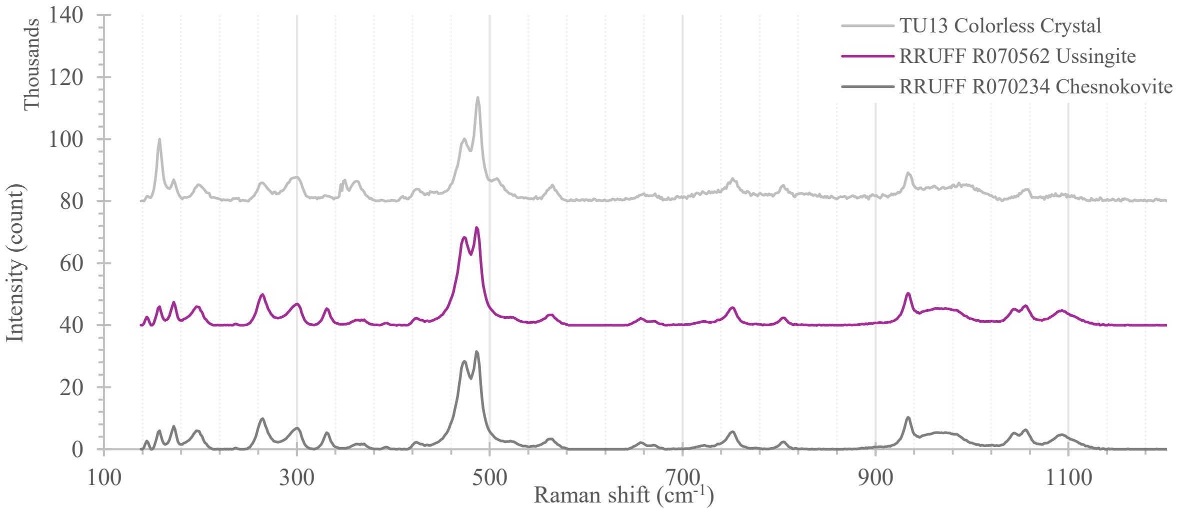

Figure 66: Micro-Raman spectra of TU13 associated minerals compared to Raman spectra of reference minerals from the RRUFF database. Spectra have been modified and shifted for clarity.

Additional minerals identified in TU13 included chkalovite (gray crystal), aegirine (greenish-black crystal), and natrolite (white crystal), as illustrated in *figure 69* and supported by microphotographs in *figures 67 and 68*.

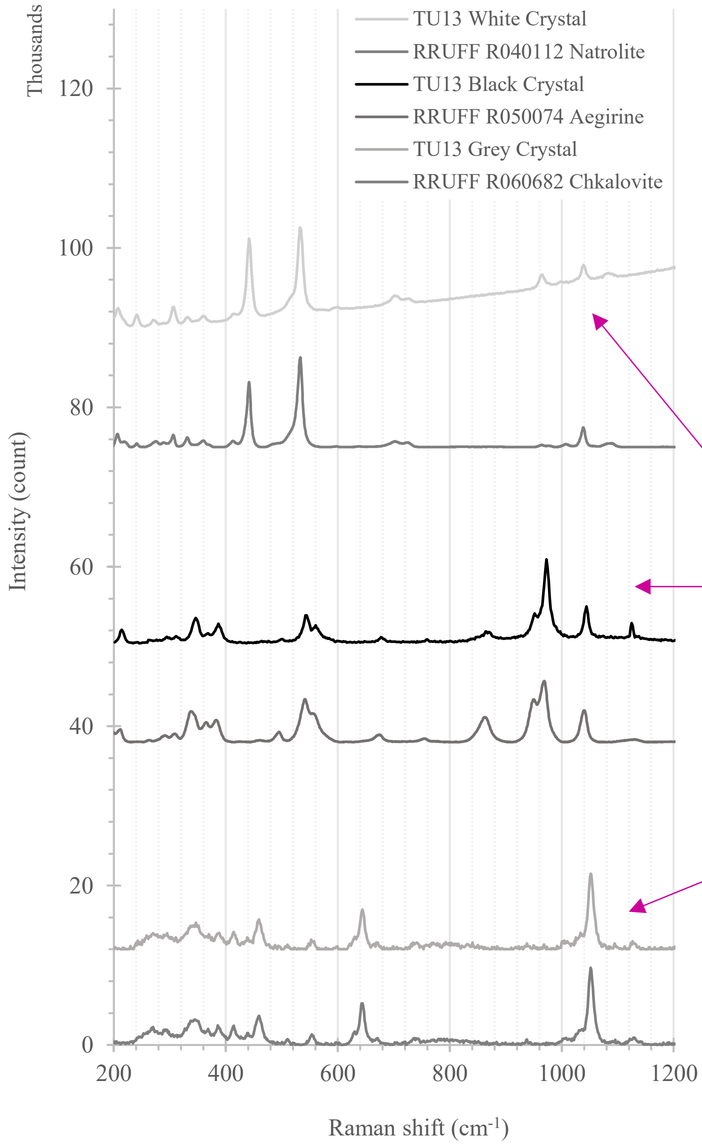

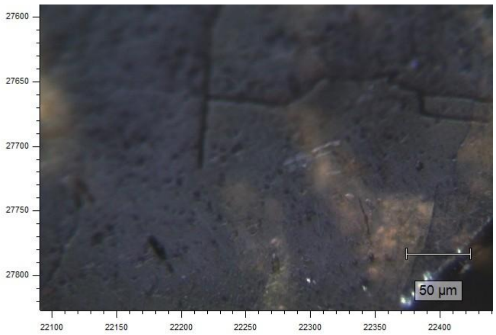

Figure 67: Photomicrography of TU13 aegirine surface crystal. Photograph by Claire Chapuis using a Renishaw InVia Raman microscope.

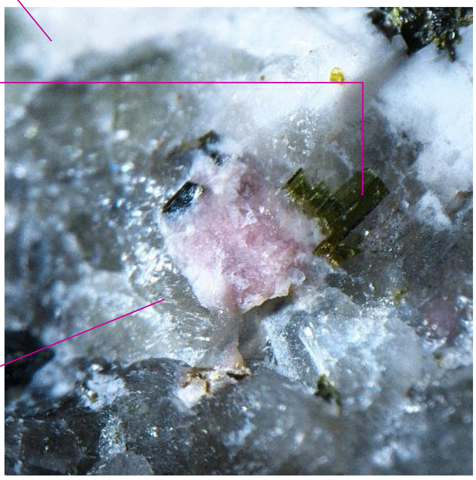

Figure 68: TU13 eudialyte crystal with chkalovite, natrolite and aegirine from Mont Saint-Hilaire, Canada. Photomicrograph by Claire Chapuis using a Nikon SMZ25 microscope. Field of view: 11 mm.

Figure 69: Micro-Raman spectra of TU13 associated minerals compared to Raman spectra of reference minerals from the RRUFF database. Spectra have been modified and shifted for clarity.

- **Russian samples**

In sample TU14, two minerals were identified in association with tugtupite (*figure 71*). Comparison with RRUFF minerals reference spectra indicated the presence of chkalovite (gray crystal) and sphalerite (brown crystal). The corresponding photomicrographs are shown in *figure 70*.

Figure 70: Photomicrographs of TU14 inclusions by Claire Chapuis using a Nikon SMZ25 microscope. Field of view: 5.36 mm (bottom) and 4.07 mm (top).

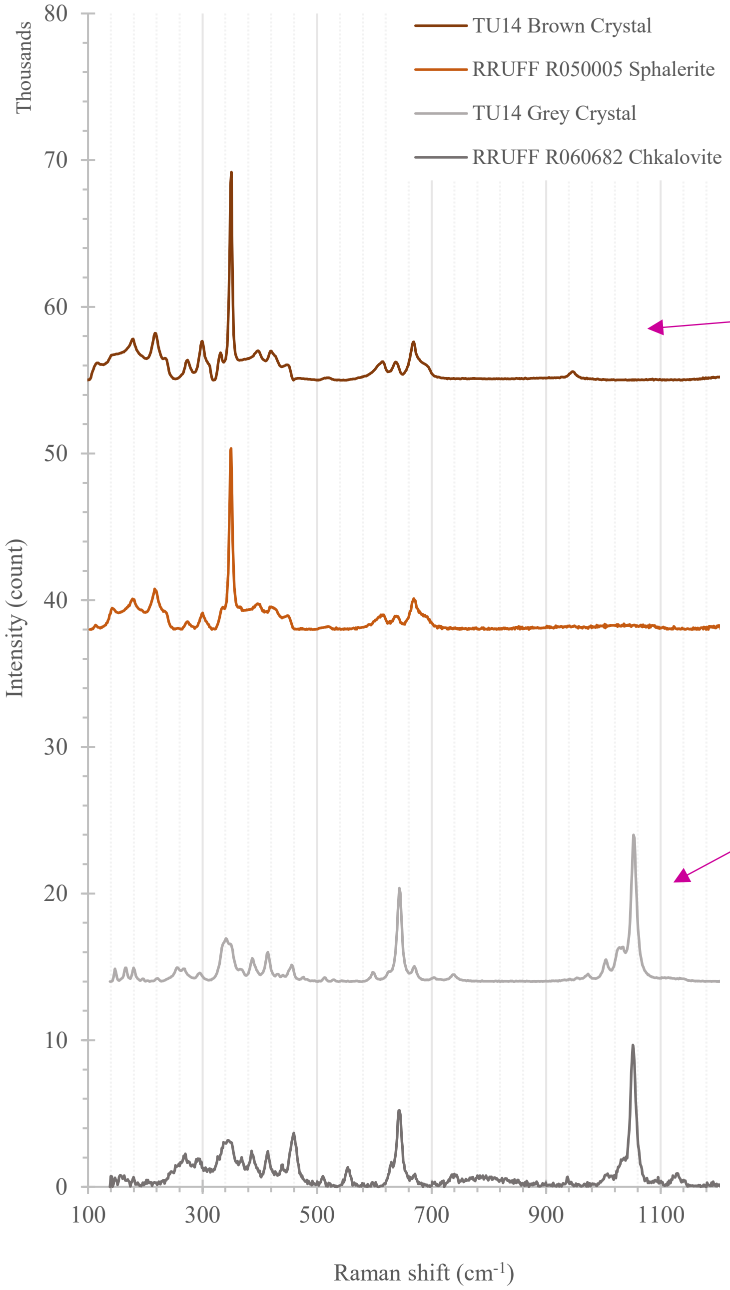

Figure 71: Micro-Raman spectra of TU14 associated minerals compared to Raman spectra of reference minerals from the RRUFF database. Spectra have been modified and shifted for clarity.

Again, for sample TU15, no tugtupite was detected. Instead, Raman analyses revealed manganoneptunite for the main pinkish-red crystal, while the adjacent pink phase was identified as ussingite, which can be also considered as a "mineral confusion" of tugtupite. Other associated minerals, presented in *figure 73*, include sphalerite (*brown spectrum*) and neptunite (*black spectrum*), result consistent with RRUFF database matches.

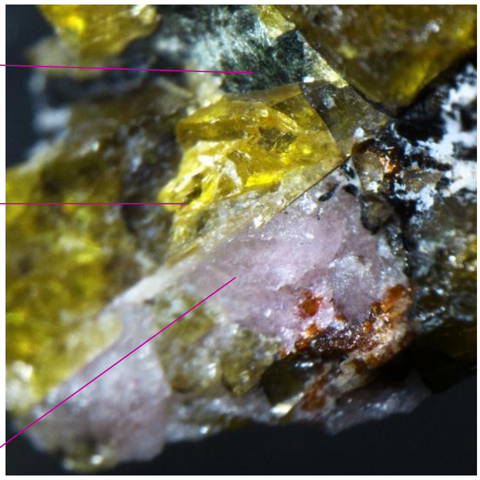

Figure 72: Photomicrograph of TU15 inclusions by Claire Chapuis using a Nikon SMZ25 microscope. Field of view: 11.58 mm.

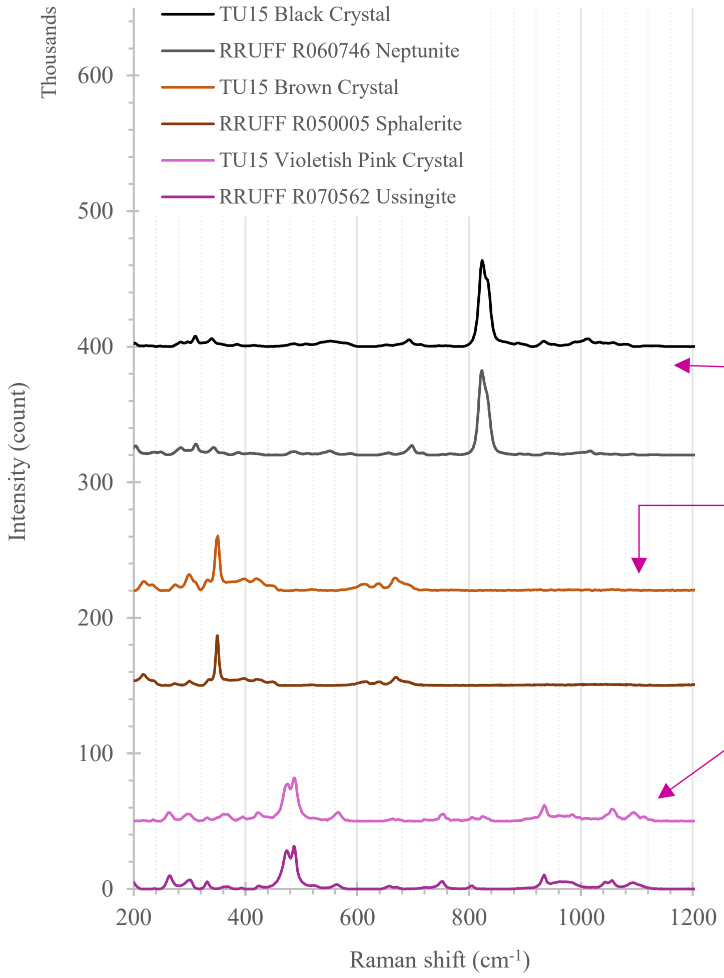

Figure 73: Micro-Raman spectra of TU15 associated minerals compared to Raman spectra of reference minerals from the RRUFF database. Spectra have been modified and shifted for clarity.

Scanning Electron Microscope (SEM)

The results of SEM chemical analyses of samples TU01 to TU06 are presented in the tables in *Annex III*, while additional BSE images can be found in *Annex IV*. These backscattered electron (BSE) images revealed the presence of numerous minerals associated with tugtupite, providing a detailed view of the mineralogical context of each sample.

In TU01, chemical analyses identified a variety of associated minerals, including albite, chkalovite, microcline, neptunite, manganoneptunite, barylite, and either a Nb-rich, Ce-bearing eudialyte or a member of the pyrochlore group. The BSE images (*figure 74*) illustrate the spatial distribution of these minerals within the sample, and reflect the specific formation process of tugtupite described by *Sørensen et al.* (1971). Distinct crystallization stages were observed, such as albite patches, tugtupite enclosing chkalovite, and commonly co-occurring minerals like neptunite and microcline.

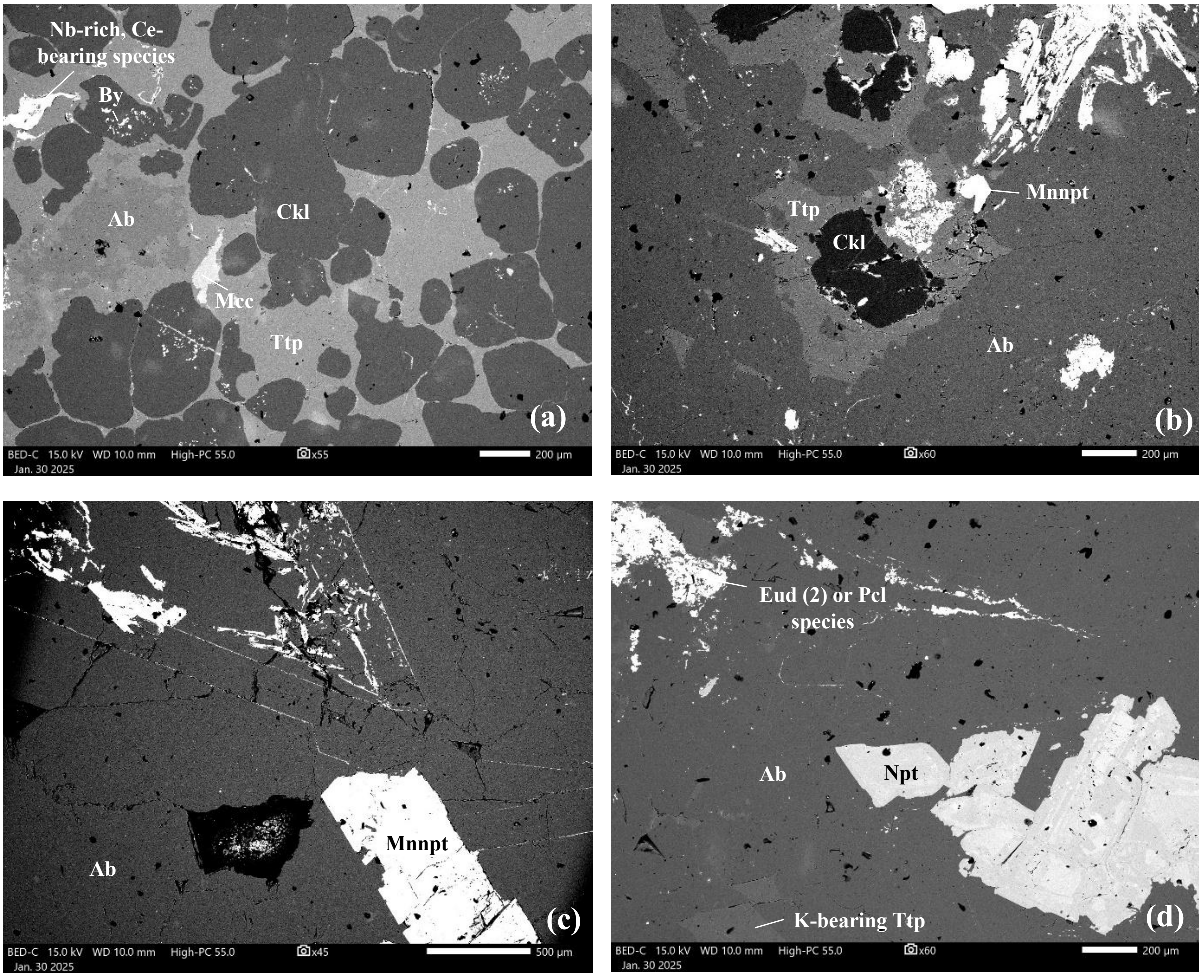

Figure 74: Backscattered electron (BSE) images of the TU01 thick section associated minerals. (a) Tugtupite enclosed by albite, chkalovite, microcline, and a Nb-rich, Ce-bearing species suggests member of the pyrochlore or eudialyte group; barylite occurs with chkalovite. (b) Tugtupite in association with albite, chkalovite, and manganoneptunite. (c) Close-up view showing albite and manganoneptunite within TU01. (d) Close-up view of K-bearing tugtupite associated with albite, neptunite, and a suggested member of pyrochlore or eudialyte group.

Backscattered electron (BSE) images presented in *figure 75* showed the minerals in association with tugtupite in TU03 (*figure 75, (a)*), TU04 (*figure 75, (b)*), TU05 (*figure 75, (c)*), and TU06 (*figure 75, (d)*).

In TU03, different feldspars were identified: "pure" albite, a feldspar containing ~35% albite, and another containing ~42% anorthite. Additionally, an unidentified Ba-bearing species was seen enclosed within tugtupite. Lighter gray areas within the tugtupite contained a K-bearing tugtupite component, similar to that observed in TU01 (*figure 74, (d)*).

In TU04, tugtupite occurred as veins within the albite, associated with a Nb-rich, Ce- and U-bearing species enclosed in an albite patch. This crystal differs from TU01 by containing uranium, suggesting a Nb-, Ce-, and U-bearing species from the eudialyte group (*Steenfelt & Bohse, 1975*). However, pyrochlore cannot be excluded due to its chemical similarities (*see Table "Likely a Nb-rich, Ce- and U-bearing member of the eudialyte or pyrochlore group," Annex III*). Again, a lighter gray patch in tugtupite area (*red circle in figure 75, (b)*) may indicate a K-bearing tugtupite component as observed in TU01 and TU03.

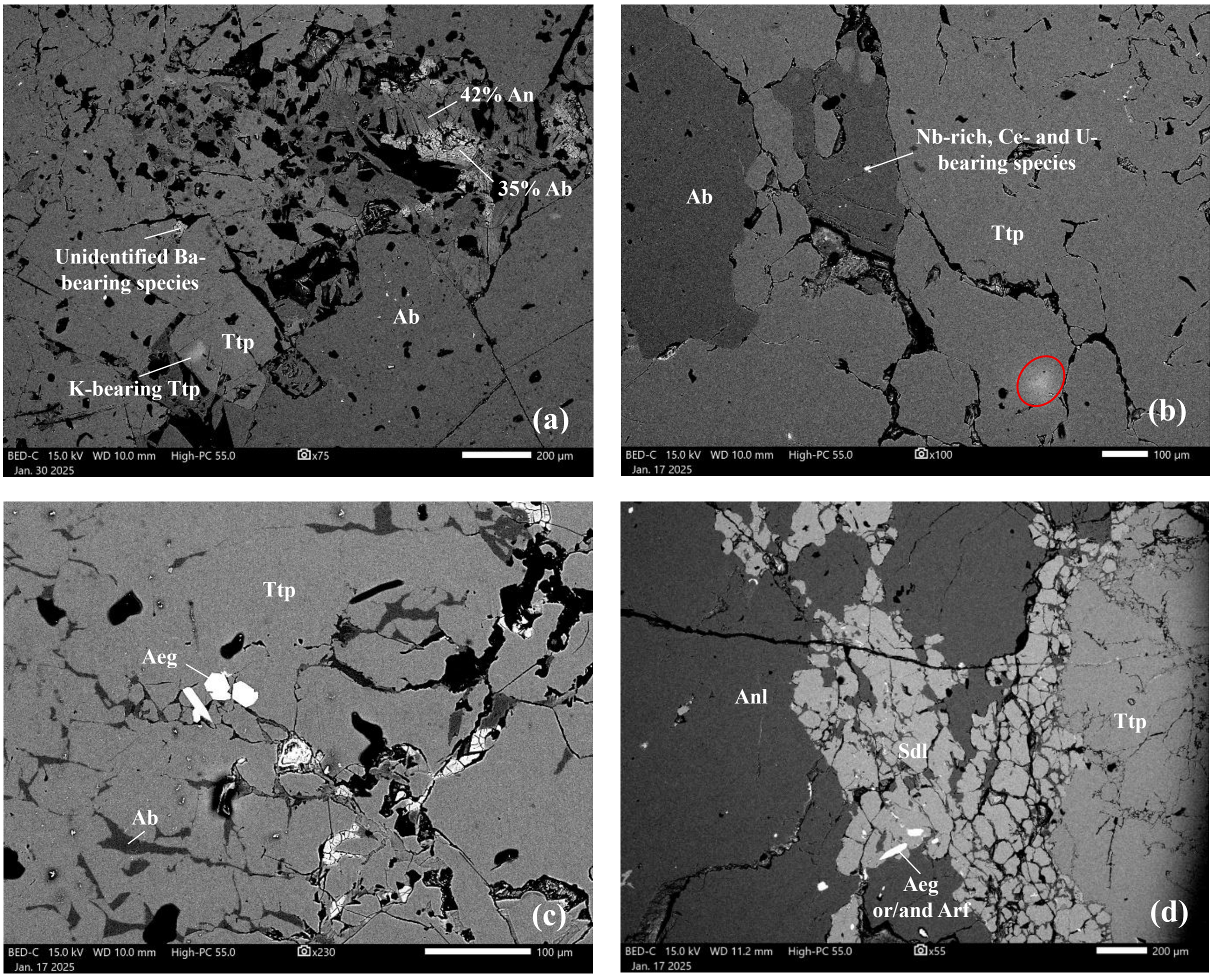

Figure 75: Backscattered electron (BSE) of samples TU03 to TU06 showing associated minerals. (a) TU03: thick section of tugtupite associated with k-bearing tugtupite, "pure" albite, albite (~35%) and anorthite (~42%) and unidentified Ba-bearing species. (b) TU04: thick section of tugtupite surrounded by albite and Nb-rich, Ce- and U- bearing species suggests to be a member of the pyrochlore or eudialyte group. (c) TU05: thick section of tugtupite associated with albite and aegirine. (d) TU06: thick section of tugtupite associated with analcime, sodalite, and aegirine and/or arfvedsonite.

In TU05 (*figure 75, (c)*), albite veins were observed within the tugtupite, enclosing well-defined aegirine crystals.

Finally, in TU06 (*figure 75, (d)*), analcime and sodalite were present, with sodalite enclosing crystals potentially representing aegirine or arfvedsonite. Further analyses are required to distinguish these minerals, which frequently form intergrowths or mixed phases during crystallization (*Wormald & Price, 1988*).

The observed crystallization patterns and the distribution of associated minerals in these samples are consistent with previously published reports (*Sørensen et al., 1971; Steenfelt & Bohse, 1975; Schilling et al., 2011*), confirming the typical sequence of tugtupite formation.

Summary of sample identification and their associated minerals

Table X summarizes the associated minerals identified in each sample (except TU09, TU10, and TU16) from the three localities, in both micro-Raman and SEM analyses, and in comparison, with those reported in literature.

Table IX: Summary of the mineralogical characterization of samples TU01 to TU15 (except TU09, TU10 and TU16), including sample identification results, localities, and associated minerals identified by micro-Raman spectroscopy and SEM analyses, in comparison to literature data.

Sample identification Name	*Sample identification result*	*Sample locality*	*Associated minerals (Micro-Raman)*	*Associated minerals (SEM)*	*Associated minerals (from literature*)*
TU01	Tugtupite	Narsap Ilua, Kujalleq, **Greenland**	Albite Chkalovite Neptunite	Albite *Barylite** Chkalovite K-bearing tugtupite Manganoneptunite Microcline Neptunite Nb-rich, Ce-bearing pyrochlore or eudialyte	**Kvanefjeld area & Taseq Plateau** Aegirine Albite Analcime Arfvedsonite Chkalovite Li-mica Microcline Neptunite Pyrochlore Ussingite
TU02	Tugtupite	Narsap Ilua, Kujalleq, **Greenland**		Albite Microcline	
TU03	Tugtupite	Narsap Ilua, Kujalleq, **Greenland**		Albite ~35% Albite *~42% Anorthite** K-bearing tugtupite *Unidentified Ba-species**	
TU04	Tugtupite	Narsap Ilua, Kujalleq, **Greenland**		Albite Nb-rich, Ce- & U-bearing pyrochlore or eudialyte	
TU05	Tugtupite	Narsap Ilua, Kujalleq, **Greenland**	Albite Arfvedsonite	Albite Arfvedsonite	
TU06	Tugtupite	**Greenland**		Analcime Aegirine or/and Arfvedsonite Sodalite	**Greenland (All locations)** Aegirine Albite Analcime Arfvedsonite Chkalovite Epistolite Li-mica Microcline Neptunite Pyrochlore Schizolite Sodalite Sphalerite Steenstrupine Ussingite
TU07	Tugtupite	**Greenland**	Chkalovite Neptunite		
TU08	Tugtupite	**Greenland**	Pyrochlore		
TU11	Tugtupite	Mont Saint-Hilaire **Canada**	*Aegirine** Sodalite *Ussingite**		**Mont Saint-Hilaire complex**

TU12	Tugtupite	Mont Saint-Hilaire **Canada**	*Aegirine** Sodalite *Ussingite**		Albite Analcime Eudialyte group Natrolite Sodalite
TU13	Eudialyte group	Mont Saint-Hilaire **Canada**	*Aegirine** *Chkalovite** Natrolite *Ussingite**		
TU14	Tugtupite	Karnasurt, Lovozero, Kola **Russia**	Chkalovite Sphalerite		**Lovozero Intrusion (All locations)** Aegirine Albite Analcime Chabazite Chkalovite Epistolite Microcline Natrolite Neptunite Schizolite Sphalerite Steenstrupine Ussingite
TU15	Mangano-neptunite (reddish-pink crystal) & Ussingite (pink phase mineral)	Shkatulka pegmatite, Alluaiv, Lovozero, Kola **Russia**	Neptunite Sphalerite Ussingite		

**Yakovlevskaja et Semenov, 1963; Sørensen et al., 1971; Markl et Baumgartner, 2002; Schilling et al., 2011; Milisenda et al., 2015; Mindat, 2025*

**Minerals identified in this study but not previously reported in the literature for corresponding locality.*

Samples TU01 to TU05 originate from the area between Kvanefjeld and the Taseq Plateau in Greenland. Comparisons show that the minerals associated with the tugtupite samples were generally consistent with the literature (*Sørensen et al., 1971*), except for the absence of minerals from the eudialyte group, as well as anorthite, barylite and barium-bearing species.

For the Canadian samples from Mont Saint-Hilaire (TU11 to TU13), only sodalite and natrolite have been reported in the literature (*Schilling et al., 2011*). However, chkalovite, ussingite, and aegirine, commonly associated with tugtupite in other localities, were also observed here. The lack of information regarding associated minerals in the Mont Saint-Hilaire complex is probably due to the limited literature available on tugtupite formation in this locality.

Regarding TU14 and TU15, collected from the Lovozero intrusion, the identified associated minerals were also consistent with those described in the literature (*Yakovlevskaja & Semenov, 1963; Sørensen et al., 1971*). The pink mineral surrounding the manganoneptunite crystal, which matches both chesnokovite and ussingite in the RRUFF Raman database reference spectra, was identified as ussingite based on its color. Although chesnokovite has been reported as being exclusively found in Russia, particularly in the Lovozero intrusion, it is described as colorless, whereas ussingite typically exhibits pale to medium violet, reddish-violet, or purple colors (*Mindat, 2025*).

CHAPTER IV: Discussion

Classical Gemology

Classical gemological observations on all tugtupite-bearing samples in this study were consistent with previously published descriptions of the mineral (*Dragsted, 1970; Sørensen et al., 1971; Finch et al., 2016; Blumentritt & Fritsch, 2021*). The "unknown" locality TU10 sample is attributed to Greenland, as the size of the tugtupite-bearing area exceeds 3 mm (*Sørensen et al., 1971)*. All analyzed specimens exhibited an orangey-red luminescence under short-wave UV, with variable intensity and a weak to moderate orange luminescence under long-wave UV. In most cases, luminescence was stronger under short-wave UV. Uneven distribution of luminescence was frequently observed in samples containing accessory minerals. No visible phosphorescence was detected. These observations are consistent with previous studies on tugtupite luminescence (*Dragsted, 1970; Povarennykh et al., 1971*).

The photochromic behavior observed in this study also aligns with descriptions in the literature (*Milisenda et al., 2015; Blumentritt & Fritsch, 2021; Gao & Sun, 2023*). All samples display a reversible change of color value ranging from light or medium pink to dark pink, intense purplish-pink, or pinkish-red upon UV exposure. The fading of color in darkness was observed over several weeks, consistent with the recovery times reported by *Milisenda et al.* (2015), and longer than those described by *Blumentritt & Fritsch* (2021) and *Gao & Sun* (2023).

Microscopic examination revealed several characteristic inclusions previously documented in tugtupite (*Sobolev et al., 1970; Gao & Sun, 2023*). Sample TU05 contained an unidentified, partially corroded colorless crystal. Fluid inclusions and typical healed fractures were observed in TU01 and TU05, that have been captured during crystallization at temperatures between 440 °C and 460 °C (*Sobolev et al., 1970*).

Laboratory Gemology

Tugtupite Identification and Characterization

Fourier-Transform InfraRed Spectroscopy

The FTIR spectra obtained for the Greenland tugtupite samples represented, to the best of the author's knowledge, among the first infrared data ever reported for this mineral. The most crystalline specimens produced transmission spectra showed a series of broad absorption bands between 1850 and 2200 cm^{-1}, with distinct peaks at 1990, 2091, and 2175 cm^{-1}. A broad band between 3100 and 3700 cm^{-1} corresponded to structural water incorporated during crystallization (*Povarennykh et al., 1971; Mindat, 2025*). Variation of intensities in this band among samples could indicate differences in structural water content related to the crystallization conditions.

The reflectance spectra of the opaque samples reveal two initial peaks at 474 and 534 cm^{-1}, followed by two weak bands at 619 and 659 cm^{-1}. Additional well-defined peaks occurred at 746, 797, and 1028 cm^{-1}, followed by weaker features at 1062 and 1110 cm^{-1}. Finally, a small band was observed around 1200 cm^{-1}.

Further research is required to fully identify these features, except for the broad H_2O band, which is well established.

UV-Visible Spectroscopy

The UV-Visible spectra of samples TU01 and TU03 are consistent with previous observations (*Povarennykh et al., 1971; Blumentritt & Fritsch, 2021*). A broad absorption band between 440 and 600 nm, centered near 507 nm in TU03 and 511 nm in TU01, is responsible for the pink to purplish-red coloration of tugtupite. This band becomes significantly more intense and slightly shifted in the photo-induced metastable state, indicating activation of color centers under UV irradiation. This broad absorption band corresponds to the absorption between the cyan and green region of the spectrum. Consequently, the transmitted light appears light pink to pink in the stable state and pinkish-red to purplish-pink in the metastable state, depending on the intensity of the band and the sample studied. A secondary band at 375 nm may correspond to the strong UV luminescence of tugtupite. Indeed, it appears to be the same peak observed at 375 nm in the TU08 excitation spectrum for the emission at 685 nm (*see figure 48*).

Differential spectral analysis suggests the presence of two distinct Gaussian components, corresponding to the two types of color centers previously identified by *Blumentritt & Fritsch* (2021). However, the specific peak assignments were not determined in this study.

Fourier-Transform Raman and Micro-Raman Spectroscopy

FT-Raman spectra of the Greenland samples match the RRUFF reference spectrum for tugtupite, confirming its identification. Several characteristic bands were observed between 150-650 cm^{-1} and 1000-1200 cm^{-1}. As with FTIR, further investigation is necessary to determine the precise origin of these features.

Micro-Raman spectroscopy allowed the identification of samples that could not be conclusively characterized by FT-Raman. TU11, TU12, and TU14 were confirmed as being tugtupite based on comparison with RRUFF reference spectra. In contrast, TU13, TU15, and TU16 were identified as other minerals commonly associated with tugtupite: TU13 corresponds to a probable manganoeudialyte (Mn-rich member of the eudialyte group), TU15 to manganoneptunite (Mn-rich member of neptunite group), and TU16 to sodalite var. hackmanite. These results highlight possible confusion, as these specimens had previously been named after tugtupite.

Chemical Analyses (EDX-SEM and EDXRF)

EDX-SEM chemical analyses (performed in both metallic and oxide modes) and semi-quantitative EDXRF analyses were conducted exclusively on Greenland tugtupite samples, due to the fragility and small size of other specimens. Furthermore, light elements such as beryllium could not be reliably quantified due to both instrumental limitations.

Regarding the EDX-SEM analyses, the measured elemental compositions are consistent with literature values (*Danø, 1966; Mindat, 2025*), showing only minor differences from reference data, that could be due to normalization and the difference in sample formation.

EDXRF analyses revealed the presence of numerous impurities in addition to the primary constituents (i.e., Na, Al, Si, and Cl). Some of these elements have been previously reported (K, Ca, Mn, Fe, Ga, Mg, and S) (*Semenov & Bykova, 1960; Danø, 1966; Mindat, 2025)*, while others appear to be unreported in the literature. All samples contained sulfur in relatively high concentrations (ranging from 4778 to 9571 ppm), except for TU09.

Several hypotheses may account for this observation. First, sulfur may not be systematically incorporated into the crystal structure, which could explain its removal from the original chemical formula by the International Mineralogical Association (IMA). Second, sulfur, as well as the other numerous impurities identified, may originate from associated minerals present within the sample matrix. Indeed, backscattered electron images (*see figures 74a, 74b, 74d, and figure 75*) reveal complex mineral assemblages, with multiple phases, including tugtupite and others associated minerals as barylite, eudialyte, aegirine, arfvedsonite or manganoneptunite, occurring within small areas (approximately 100-200 µm). This calls into question the role of sulfur in the photochromic behavior of tugtupite, especially in sample lacking of this element.

Therefore, it would be interesting to perform an analysis on a single tugtupite crystal to determine whether the presence of numerous impurities is due to associated minerals in the matrix or whether they are intrinsic to the tugtupite structure.

Luminescence and Phosphorescence Spectroscopy

Advanced luminescence analyses confirm the coexistence of several luminescence centers in tugtupite, consistent with previous studies on this mineral and related aluminosilicates:

- **S_2^- polyanions:** responsible for the orange luminescence observed under LWUV excitation, their vibrational structure, characterized by several bands between 500 and 700 nm (*Povarennykh et al., 1971; Gaft et al., 2009*), has been observed in TU04, TU06 and TU08 spectra.
- **Fe^{3+} substitutions:** characterized by a broad emission band centered at 670 nm under SWUV excitation, responsible for the red luminescence (*Gaft et al., 2009; Warner & Andersen, 2012*). Broad bands centered around 676-679 nm under SWUV have been observed in TU01, TU02, TU03 and TU06. It is also probably Fe^{3+} which is responsible for the red luminescence, corresponding to broader emission bands between 680 and 689 nm, present in TU02, TU04, TU05, and TU07-TU10 samples, although there is no information reported in the literature, since an orangey-red luminescence is observed under SWUV in all tugtupite samples.
- **S^2 type centers:** characterized by a band near 430 nm under SWUV and responsible for the UV-blue luminescence (*Gaft et al., 2009*). Broad emission bands between 421 and 444 nm were detected in TU01, TU03, and TU05, showing slight differences from the literature. This center could also contribute to bands observed under LWUV peaking at 421 nm (TU05) and 425 nm (TU08). Since these emissions are in the UV range, it is maybe the reason why they are less visible under the UV lamp, or maybe it acts as a secondary luminescence center.

Therefore, the 375 nm band observed in the UV-Visible spectra (*see figure 38*) appears to correspond to the same feature detected in the TU08 excitation spectrum for the emission at 685 nm (*see figure 48*). This suggests that this band observed in the UV-Visible spectra of TU01 and TU03 may be linked to the UV luminescence of the specimen.

Finch et al. (2016) reported that red-infrared luminescence in minerals of the sodalite group is commonly attributed to tetrahedrally coordinated Fe^{3+} substituting for Al^{3+}, although the mechanisms can be more complex depending on the specific mineral. For example, in pink sodalite, the luminescence may involve one or both Fe^{3+} and Cr^{3+}. In tugtupite, it has been suggested that the emission may result from a combination of red luminescence from both S_2^- and tetrahedral Fe^{3+} centers.

Additionally, a similar band is observed with a slight shift peaking at 378 nm in the TU08 excitation spectrum corresponding to an emission at 674 nm (*see figure 51*). This 674 nm band was previously observed in TU08 emission spectrum at 365 nm (*see figure 49*). As the orange luminescence under LWUV (365 nm) is characterized by a several broad bands between 500 and 700 nm, typically attributed to the S_2^- vibronic structure, and the red luminescence under SWUV (254 nm) is shown through a broad band around 670 nm, and typically associated with Fe^{3+}, taken together, the presence of excitation peaks around 375-378 nm for emissions at both 685 nm and 674 nm suggests that this UV excitation band may involve contributions from both Fe^{3+} and S_2^- centers.

Tugtupite samples in this present study exhibited extremely short-lived phosphorescence, imperceptible to the naked eye, consistent with the work of *Gao & Sun* (2023). Further studies are needed to determine the duration, elemental origin of this phosphorescence, and its relationship to luminescent centers.

Associated minerals identification

Across all analyzed samples, micro-Raman, and SEM-EDS analyses revealed consistent mineral assemblages typical of tugtupite-bearing environments, providing complementary insights into their paragenesis and crystallization conditions in Greenland, Canada, and Russia.

Micro-Raman

Across all analyzed samples, several recurrent mineral associations were identified in relation to tugtupite or within its characteristic paragenetic environment.

Gray crystals were mainly identified as chkalovite in samples TU01, TU07, TU13, and TU14, or as sodalite in TU11 and TU12. Albite appeared as grayish-white crystals in TU01 and TU05, while white crystals corresponded to pyrochlore in TU08 and natrolite in TU13. The pink crystalline phases were attributed to ussingite, present in samples TU11, TU12, TU13, and TU15. Sphalerite was recognized as the brown crystal in TU14 and TU15. Among the black or greenish-black minerals, neptunite occurred in TU01 and TU07, arfvedsonite in TU05, and aegirine in TU11, TU12, and TU13.

Altogether, these results show consistent mineralogical assemblages across the Greenland, Canadian, and Russian samples, supporting a common atomic association between tugtupite and several sodium-rich silicate phases, such as chkalovite, ussingite, sodalite, albite, aegirine, arfvedsonite, and neptunite, together with accessory minerals including pyrochlore, natrolite, and sphalerite. These associations indicate crystallization under peralkaline magmatic conditions typical of the environments where tugtupite forms.

Energy-Dispersive X-ray – Scanning Electron Microscope (EDX-SEM) and Backscattered (BSE) images

SEM chemical analyses results and backscattered electron (BSE) images reveal the presence of numerous minerals associated with tugtupite, providing a detailed view of the mineralogical context of each sample. The common associated minerals found in the Greenland samples studied are: albite, anorthite, analcime, chkalovite, microcline, sodalite, neptunite, manganoneptunite, aegirine or/and arfvedsonite, barylite, Ba-bearing species, part of K-bearing tugtupite and either a Nb-rich, Ce- or/and U-bearing eudialyte or a member of the pyrochlore group.

The presence of barylite in sample TU01 is particularly significant, representing, to the author's knowledge, the first documented occurrence of this mineral in association with tugtupite. This association, together with a highly Nb-rich ($Nb_2O_5 > 50$ % element mass) and Ce-bearing phase, suggests the formation of tugtupite in environments enriched in incompatible and high-field-strength elements (HFSE) such as Nb, Ta, Zr, Y, and REE. During the transition from magmatic to hydrothermal stages, volatile-rich fluids containing Na, Cl, F, and large-ion lithophile elements (LILE, e.g., Ba) likely circulated through the peralkaline syenite, promoting the crystallization of secondary and rare minerals (*Schilling et al., 2011*). These observations suggest that the previously unidentified Nb- and Ce-rich mineral phases associated with tugtupite may represent a Nb-enriched variety of eudialyte not detected during micro-Raman analyses.

The observed crystallization patterns such as albite patches or tugtupite enclosing chkalovite, and the distribution of associated minerals in these samples are consistent with previously published reports (*Sørensen et al., 1971; Steenfelt & Bohse, 1975; Schilling et al., 2011*), confirming the typical sequence of tugtupite formation.

In summary, the mineral associations observed in all samples are generally consistent with previous studies, with some local differences. Minerals such as aegirine, albite, analcime, chkalovite, sodalite, and ussingite are commonly found with tugtupite in Greenland, Canada, and Russia, reflecting similar peralkaline magmatic conditions. The absence of some minerals, like barylite, may be due to local geological variations or limited literature. Overall, these results confirm that tugtupite forms in evolved, sodium-rich environments where fluid-rock interactions influence the final mineral assemblage.

CONCLUSION AND OUTLOOK ON FUTURES ANALYSES

This study provides a detailed characterization of tugtupite from its three main localities: Greenland, Canada, and Russia. The research focused on its identification as a gemstone, its physical and optical properties, luminescence behavior, and its mineralogical associations, highlighting both common features and local variations.

Classical gemological observations confirmed its reversible photochromic behavior, and luminescence colors under both short-wave and long-wave ultraviolet radiation, consistent with previous studies. Moreover, visual examination suggests that TU10 sample is probably from Greenland, and microscopic examinations revealed inclusions, healed fractures, and fluid inclusions that reflect typical crystallization conditions.

Advanced spectroscopic analyses (FTIR, UV-Vis, FT-Raman, and micro-Raman) allowed reliable identification of tugtupite and distinguished it from associated or visually similar minerals such as manganoeudialyte, manganoneptunite, and hackmanite. Advanced luminescence analyses revealed the existence of multiple centers, including S_2^- polyanions, Fe^{3+} substitutions, and S^2 type centers, explaining the diverse luminescence color emissions and confirming previous studies.

Micro-Raman and SEM analyses allow to identify minerals in association with tugtupite across all localities. Analyses on Greenland samples revealed non-report minerals, such as barylite, Nb-rich and Ce-bearing species, confirming its crystallization in peralkaline environments rich in high-field-strength elements and volatile-rich fluids. Canadian samples exhibited similar associations, though less documented in the literature, while Russian samples confirmed previously reported mineral association.

Overall, tugtupite exhibits consistent optical, luminescent, and mineralogical features across Greenland, Canada, and Russia. Differences in associated minerals likely reflect local geological conditions and formation environments. These findings provide a better understanding of its formation and paragenesis.

Further investigations are required in several aspects. More comprehensive chemical analyses using LA-ICP-MS would be particularly valuable for quantifying beryllium and verifying the statement of *Danø* (1966) regarding the sulfur content. In addition, the element responsible for the photochromic behavior of tugtupite remains to be identified, as does the origin of differences in fading time when samples are kept in the dark. Further work is also needed to identify features observed in the FTIR and Raman spectra and to distinguish co-occurring, yet unidentified, associated minerals such as aegirine/arfvedsonite, barium-bearing phases, and Nb-rich, Ce-, U-, and/or F-bearing species. Finally, additional studies on the luminescence behavior are needed to better understand why some samples exhibit a stronger luminescence under long-wave UV than under short-wave UV.

REFERENCES

Antao, S. M., and Hassan, I. 2002. Thermal Analyses of Sodalite, Tugtupite, Danalite and Helvite. *The Canadian Mineralogist,* **40**(1). pp. 163-172. https://doi.org/10.2113/gscanmin.40.1.163

Antao, S. M., Hassan I., and Parise J. B. 2004. Tugtupite: High-temperature structures obtained from in situ synchrotron diffraction and Rietveld refinements. *American Mineralogist*, **89**(4), pp. 492-497. https://doi.org/10.2138/am-2004-0403.

Armstrong, J.A., and Weller, M.T. 2006. New sodalite frameworks; synthetic tugtupite and a beryllosilicate framework with a 3:1 Si:Be ratio. *Dalton Transactions*, (24), pp. 2998–3005. https://doi.org/10.1039/b600579a.

Bailleul, P. 2023. Quand la tugtupite groenlandaise devient une pierre précieuse : Enjeux sociaux et politiques autour d'une catégorie de la ressource. *Atelier d'anthropologie [En ligne]*, Varia, mis en ligne le 18 octobre 2023. https://journals.openedition.org/ateliers/18343 Consulted 25 March 2025 (in French). https://doi.org/10.4000/ateliers.18343.

Bailey, J. C., Gwozdz, R., Rose-Hansen, J., and Sørensen, H. 2001. Geochemical overview of the Ilímaussaq alkaline complex, South Greenland. *Geology of Greenland Survey Bulletin*, **190**(190), pp. 35-53. https://doi.org/10.34194/ggub.v190.5172.

Blumentritt F. 2021. Matériaux à propriétés ciblées par minéralomimétisme : Le photochromisme de la sodalite et de la scapolite. PhD dissertation. Université de Nantes, Nantes, France, 248 pp (in French). https://theses.hal.science/tel-05353535v1

Blumentritt, F., and Fritsch, E. 2021. Photochromism and Photochromic Gems: A Review and Some New Data (Part 1). *Journal of Gemmology*, **37**(8), pp. 780-800. https://doi.org/10.15506/JoG.2021.37.8.780.

Blumentritt, F., Latouche, C., Morizet, Y., Caldes, M.-T., Jobic, S., and Fritsch, E. 2020. Unravelling the origin of the yellow-orange luminescence in natural and synthetic scapolites. *Journal of Physical Chemistry Letters*, **11**(12), pp. 4591–4596. https://doi.org/10.1021/acs.jpclett.0c00712.

Bouas-Laurent, H., and Durr, H. 2001. Organic photochromism (IUPAC Technical Report). *Pure and Applied Chemistry*, **73**(4), pp. 639–665. https://doi.org/10.1351/pac200173040639.

Byron, H., Norrbo, I., and Lastusaari, M. 2021. A zeolite-free synthesis of luminescent and photochromic hackmanites. *Journal of Alloys and Compounds*, **872**(159671), 7 pp. https://doi.org/10.1016/j.jallcom.2021.159671.

Colville, A. A., and Ribbe, P. H. 1968. The crystal structure of an adularia and a refinement of the structure of orthoclase. *The American Mineralogist,* **53**(1), pp. 25-37.

Danø, M. 1966. The Crystal Structure of Tugtupite – a New Mineral, $Na_8Al_2Be_2Si_8O_{24}(Cl,S)_2$. *Acta Crystallographica*, **20**(6), pp. 812–816. https://doi.org/10.1107/s0365110x66001907.

Danø, M., and Sørensen, H. 1959. An examination of some rare minerals from the nepheline syenites of south west Greenland. *Grønlands Geologiske Undersøgelse,* **20**, 39 pp. https://doi.org/10.34194/bullggu.v20.6553

Downs, R.T., and Hall-Wallace, M. 2003. The American Mineralogist Crystal Structure Database. *American Mineralogist*, **88**, pp. 247-250. https://doi.org/10.5860/choice.41sup-0262

Dragsted, O. 1970. Tugtupite. *Journal of Gemmology*, **12**(1), pp. 10–11. https://doi.org/10.15506/JoG.1970.12.1.10.

Eggenkamp, H. G. M., Marks, M. A. W., Louvat, P., and Markl, G. 2021. Bromine Isotope Variations in Magmatic and Hydrothermal Sodalite and Tugtupite and the Estimation of Br Isotope Fractionation between Melt and Sodalite. *Minerals*, **11**(4), pp. 370-379. https://doi.org/10.3390/min11040370.

Eggenkamp, H. G. M., Marks, M. A.W., Bonifacie, M., Bardoux, G., Agrinier, P., and Markl, G. 2022. Cl isotope fractionation in magmatic and hydrothermal eudialyte, sodalite and tugtupite (Ilímaussaq intrusion, South Greenland). *Chemical Geology*, **604**, pp. 120932-120943. https://doi.org/10.1016/j.chemgeo.2022.120932.

Ferguson, J. 1964. Geology of the Ilímaussaq alkaline intrusion, South Greenland. Part I. Description of map and structure. *Meddr Grøland*, **172**(4), pp. 1-81. https://doi.org/10.34194/bullggu.v39.6573

Finch, A. A., Friis, H., and Maghrabi, M. 2016. Defects in sodalite-group minerals determined from X-ray induced luminescence. *Physics and Chemistry of Minerals,* **43**(7), pp. 481-491. https://doi.org/10.1007/s00269-016-0816-7.

Flink, G. 1893. Om några mineral från Grönland. *Geologiska Föreningen i Stockholm Förhandlingar*, **15** (4), pp. 195-208. https://doi.org/10.1080/11035899309442185.

Friis, H. 2011. Sodalite—A mineralogical chameleon. *Geology Today*, **27**(5), pp. 194–198. https://doi.org/10.1111/j.1365-2451.2011.00809.x.

Fritsch, E., and Rossman, G.R. 1988. An update on color in gems. Part 2: Colors involving multiple atoms and color centers. *Gems & Gemology*, **24**(1), pp. 3–15. https://doi.org/10.5741/gems.24.1.3.

Gaft, M., Panczer, G., Nagli, L., and Yeates, H. 2009. Laser induced time-resolved luminescence of tugtupite, sodalite and hackmanite. *Physics and Chemistry of*

Minerals, **36**(3), pp. 127–141.
https://doi.org/10.1007/s00269-008-0263-1.

Gao, Y., and Sun, X. 2023. Photochromism and Phosphorescence of Tugtupite. *Journal of Gemmology,* **38**(5), pp. 429-431.
https://doi.org/10.15506/JoG.2023.38.5.429.

Grice, J. D., and Gault, R. A. 2006. Johnsenite-(Ce): A new member of the eudialyte group from Mont Saint Hilaire, Quebec, Canada. *The Canadian Mineralogist*, **44**(1), pp. 105-115.
https://doi.org/10.2113/gscanmin.44.1.105.

Henderson, C. M. B., and Taylor, D. 1977. The thermal expansion of tugtupite. Mineralogical Magazine, **41**(317), pp. 130-131.
https://doi.org/10.1180/minmag.1977.041.317.21 .

International Mineralogical Association 2025. *The New IMA List of Minerals* – A Work in Progress – Updated: May 2025 through RRUFF link.
https://mineralogy-ima.org/Minlist.htm Consulted 6 May 2025.

Irie, M. 2000. Photochromism: Memories and Switches – Introduction. *Chemical Reviews*, **5**(100), pp. 1683-1684.
https://doi.org/10.1021/cr980068l.

Janák, M., Froitzheim, N., Georgiev, N., Nagel, T. J., and Sarov, S. 2011. P-T evolution of kyanite eclogite from the Pirin Mountains (SW Bulgaria): implications for the Rhodope UHP Metamorphic Complex. *Journal of Metamorphic Geology*, **29**(3), pp. 317-322.
https://doi.org/10.1111/j.1525-1314.2010.00920.x.

Jensen, A., and Petersen, O.V. 1982. Tugtupite: A gemstone from Greenland. *Gems & Gemology*, **18**(2), pp. 90–94.
https://doi.org/10.5741/gems.18.2.90.

Johensen, O., Gride, J. D., and Gault, R. A. 1998. Kentbrooksite from the Kangerdlugssuaq intrusion, East Greenland, a new Mn-REE-Nb-F end-member in a series within the eudialyte group: Description and crystal structure. *European Journal of Mineralogy*, **10**(2), pp. 207-220.
https://doi.org/10.1127/ejm/10/2/0207.

Johnsen, O., and Grice, J. D. 1999. The crystal chemistry of the eudialyte group. *The Canadian Mineralogist*, **37**(4), pp. 865-891.

Johnsen, O., Grice, J. D., and Gault, R. A. 2001. The eudialyte group: a review. Geology of Greenland Survey Bulletin, **190**, pp.65-72.
https://doi.org/10.34194/ggub.v190.5174.

Laird, J., and Albee, A. L. 1972. Chemical Composition and Physical, Optical, and Structural Properties of Benitoite, Neptunite, and Joaquinite. *American Mineralogist*, **57**(1), pp. 85-102.

Lapache, C. 1937. The Minerals of Franklin and Sterling Hill Sussex County, New Jersey. *United States Department of the Interior, Geological Survey*. 135 pp. https://doi.org/10.3133/pp180

Larsen, A. O., and Raade, G. 1997. Pyroksener fra Oslofeltets syenittpegmatitter. Kongsberg mineralsymposium 1997, *Norsk Bergverksmuseum Skrift*. **12**, pp.16-21.

Lyalina, L. M., Selivanova, E. A., Zozulya D. R., and Ivanyuk, G. Y. 2019. Beryllium Mineralogy of the Kola Peninsula, Russia – A Review. *Minerals*, **9**(1), pp. 12-54. https://doi.org/10.3390/min9010012.

Markl, G., and Baumgartner, K. 2002. PH changes in late-magmatic peralkaline fluids. *Contributions to Mineralogy and Petrology*, 144, pp. 331-346. https://doi.org/10.1007/s00410-002-0401-6.

Mikhailova, J. A., Ivanyuk, G. Y., Kalashnikov, A. O., Pakhomovsky, Y. A. Bazai, A. V., and Yakovenchuk, V. N. 2019. Petrogenesis of the Eudialyte Complex of the Lovozero Alkaline Massif (Kola Peninsula, Russia). *Minerals*, **9**(10), pp. 581. https://doi.org/10.3390/min9100581.

Milisenda, C.C., Koch, S., Müller, S., Stephan, T., and Wild, M. 2015. Gemstones with photochromism. 34th International Gemmological Conference, Vilnius, Lithuania, pp.107-109.

Mposkoks, E., Baziotis, I., and Proyer, A. 2012. Pressure-temperature evolution of eclogites the Kechros complex in the Eastern Rhodope (NE Greece). *International Journal of Earth Sciences*, **101**(4), pp. 973-996. https://doi.org/10.1007/s00531-011-0699-2.

Nickel, E. H., and Mark, E. 1965. Arfvedsonite and Aegirine-Augite from Seal Lake, Labrador. *The Canadian Mineralogist*, **8**(2), pp. 185-197.

Panikorovskii, T. L., Mikhailova, J. A., Pakhomovsky, Y. A., Bazai, A. V., Aksenov, S. M., Kalashnikov, A. O., and Krivovichev, S. V. 2021. Zr-Rich Eudialyte from the Lovozero Peralkaline Massif, Kola Peninsula, Russia. *Minerals*, **11**(9), pp. 982-1000. https://doi.org/10.3390/mon11090982.

Petersen, O. V. 1978. The twin formation of tugtupite, a contribution. *Mineralogical Magazine*, **42**(322), pp. 251-254. https://doi.org/10.1180/minmag.1978.042.322.13.

Piard, J. 2013. Le photochromisme : définition et applications. *Le Bulletin de l'Union des Professeurs de Physique et de Chimie*, **107**(954), pp. 549-559 (in French). https://hal.science/hal-04065508v1

Piilonen, P., Mcdonald, A., and Lalonde, A. E. 1998. The crystal chemistry of aegirine from Mont Saint-Hilaire, Quebec. *The Canadian Mineralogist*, **36**(3). pp. 779-791.

Povarennykh, A.S., Platonov, A.N., Tarashchan, A.N., and Belichenko, V.P. 1971. The colour and luminescence of tugtupite (beryllosodalite) from Ilímaussaq, south Greenland. *Meddelelsev om Gronland*, **181**(14), pp. 1–12. https://doi.org/10.34194/bullggu.v95.6636

Rastsvetaeva, R. K., and Chukanov, N. V. 2012. Classification of Eudialyte-Group Minerals. *Geology of Ore Deposits*, **54**(7), pp. 487-497. https://doi.org/10.1134/S1075701512070069.

Robbins, M. 1983. Fluorescent Minerals Worldwide. In: The Collector's Book of Fluorescent Minerals. Springer, Boston, MA (not accessible online). https://doi.org/10.1007/978-1-4757-4792-8_8.

Rosenholtz, J. L., and Smith, D. T. 1942. Thermal Studies of Orthoclase and Microcline. *American Mineralogist,* **27**(5), pp. 344-349.

Steenfelt, A., and Bohse, H. 1975. Variations in the content of uranium in eudialyte from the differentiated alkaline Ilímaussaq intrusion, south Greenland: (Contribution to the Mineralogy of Ilímaussaq, no. 36). *Lithos*, **8**(1), pp. 39-45. https://doi.org/10.1016/0024-4937(75)90029-8.

Semenov, E.I., and Bykova, A.V. 1960. Beryllosodalite. *Doklady Akademii Nauk SSSR*, **133**, pp. 1191–1193 (in Russian, not accessible online).

Schilling, J., Marks, M. A. W., Wenzel, T., Vennemann, T., Horváth, L., Tarassof, P., Jacob, D. E., and Markl, G. 2011. The Magmatic to Hydrothermal Evolution of the Intrusive Mont Saint-Hilaire Complex: Insights into the Late-stage Evolution of Peralkaline Rocks. *Journal of Petrology*, **52**(11), pp. 2147-2185. https://doi.org/10.1093/petrology/egr042

Sobolev, V. S., Bazarova, T. Y., Shugurova, N. A., Bazarova, L. SH., Dolgov, YU. A., and Sørensen, H. 1970. A preliminary examination of fluid inclusions in nepheline, sorensenite, tugtupite and chkalovite from the Ilímaussaq alkaline intrusion, south Greenland. *Grønlands Geologiske Undersøgelse,* **81**, 32 pp. https://doi.org/10.34194/bullggu.v81.6621

Sørensen, H. 1962. On the occurrence of steenstrupine in the Ilímaussaq massif, Southwest Greenland. *Meddelelser om Grønland*, **167**(1), 251 pp. https://doi.org/10.34194/bullggu.v32.6566

Sørensen, H., Danø, M., Petersen, O.V., Povarennykh, A.S.,Platonov, A.N., Tarashchan, A.N., and Belichenko, V.P. 1971. On the mineralogy and paragenesis of tugtupite $Na_8Al_2Be_2Si_8O_{24}(Cl,S)_2$ from the Ilímaussaq alkaline intrusion, south Greenland. *Meddelelser om Grønland*, **181**(13), 38 pp. https://doi.org/10.34194/bullggu.v95.6635

Sørensen, H. 2001. The Ilímaussaq alkaline complex, South Greenland: status of mineralogical research with new results. *Geology of Greenland Survey Bulletin*, **190**(10), 167 pp.

Tunzi, J., and Pearson, G. 2008. Hackmanite, tugtupite and afghanite – Tenebrescence and fluorescence of some sodalite related minerals. *Australian Gemmologist*, **23**(8), pp. 349–355.

Vertriest, W., Palke, A. C., Renfro, N. D. 2019. Field Gemology: Building a Research Collection and Understanding the Development of Gem Deposits. Gems & Gemology, **55**(4), pp. 491-511. https://doi.org/10.5741/gems.55.4.490

Warner, T.E., and Hutzen Andersen, J. 2012. The effects of sulfur intercalation on the optical properties of artificial 'hackmanite', $Na_8[Al_6Si_6O_{24}]Cl_{1.8}S_{0.1}$; 'sulfosodalite', $Na_8[Al_6Si_6O_{24}]S$; and natural tugtupite, $Na_8[Be_2Al_2Si_8O_{24}](Cl,S)_{2-\delta}$. *Physics and Chemistry of Minerals*, **39**(2), pp. 163–168. https://doi.org/10.1007/s00269-011-0471-y.

Warr, L. N. 2021. IMA-CNMNC approved mineral symbols. *Mineralogical Magazine*, **85**(3), pp. 291-320. https://doi.org/10.1180/mgm.2021.43.

Wormald, R., and Price, R. C. 1988. Peralkaline granites near Temora, southern New South Wales: Tectonic and Petrological implications. *Australian Journal of Earth Sciences*, **35**(2), pp. 209-221. https://doi.org/10.1080/14400958808527941.

Yakovlevskaja, T. A., and Semenov, E. I. 1963. [New data on Chkalovite]. *Trudy miner. Muz.* **14**, pp. 265-267 (in Russian, not accessible online).

Yin, R., Sun, X., Wang, S., and Wu, B. 2024. Mineral Chemistry of Pyrochlore Supergroup Minerals as Records of Nb Mineralization Processes in NYF-Type Pegmatites: A case Study of the Emeishan Large Igneous Province, SW China. *Minerals*, **14**(1), pp. 13-33. https://doi.org/10.3390/min14010013.

ANNEXES

ANNEX I: ADDITIONAL FT-RAMAN SPECTRA

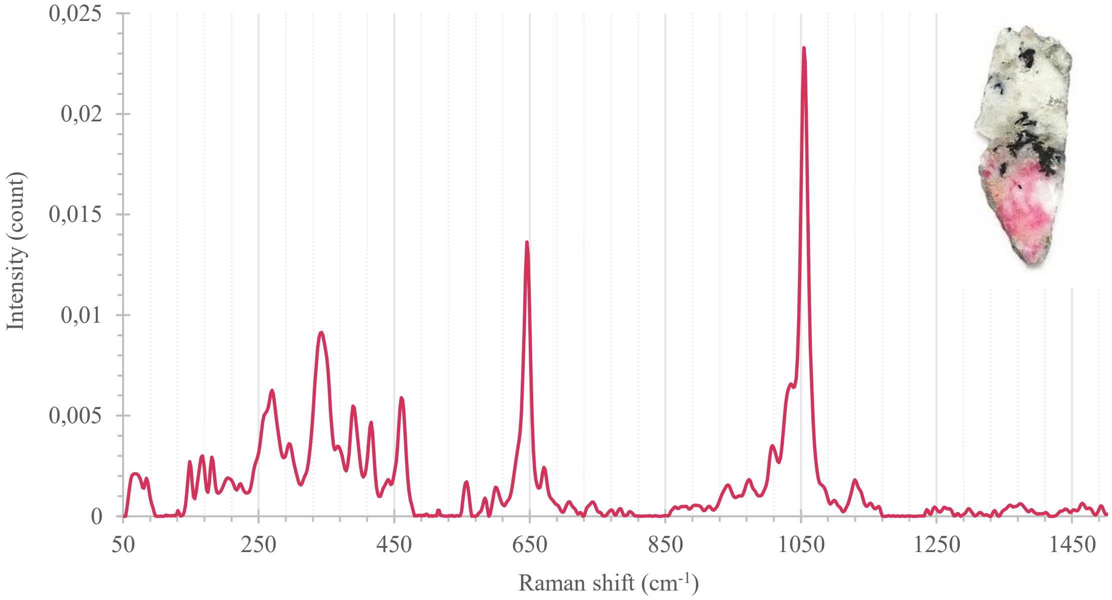

Figure 76: TU01 Fourier-Transform Raman spectrum. Background has been removed for clarity. Photograph of TU01 by Claire Chapuis.

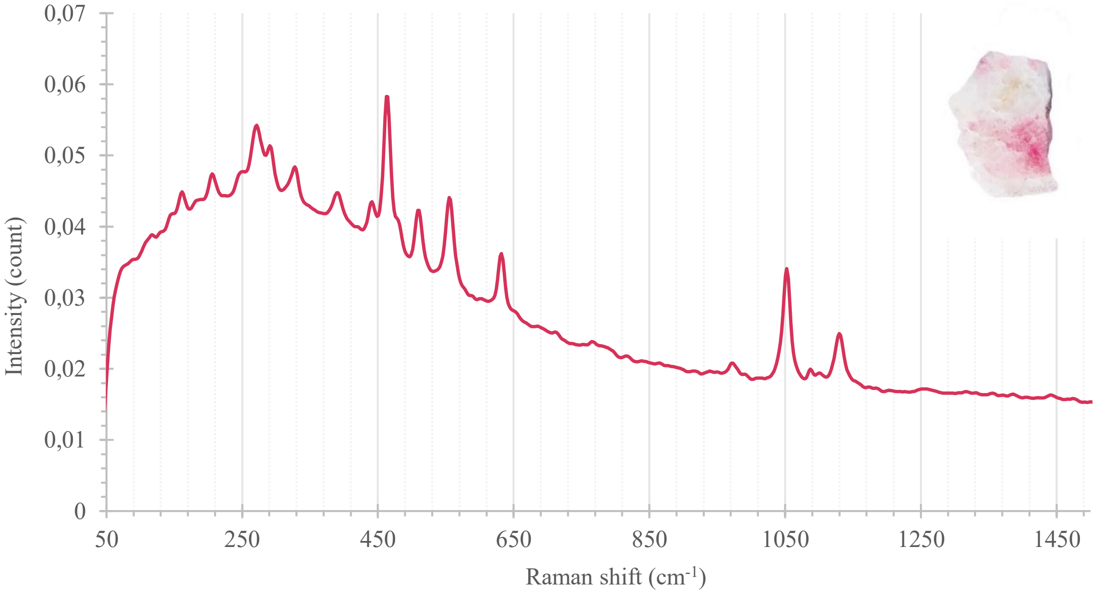

Figure 77: TU04 Fourier-Transform Raman spectrum. Photograph of TU04 by Claire Chapuis.

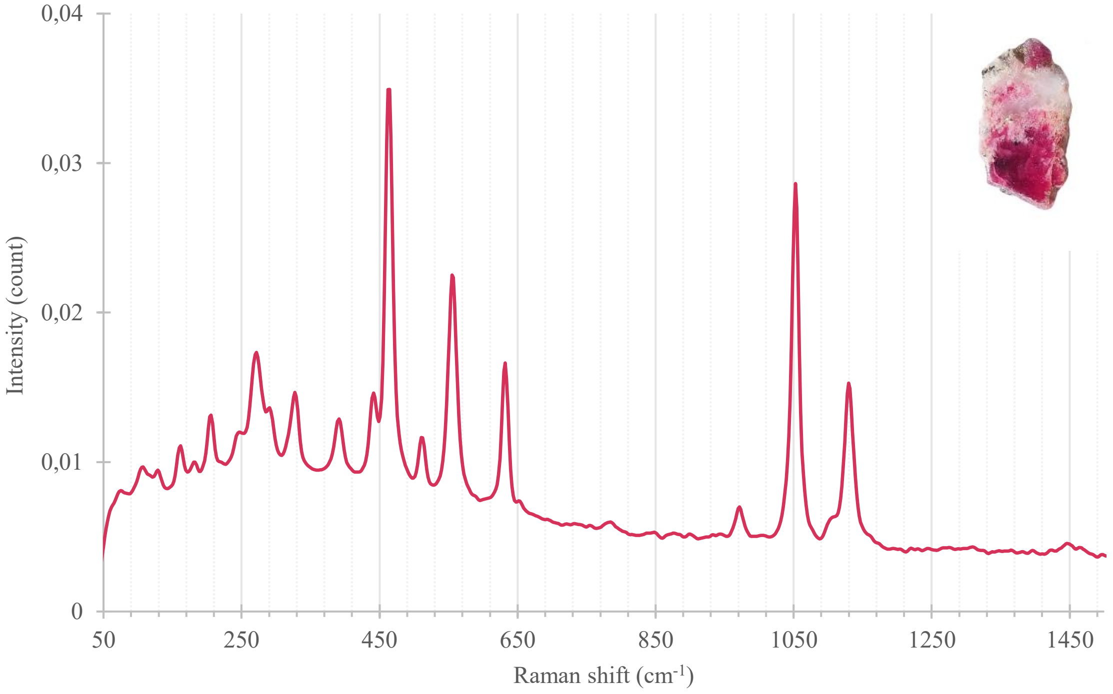

Figure 78: TU05 Fourier-Transform Raman spectrum. Photograph of TU05 by Claire Chapuis.

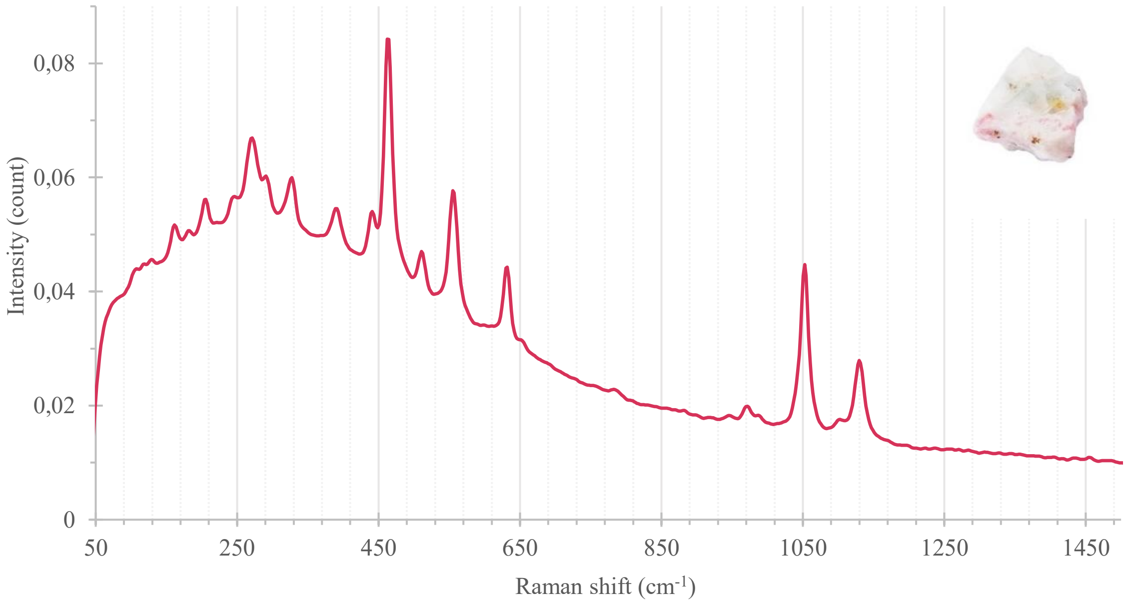

Figure 79: TU06 Fourier-Transform Raman spectrum. Photograph of TU06 by Claire Chapuis.

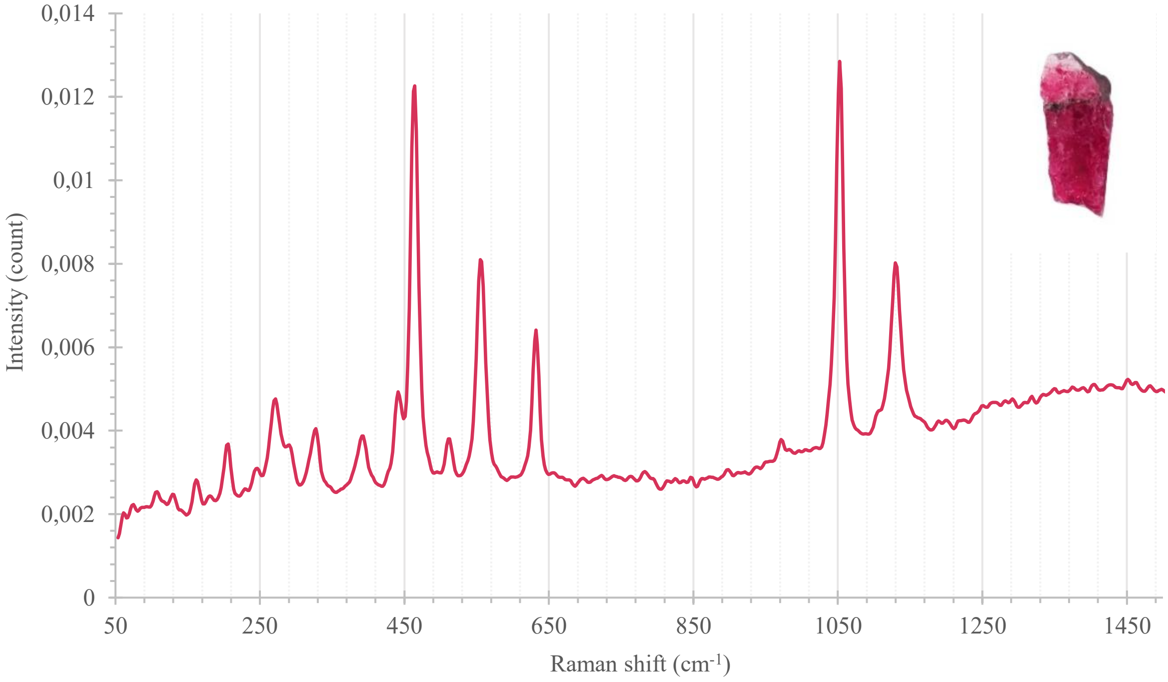

Figure 80: TU08 Fourier-Transform Raman spectrum. Photograph of TU08 by Claire Chapuis.

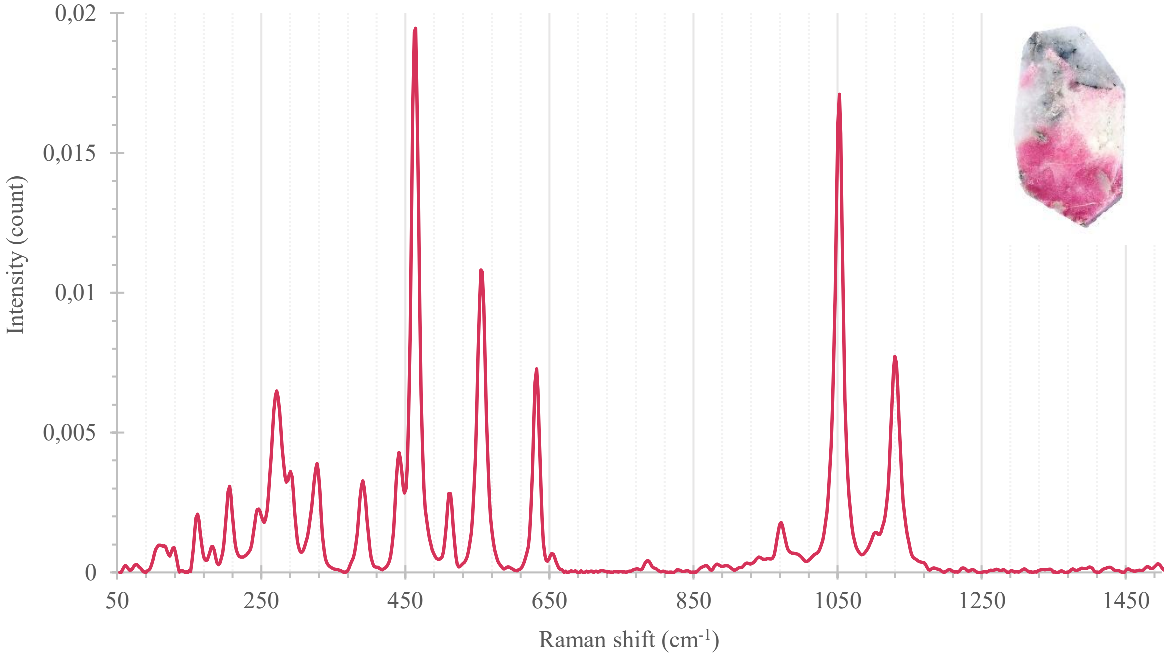

Figure 81: TU09 Fourier-Transform Raman spectrum. Background has been removed for clarity. Photograph of TU09 by Claire Chapuis.

ANNEX II: EDXRF ANALYSES RESULTS

Element	***Normalized concentration (ppm)***															
	TU01 (Narsap Ilua, Kujalleq)**	Uncertainty	**TU02 (Narsap Ilua, Kujalleq)****	Uncertainty	**TU05 (Narsap Ilua, Kujalleq)****	Uncertainty	**TU07 (Greenland)**	Uncertainty	**TU08 (Greenland)**	Uncertainty	**TU08 Rough (Greenland)**	Uncertainty	**TU09 (Greenland)**	Uncertainty	**TU10 (Assigned to Greenland)**	Uncertainty
Na	354300	1400	255500	1600	275100	1600	275500	1600	285700	1600	249100	1500	371600	2000	239000	1500
Al	24900	120	73070	180	71220	190	69040	180	69210	180	68100	160	80030	240	67370	160
Si	459690	200	304860	190	292840	190	302480	190	298600	190	283680	160	287420	230	300930	170
K	1063	18	7512	45	2786	39	626	21	163	19	8673	44	589	21	4593	35
Ca	391.1	7	9802	28	21470	40	195.7	6.4	88.2	6.5	6801	27	749.6	9.3	4752	19
Mn	40.4	2.5	[0.7]*	3	205.3	4.1	51.9	3.2	[5.7]*	3.1	147.7	4	0	0	58.4	3.5
Fe	103	2.2	129.8	2.7	60.5	2.1	112.1	2.5	68.7	2.1	709.3	5.4	137.9	3	1462.4	7.4
Sr	130.2	1.5	14,33	0.61	8.1	1.2	25.2	1.3	8.8	1.1	21.2	1.3	87.8	1.6	79.7	1.6
Ba	1910	110	338	54	[200]*	120	**0**	**0**	[40]*	110	510	130	470	120	530	140
Ga	114	1.8	488.4	3,6	424.5	3.2	509.4	3.6	394.8	3.1	502.1	3.3	313.4	3	497.2	3.2
Mg	6355	97	2361	93	2810	100	2369	99	2870	100	2339	86	2770	120	2467	86
S	9571	45	5282	33	5485	34	5524	33	5806	35	4778	33	0	0	9495	36
Cl	138810	420	339630	700	326830	710	342970	710	336870	720	374080	660	255660	720	368120	670
Br	71.54	0.81	5.44	0.29	172.4	1.4	93.7	1.1	149.9	1.3	215.5	1.5	73.1	1	187.9	1.4
I	[29]*	16	[21.3]*	9.8	**0**	0	123	23	**0**	0	**0**	0	[7]*	20	[39]*	24
Cs	[124]*	30	[23]*	17	**0**	0	**0**	0	**0**	0	**0**	0	**0**	0	[170]*	46
Cr	**0**	0	[5]*	2	**0**	0	12,6	1,9	**0**	0	**0**	0	**0**	0	[9.6]*	2.3
Ni	**0**	0	[2.0]*	1.2	9.7	1.1	[2.75]*	0.92	[2.7]*	1.1	[1.7]*	1.1	**0**	0	7.6	1.2
V	**0**	0	[1.1]*	2.2	0	0	**0**	0	**0**	0	**0**	0	**0**	0	[7.4]*	2.2
Ti	368.2	6.2	91,1	4.2	348.9	6.3	26	2.9	[10.1]*	2.5	260.5	6	49.2	3.6	191.7	4.9
Sc	**0**	0	[2.08]*	0.66	**0**	0	[0.15]*	0.31	3,7	0.54	**0**	0	**0**	0	**0**	0
Rb	10.43	0.68	4,08	0.31	12.16	0.83	5,16	0.73	**0**	0	5.86	0.79	2.27	0.59	11.73	0.83
Cu	11,7	1.2	29,2	1.5	**0**	0	[0.96]*	0.93	**0**	0	4.9	1.1	3.13	0.89	14.8	1.3
Zn	2051.9	5.7	848.4	4.6	20.1	1.1	332.7	3	20.31	0.96	112.3	1.8	5.33	0.76	31.2	1.1

🟦 *Primary constituent* 🟩 *Common impurities listed in the literature* *[ ]* Below detection limit* *** Specific location in Greenland*

ANNEX III: SEM ASSOCIATED MINERALS ANALYSES RESULTS

TU01 Associated Minerals

K-bearing Tugtupite

% element mass	*TU01*
Na_2O	26.67
Uncertainty (+/-)	0.10
Al_2O_3	11.68
Uncertainty (+/-)	0.08
SiO_2	53.47
Uncertainty (+/-)	0.18
Cl	7.99
Uncertainty (+/-)	0.05
K_2O	0.19
Uncertainty (+/-)	0.02
Total	100 (+/-) 0.43

Albite

% element mass	*Reference: Mposkos et al., 2012 (2)*	*TU01*
Na_2O	11.77	12.25
Uncertainty (+/-)		0.06
Difference (%)		*4.07%*
Al_2O3	19.33	19.57
Uncertainty (+/-)		0.09
Difference (%)		*1.24%*
SiO_2	68.65	68.17
Uncertainty (+/-)		0.19
Difference (%)		*0.70%*
Total	99.75	99.99 (+/-) 0.34

Chkalovite

% element mass	*Reference: American Mineralogist Crystal Structure Database record, 2001 - Chkalovite (2)*	*Recalculate without BeO*	*TU01*
SiO_2	58.01	65.99	66.06
Uncertainty (+/-)			0.2
Difference (%)			*0.10%*
Na_2O	29.92	34.01	33.94
Uncertainty (+/-)			0.11
Difference (%)			*0.20%*
BeO	12.07	0	non-detectable
Total	100	100	100

Microcline

% element mass	*Reference: Rosenholtz & Smith, 1942 (without impurities*)*	*Recalculate*	*TU01*
SiO_2	65.1	66.4	64.26
Uncertainty (+/-)			0.18
Difference (%)			*1.29%*
Al_2O_3	18.8	19.18	18.5
Uncertainty (+/-)			0.09
Difference (%)			*1.59%*
K_2O	14.14	14.42	17.23
Uncertainty (+/-)			0,09
Difference (%)			*19.48%*
Total	98.04	100	100 (+/-) 0.36

*Impurities listed: Fe_2O_3, FeO, MgO, CaO, Na_2O, TiO_2, H_2O^+, H_2O^- for a total of 2.33.

Barylite

% element mass	*Reference: Lapache, 1937 - Barylite (3)*	*Recalculate without BeO*	*TU01*
SiO_2	37.14	43.93	44.67
Uncertainty (+/-)			0.17
Difference (%)			*1.68%*
BaO	47.39	56.07	55.33
Uncertainty (+/-)			0.24
Difference (%)			*1.32%*
BeO	15.47	0	non-detectable
Total	100	100	100

Manganoneptunite

% element mass	*Reference: Laird et Albee, 1972 - Neptunite (1)*	*Reference: American Mineralogist Crystal Structure Database record, 2001 – Mangan-neptunite (3)*	*TU01*
SiO_2	53.96	52.98	52.52
Uncertainty (+/-)			0.17
TiO_2	17.74	17.61	16.05
Uncertainty (+/-)			0.12
Al_2O_3	< 0.10	0	0
Fe_2O_3	0	0	15.32
Uncertainty (+/-)			0.15
FeO	11.71	7.92	0
MnO	1.40	7.82	3.36
Uncertainty (+/-)			0.07
MgO	1.73	0	0
BaO	0.25	0	0
Li_2O	bdl	1.65	0
Na_2O	7.38	6.83	7.43
Uncertainty (+/-)			0.06
K_2O	4.84	5.19	5.33
Uncertainty (+/-)			0.05
Total	99.01	100	100.01 (+/-) 0.51

Neptunite without Mn

% element mass	*Reference: Flink et Gust, 1893 - Neptunite (1)*	*TU01*
SiO_2	51.53	54.45
Uncertainty (+/-)		0.17
Difference (%)		*5.66%*
TiO_2	18.13	17.66
Uncertainty (+/-)		0.13
Difference (%)		*2.59%*
Fe_2O_3	0	14.74
Uncertainty (+/-)		0.16
FeO	10.91	0
MnO	4.97	0
MgO	0.49	0.23
Uncertainty (+/-)		0.02
Difference (%)		*53.06%*
Na_2O	9.26	7.42
Uncertainty (+/-)		0.06
Difference (%)		*19.87%*
K_2O	4.88	5.50
Uncertainty (+/-)		0.05
Difference (%)		*12.70%*
Total	100.17	100 (+/-) 0.59

TU01 - (1) is likely a Nb-rich eudialyte, whereas TU01 – (2) is presumed to be a Nb-rich, F- and Ce-bearing species, belonging to either the eudialyte or pyrochlore group.

% element mass	*Reference: Johnsen et Grice, 1999 - Eudialyte (17)*	*Reference: Johnsen et al., 1998 - Kentbrooksite*	*Reference: Grice & Gault, 2006 - Johnsenite-(Ce) (1)*	*Reference: Yin et al., 2024 - Pyrochlore (Pcl-IV) **	***TU01 - (1)***	***TU01 - (2)***
F	0.71	0.88	0	3.51	0	3.45
Uncertainty (+/-)						0.07
Cl	0.88	0.29	0.77	0	0	0
Na_2O	11.69	14.51	10.47	5.90	6.39	4,95
Uncertainty (+/-)					0,06	0.05
K_2O	0.38	0.43	0.25	0	1.09	0.6
Uncertainty (+/-)					0.03	0.03
CaO	5.6	5.62	8.98	15.04	4.28	6.52
Uncertainty (+/-)					0.06	0.07
SrO	1.71	0.49	1.6	0	0	0
MgO	0.06	0.06	0	0	0	0
BaO	0.17	0	0	bdl	0	0
TiO_2	0.83	0.56	0.73	6.51	2.19	2.33
Uncertainty (+/-)					0.06	0.06
FeO	3.18	1.58	1.61	0.19	0	0
Fe_2O_3	0	0	0	0	1.53	0
Uncertainty (+/-)					0.06	
MnO	4.52	8.01	5.43	0.09	0	0
ZnO	0	0	0	0	1.67	0

Uncertainty (+/-)					0.12	
Nb_2O_5	1.78	2.26	0.82	58.11	55.59	66.22
Uncertainty (+/-)					0.21	0.22
ZrO_2	11.22	11.08	9.6	bdl	0	0
HfO_2	0.18	0.36	0.04	0	0	0
WO_3	0	0	5.23	0	0	0
Al_2O_3	1.22	0.21	0	0	0	0
SiO_2	43.9	45.34	43.16	0	27.26	1.,45
Uncertainty (+/-)					0.13	0.08
CeO_2	0	0	0	0	0	5.48
Uncertainty (+/-)						0.11
Ce_2O_3	2.73	2.44	3.01	3.20	0	0
La_2O_3	1.75	2.23	1.56	0.71	0	0
Nd_2O_3	0.69	0.69	0.89	0.56	0	0
Yb_2O_3	0.32	0	0	0	0	0
Y_2O_3	1.66	1.46	0.7	0.22	0	0
Pr_2O_3	0	0	1.14	0.39	0	0
Sm_2O_3	0	0	0,12	bdl	0	0
Gd_2O_3	0.11	0	0.33	0	0	0
Dy_2O_3	0	0	0.14	0	0	0
O=Cl	-0.2	-0.07	-0.17	0	0	0
O=F	-0.3	-0.37	0	0	0	0
CO_2	0	0	1.27	0	0	0
H_2O	0	1.28	0.32	0	0	0
Total	94.79	99.34	98	94.43	100 (+/-) 0.73	100 (+/-) 0.69

bdl = below detection limit.

*Without PbO, UO_2, ThO_2, and Ta_2O_5 for a total of 6.62.

▨ : Rare Earth Elements (REE)

TU02 Associated Minerals

Albite

% element mass	*Reference: Mposkos et al., 2012 (2)*	*TU02*
Na_2O	11.77	12.19
Uncertainty (+/-)		0.66
Difference (%)		*3.56%*
Al_2O_3	19.33	19.65
Uncertainty (+/-)		0.09
Difference (%)		*1.65%*
SiO_2	68.65	68.14
Uncertainty (+/-)		0.19
Difference (%)		*0.74%*
Total	99.75	99.98 (+/-) 0.94

Microcline

% element mass	*Reference: Rosenholtz & Smith, 1942 (without impurities*)*	*TU02*
SiO_2	65.1	63.95
Uncertainty (+/-)		0.18
Difference (%)		*1.76%*
Al_2O_3	18.8	18.56
Uncertainty (+/-)		0.09
Difference (%)		*1.27%*
K_2O	14.14	17.23
Uncertainty (+/-)		0.09
Difference (%)		*21.85%*
Na_2O	1.99	0.26
Uncertainty (+/-)		0.01
Difference (%)		*86.93%*
Total	100.03	100 (+/-) 0.37

*Impurities listed: Fe_2O_3, FeO, MgO, CaO, TiO_2, H_2O^+, H_2O^- for a total of 0.34.

TU03 Associated Minerals

K-bearing Tugtupite

% element mass	*TU03*
Na_2O	28.62
Uncertainty (+/-)	0.10
Al_2O_3	11.30
Uncertainty (+/-)	0.08
SiO_2	52.58
Uncertainty (+/-)	0.18
Cl	7.23
Uncertainty (+/-)	0.05
K_2O	0.28
Uncertainty (+/-)	0.02
Total	100 (+/-) 0.43

**
32.55% of the orthoclase pole
25.58% of the albite pole
41.86% of the anorthite pole

***
31.78% of the orthoclase pole
35.32% of the albite pole
32.89% of the anorthite pole

~42% Anorthite** and ~35% Albite***

% element mass	*Reference: Smith et Ribbe, 1966 - Orthoclase 90,1 wt.% (Spencer C) without impurities**	*Reference: Janák et al., 2011 - Albite (OBI3a)*	*Reference: Janák et al., 2011 - Anorthite (OBI3d)*	*TU03***	*TU03****
Na_2O	0.9	8.66	0.25	2.54	3.68
Uncertainty (+/-)				0.04	0.04
SiO_2	64.2	62.69	43.83	62.9	63.75
Uncertainty (+/-)				0.22	0.21
Al_2O_3	18.3	23.8	35.64	22.09	21.31
Uncertainty (+/-)				0.11	0.11
CaO	0.1	5.03	19.81	7.59	6.22
Uncertainty (+/-)				0.08	0.07
K_2O	15.3	0.15	0.01	4.88	5.04
Uncertainty (+/-)				0.06	0.06
Total	98.8*	100.33	99.54	100 (+/-) 0.51	100 (+/-) 0.49

*Impurities listed: SrO and BaO for a total of 0.2.

Albite

% element mass	*Reference: Mposkos et al., 2012 (2)*	*TU03*
Na_2O	11.77	12.12
Uncertainty (+/-)		0.07
Difference (%)		*2.97%*
Al_2O_3	19.33	19.65
Uncertainty (+/-)		0.09
Difference (%)		*1.65%*
SiO_2	68.65	68.23
Uncertainty (+/-)		0.19
Difference (%)		*0.61%*
Total	99.75	100 (+/-) 0.35

Unidentified Ba-bearing species

% element mass	*TU03*
Na_2O	1.51
Uncertainty (+/-)	0.02
Al_2O_3	22.05
Uncertainty (+/-)	0.06
SiO_2	63.84
Uncertainty (+/-)	0.12
K_2O	4.67
Uncertainty (+/-)	0.03
CaO	5.54
Uncertainty (+/-)	0.04
BaO	2.31
Uncertainty (+/-)	0.04
Total	99.92 (+/-) 0.31

TU04 Associated Minerals

Albite

% element mass	*Reference: Mposkos et al., 2012 (2)*	*TU04*
Na_2O	11.77	11.64
Uncertainty (+/-)		0.06
Difference (%)		*1.10%*
Al_2O_3	19.33	19.65
Uncertainty (+/-)		0.09
Difference (%)		*1.65%*
SiO_2	68.65	68.71
Uncertainty (+/-)		0.19
Difference (%)		*0.08%*
Total	99.75	100(+/-) 0.34

Likely a Nb-rich, Ce- and U-bearing member of the eudialyte or pyrochlore group

% element mass	*Reference: Johnsen et Grice, 1999 - Eudialyte (17)*	*Reference: Johnsen et al., 1998 - Kentbrooksite*	*Reference: Yin et al., 2024 - Pyrochlore (Pcl-I)**	*TU04*
F	0.71	0.88	1.60	0
Cl	0.88	0.29	0	0.55
Uncertainty (+/-)				0.01
Na_2O	11.69	14.51	3.56	3.05
Uncertainty (+/-)				0.05
K_2O	0.38	0.43	0	0.88
Uncertainty (+/-)				0.02
CaO	5.6	5.62	14.74	5.96
Uncertainty (+/-)				0.05
SrO	1.71	0.49	0	0
MgO	0.06	0.06	0	0
BaO	0.17	0	bdl	0
TiO_2	0.83	0.56	12.82	0
FeO	3.18	1.58	0.34	0
Fe_2O_3	0	0	0	1.18
Uncertainty (+/-)				0.05
MnO	4.52	8.01	0.06	0
ZnO	0	0	0	3.79
Uncertainty (+/-)				0.13
Nb_2O_5	1.78	2.26	41.54	30.39
Uncertainty (+/-)				0.14
ZrO_2	11.22	11.08	bdl	0
HfO_2	0.18	0.36	0	0
Al_2O_3	1.22	0.21	0	1.89
Uncertainty (+/-)				0.03
SiO_2	43.9	45.34	0	40.17
Uncertainty (+/-)				0.12
P_2O_5	0	0	0	0
U_3O_8	0	0	0	9.19
Uncertainty (+/-)				0.2

UO_2	0	0	15.12	0
CeO_2	0	0	0	2.95
Uncertainty (+/-)				0.08
Ce_2O_3	2.73	2.44	2.95	0
La_2O_3	1.75	2.23	0.36	0
Nd_2O_3	0.69	0.69	0.85	0
Yb_2O_3	0.32	0	0	0
Y_2O_3	1.66	1.46	0.19	0
Pr_2O_3	0	0	0.27	0
Sm_2O_3	0	0	0.21	0
Gd_2O_3	0.11	0	0	0
Dy_2O_3	0	0	0	0
O=Cl	-0.2	-0.07	0	0
O=F	-0.3	-0.37	0	0
H_2O	0	1.28	0	0
Total	94.79	99.34	94.61*	100 (+/-) 0.88

bdl = below detection limit.

*Without PbO, ThO_2, and Ta_2O_5 for a total of 5.47.

▨ : Rare Earth Elements (REE)

TU05 Associated Minerals

Aegirine

% element mass	*Reference: Piilonen et Mcdonald, 1998 - Aegirine (SX934) without impurities**	*Reference: Gwozdz et al., 2001 - Aegirine lujavrite (6) without impurities***	*TU05*
Na_2O	12.15	10.72	6.56
Uncertainty (+/-)			0.04
Al_2O_3	1.17	13.2	0.43
Uncertainty (+/-)			0.02
SiO_2	51.54	52.38	48.81
Uncertainty (+/-)			0.13
K_2O	0	2.82	4.1
Uncertainty (+/-)			0.03
TiO_2	0.53	0.22	0.51
Uncertainty (+/-)			0.02
MgO	0.29	0.1	0.29
Uncertainty (+/-)			0.02
Fe_2O_3	31.08	10.9	37.66
Uncertainty (+/-)			0.19
FeO	0	1.96	0
Total	96.76*	92.3**	98.36 (+/-) 0.45

*Impurities listed: ZrO_2, MnO, CaO for a total of 3.07.
**Impurities listed: ZrO_2, MnO, MgO, CaO, P_2O_5, H_2O^+, H_2O^-, CO_2, S, Cl, F, “others”.

Albite

% element mass	*Reference: Mposkos et al., 2012 (3)*	*Reference: Mposkos et al., 2012 (3) recalculate without CaO*	*TU05*
Na_2O	10.2	10.48	10.7
Uncertainty (+/-)			0.05
Difference (%)			*2.10%*
Al_2O_3	20.85	21.43	21.43
Uncertainty (+/-)			0.08
Difference (%)			*0.00%*
SiO_2	66.16	68.09	67.87
Uncertainty (+/-)			0.15
Difference (%)			*0.32%*
CaO	2.66	0	0
Total	99.87	100	100 (+/-) 0.28

TU06 Associated Minerals

Analcime

% element mass	*Reference: American Mineralogist Crystal Structure Database record, 2001 - Analcime (3)*	*Recalculate without H_2O*	*TU06*
Na_2O	14.08	15.32	14.69
Uncertainty (+/-)			0.07
Difference (%)			*4.11%*
Al_2O_3	23.16	25.24	25.54
Uncertainty (+/-)			0.1
Difference (%)			*1.18%*
SiO_2	54.58	59.33	59.77
Uncertainty (+/-)			0.17
Difference (%)			*0.74%*
H_2O	8.18	0	bdl
Total	100	99.89	100 (+/-) 0.34

Sodalite

% element mass	*Reference: Antao et Hassan, 2002 - Sodalite without impurities**	*TU06*
Na_2O	25.3	26.46
Uncertainty (+/-)		0.08
Difference (%)		*4.58%*
Al_2O_3	31.78	30.85
Uncertainty (+/-)		0.1
Difference (%)		*2.92%*
SiO_2	36.55	35.74
Uncertainty (+/-)		0.12
Difference (%)		*2.21%*
Cl	7.17	7.01
Uncertainty (+/-)		0.04
Difference (%)		*2.23%*
Total	100.8*	100 (+/-) 0.34

*Impurities listed: CaO, K_2O, Fe_2O_3, MnO, MgO, S, and O=Cl, S.

Aegirine/Arfvedsonite

% element mass	*Reference: Piilonen et Mcdonald, 1998 - Aegirine (SX934) without impurities**	*Reference: Gwozdz et al., 2001 - Aegirine lujavrite without impurities***	*Reference: Gwozdz et al., 2001 - Arfvedsonite lujavrite without impurities***	*TU06*
Na_2O	12.15	10.72	9.25	7.35
Uncertainty (+/-)				0.05
Al_2O_3	1.17	13.2	12.23	0.75
Uncertainty (+/-)				0.02
SiO_2	51.54	52.38	52.25	51.74
Uncertainty (+/-)				0.15
K_2O	0	2.82	3.23	4.71
Uncertainty (+/-)				0.04
TiO_2	0.53	0.22	0.23	0.54
Uncertainty (+/-)				0.03
Fe_2O_3	31.08	10.9	6.06	34.97
Uncertainty (+/-)				0.49
FeO	0	1.96	8.72	0
Total	96.47*	92.2**	91.97**	100.06 (+/-) 0.78

*Impurities listed: ZrO_2, MnO, MgO, CaO for a total of 3.36.

**Impurities listed: ZrO_2, MnO, MgO, CaO, P_2O_5, H_2O^+, H_2O^-, CO_2, S, Cl, F, “others”.

ANNEX IV: SUPPLEMENTARY SEM PHOTOMICROGRAPHS

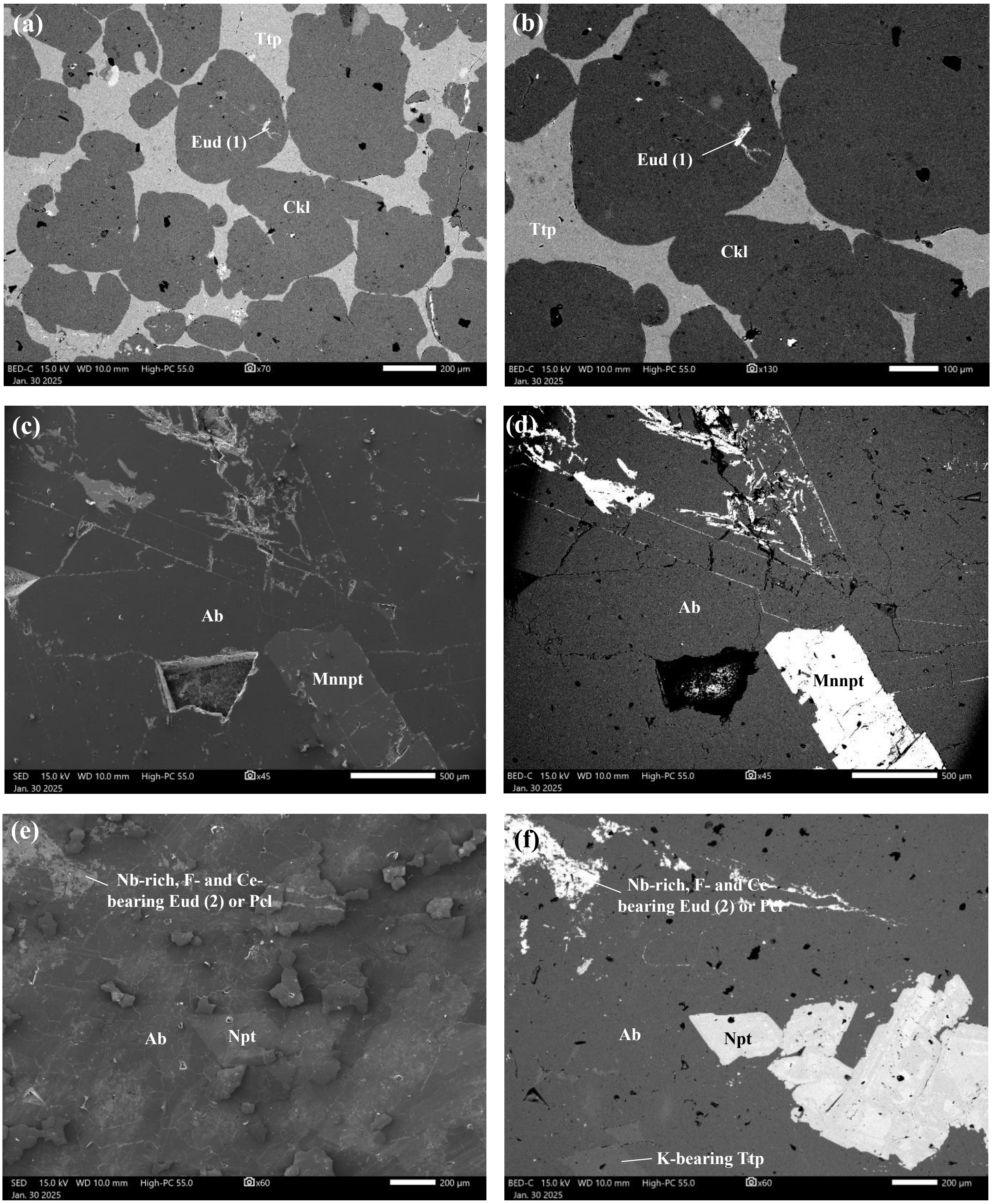

Figure 82: TU01 thick section. (a) Backscattered electron (BSE) image showing minerals associated with TU01. (b) Close-up of (a), highlighting a suggested Nb-rich eudialyte inclusion surrounded by chkalovite and tugtupite. (c) Secondary electron (SED) image of albite and manganoneptunite associated minerals. (d) Same region as (c), imaged using backscattered electron (BSE). (e) Secondary electron (SED) image of a suggested Nb-rich, F- and Ce-bearing species, belonging to either the eudialyte or pyrochlore group, with albite and neptunite. (f) Same region as (e), shown in backscattered electron (BSE) imaging.

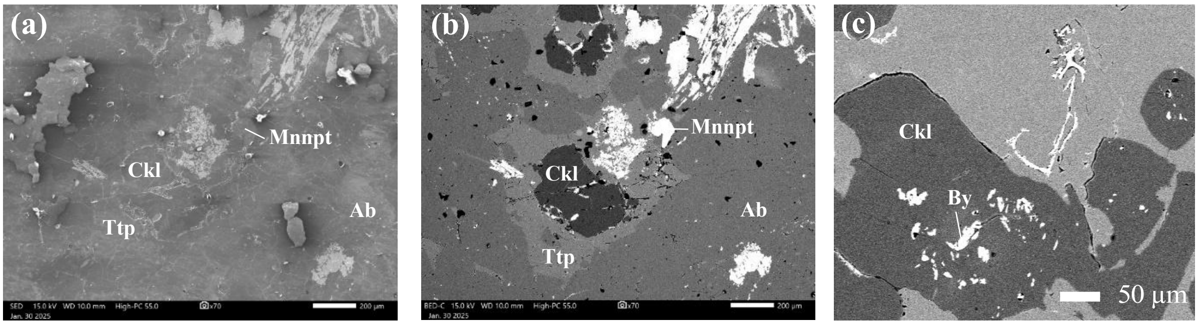

Figure 83: TU01 thick section. (a) Secondary electron (SED) image showing minerals associated with TU01. (b) Same area as (a), using backscattered electron (BSE). (c) Close-up view of barylite surrounded by chkalovite in TU01.

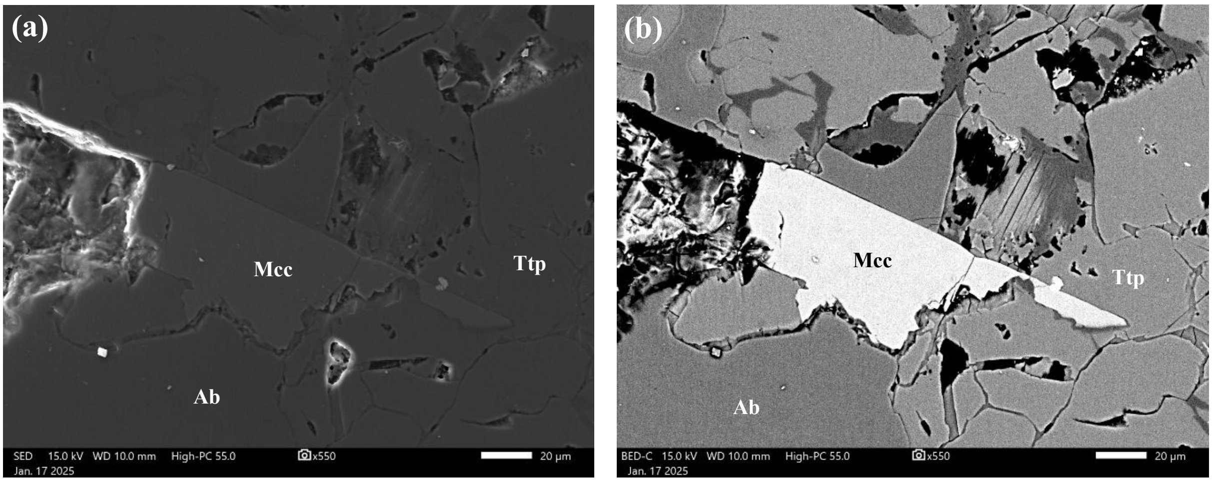

Figure 84: TU02 thick section. (a) Secondary electron (SED) image showing albite and microcline associated with tugtupite. (b) Same region as (a), in backscattered electron (BSE) imaging.

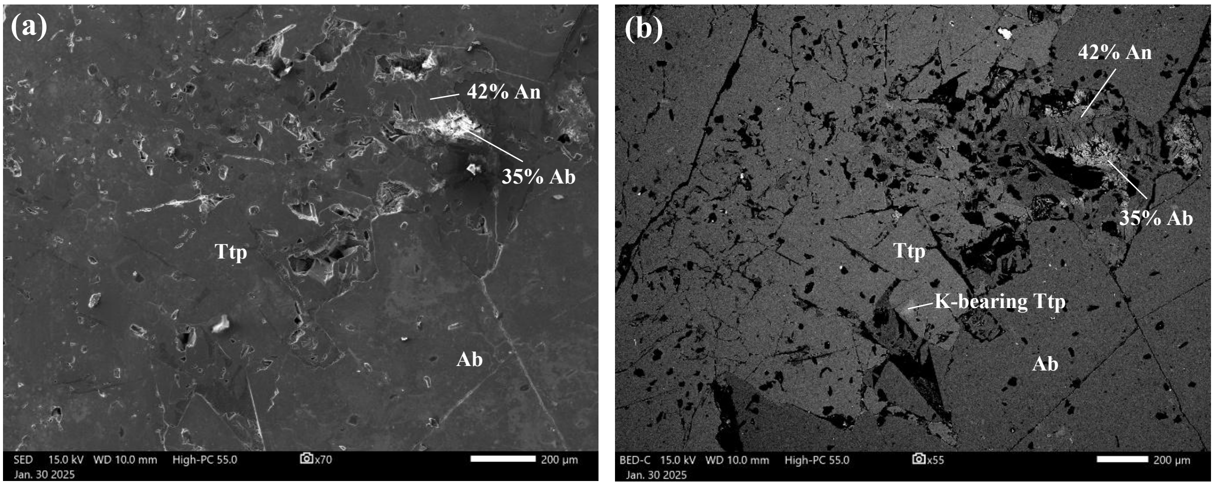

Figure 85: TU03 thick section. (a) Secondary electron (SED) image showing albite and anorthite associated with tugtupite. (b) Same region as (a), imaged using backscattered electron (BSE).

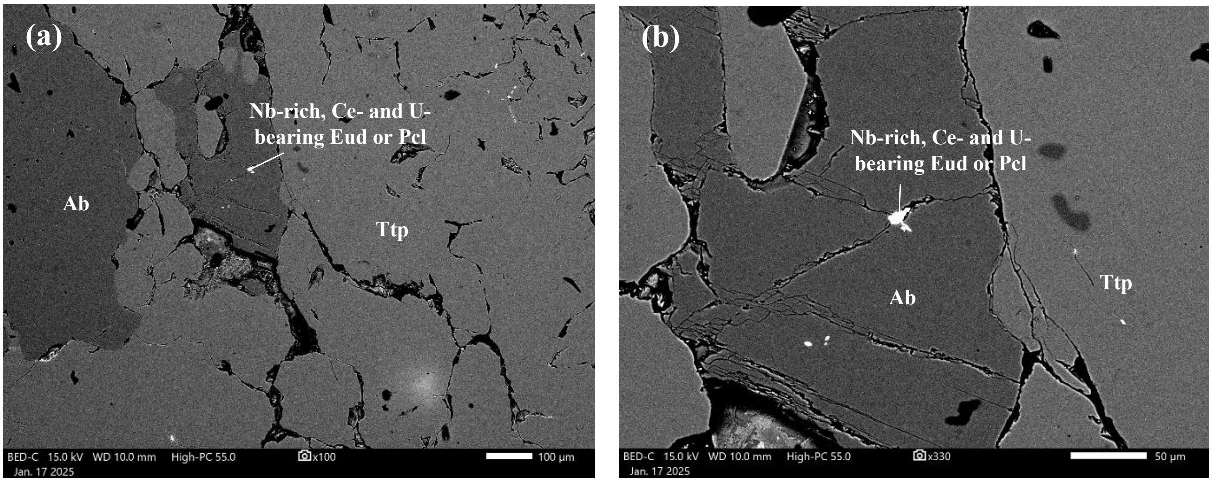

Figure 86: TU04 thick section. (a) Backscattered electron (BSE) image showing minerals associated with TU04. (b) Close-up of (a), highlighting a Nb-rich, Ce- and U- bearing species suggests to be a member of the pyrochlore or eudialyte group, surrounded by albite and tugtupite.

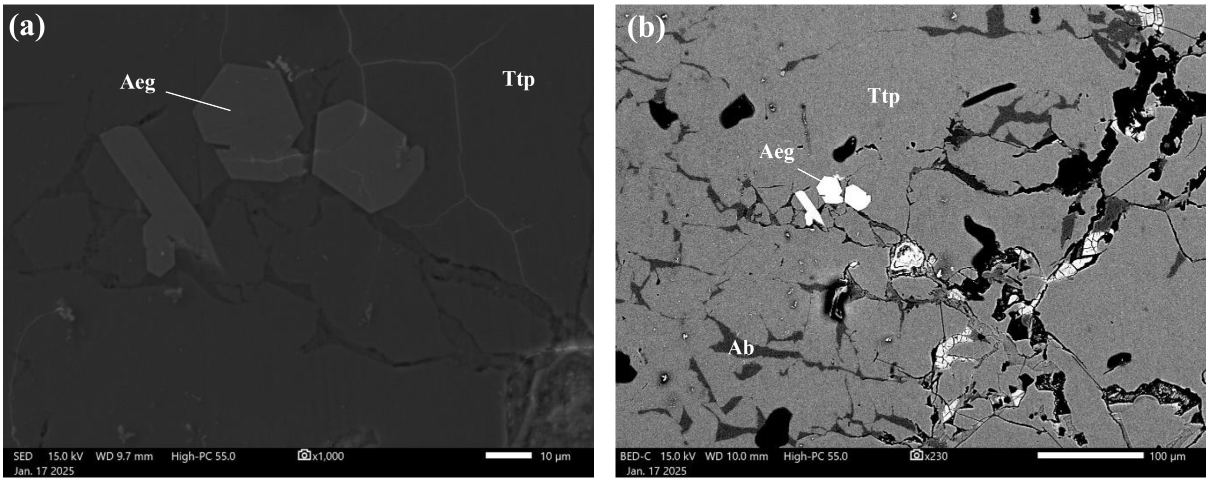

Figure 87: TU05 thick section. (a) Secondary electron (SED) close-up image showing aegirine or/and arfvedsonite associated with tugtupite. (b) Backscattered electron (BSE) image of TU01 associated minerals.